UNIVERSITY OF CALIFORNIA,
IRVINE

Mitigating Electrode Deactivation Through Microstructural Design

DISSERTATION

submitted in partial satisfaction of the requirements
for the degree of

DOCTOR OF PHILOSOPHY

in Materials Science and Engineering

by

Kyle McAnulty McDevitt

Dissertation Committee
Associate Professor Ali Mohraz, Chair
Associate Professor Daniel R. Mumm
Associate Professor Shane Ardo

2019

COPYRIGHT

Sections of this dissertation have been previously published and are re-used here with appropriate permissions:

TABLE OF CONTENTS

Page

LIST OF SYMBOLS

2D – Two-Dimensional

3D – Three-Dimensional

A – Surface area

APTES – 3-Aminopropyltriethyloxysilane

Bijel – Bicontinuous Interfacially Jammed Emulsion Gel

CLSM – Confocal Scanning Laser Microscopy

CV – Cyclic Voltammetry

D_a – Intrinsic Diffusivity

D_e – Effective Diffusivity

DOD – Depth of Discharge

E – Potential

e – Edges (in a 3D computer mesh)

EDL - Electrochemical Double Layer

EtOH – Ethanol alcohol

EV – Electric Vehicle

ϵ – Porosity

F – Formation Factor

f – Faces (in a 3D computer mesh)

FAST – Field Assisted Sintering Technique

FEA – Finite Element Analysis

FEG – Field Emission Gun

G – Genus

G_s – Scaled Genus

h – Hour(s)

HER – Hydrogen Evolution Reaction

HF – Hydrofluoric Acid

HVAC – Heating, Ventilation, and Air Conditioning

I – Current

IPA – Isopropanol alcohol

j – Current Density

k_1, k_2 – Principal Curvatures ($k_2 \leq k_1$)

L – Length / Distance (Euclidean)

L_e – Length / Distance (Tortuous pathways)

LCST - Lower Critical Solution Temperature

M_n – Molecular weight

m – Minute(s)

m_A – Archie's law exponent

n – Vertices (in a 3D computer mesh)

OER – Oxygen Evolution Reaction

PEGDA - polyethylene glycol diacrylate

QRE – Quasi Reference Electrode

RBITC – Rhodamine B Isothiocyanate

S_v^{-1} – Volume per surface area

SE – Secondary Electron

SEM – Scanning Electron Microscop(e/y)

s – Second(s)

t – Time

τ – Tortuosity

$\bar{\tau}$ – Representative Tortuosity

$\bar{\tau}_{0.5}$ – Scaled τ at $\epsilon = 0.5$

TEOS – Tetraethylorthosilicate

μCT – X-ray Micro Computed Tomography

UV – Ultraviolet

V_x - Volume fraction of phase *x*

x_x – Mole fraction of phase *x*

χ – Euler-Poincare Characteristic

XRD – X-ray Diffraction

LIST OF TABLES

LIST OF FIGURES

ACKNOWLEDGMENTS

This work was created with financial support from the National Science Foundation (CMMI 1301489) and the National Aeronautics and Space Administration (NNX13AQ69G & 80NSSC18K1554). All other support (emotional, administrative, scientific, and otherwise) was provided through a robust network of family, friends, and coworkers who deserve more thanks than can be expressed here.

First, my family, who has given me space to work when I need it. I've missed almost all the holidays, vacations, and celebrations over the last four years, but I'll spend the rest of my life making it up to all of you.

Next, my friends, who are always ready to help however they can and have given me much-needed encouragement along the way.

Also, my coworkers, who teach me what I need to learn the proverbial 'easy way'.

Finally, to Professors Ali Mohraz and Dan Mumm, who have taught me the rest. Through high standards, you've helped me bring this work to something I can be proud of. Your influence will go beyond what is contained in these pages.

CURRICULUM VITAE

Kyle McAnulty McDevitt

2013 B.S. in Ceramics Engineering, Alfred University, Alfred, NY

2015 M.S. in Ceramics Engineering, Alfred University, Alfred, NY

2020 Ph.D. in Materials Science and Engineering, University of California, Irvine

FIELD OF STUDY PUBLICATIONS AND PRESENTATIONS

McDevitt, K. M.; Gross, S.J; Mumm, D. R.; Mohraz, A. Mitigating the Bubble Effect Through Spinodally-Derived Pore Networks. *In preparation*.

McDevitt, K. M.; Mumm, D. R.; Mohraz, A. Improving Cyclability of ZnO Electrodes through Microstructural Design. ACS Appl. Energy Mater. 2019, 2 (11), 8107–8117. https://doi.org/10.1021/acsaem.9b01584.

Garcia, A. E.; Wang, C. S.; Sanderson, R. N.; **McDevitt, K. M.**; Zhang, Y.; Valdevit, L.; Mumm, D. R.; Mohraz, A.; Ragan, R. Scalable Synthesis of Gyroid-Inspired Freestanding Three-Dimensional Graphene Architectures. Nanoscale Adv. 2019, 1 (10), 3870–3882. https://doi.org/10.1039/C9NA00358D.

McDevitt, K. M.; Mumm, D. R.; Mohraz, A. Improving Cyclability of ZnO Electrodes Through Microstructural Design. ACS Colloids 2019. Atlanta, GA

McDevitt, K. M.; Thorson, T. J.; Botvinick, E. L.; Mumm, D. R.; Mohraz, A. Microstructural Characteristics of Bijel-Templated Porous Materials. Materialia 2019, 7, 100393. https://doi.org/10.1016/j.mtla.2019.100393.

Misture, S. T.; **McDevitt, K. M.**; Glass, K. C.; Edwards, D. D.; Howe, J. Y.; Rector, K. D.; He, H.; Vogel, S. C. Sulfur-Resistant and Regenerable Ni/Co Spinel-Based Catalysts for Methane Dry Reforming. Catal. Sci. Technol. 2015, 5 (9), 4565–4574. https://doi.org/10.1039/C5CY00800J.

ABSTRACT OF THE DISSERTATION

Mitigating Electrode Deactivation Through Microstructural Design

by

Kyle McAnulty McDevitt

Doctor of Philosophy in Materials Science and Engineering

University of California, Irvine, 2019

Associate Professor Ali Mohraz, Chair

Increasing demands for energy storage and conversion has fueled research and development of next-generation electrochemical devices, including batteries, supercapacitors, and catalysts. Viability of technology beyond the proof-of-concept is dependent on the morphology and topology of the electrode, which should be carefully designed to maximize material utilization during operation. Despite the close relationship between microstructure and operational efficiency, there does not currently exist a single configuration that can be broadly applied across electrochemically active materials. The ideal microstructure is expected to have co-continuous and interpenetrating domains that have high interfacial area and present minimal resistance to ionic and electronic transport.

In the following dissertation, I present a technique to create such a structure through bicontinuous interfacially jammed emulsion gels (bijels), which are generated *via* spinodal decomposition and therefore confer characteristic microstructural qualities to derivative materials. Domain size distribution, interfacial curvature, tortuosity, and self-similarity are discussed in detail and compared quantitatively to alternative microstructures that have been

proposed for electrochemical devices. These qualities are shown to influence material utilization in two specific applications, energy storage in zinc electrodes, and electrocatalytic water splitting for hydrogen generation.

Maintaining electronic conductivity in electrodes has been shown previously to delay capacity loss during repeated charge-discharge cycling. In the case of zinc anodes, converting the metallic material to the semiconducting zinc oxide creates heterogeneities in current distribution that inspire material reconfiguration and premature cell failure. Spinodal-like electrodes mitigate these effects by improving electronic accessibility of the active material and maintaining conduction pathways to a high degree of discharge compared to electrodes built with randomly sized features.

Homogeneous activity and co-continuity in an electrode are also advantageous in the electrocatalytic separation of water into constituent hydrogen and oxygen gases. Product desorption from the electrode is necessary to continue the reaction, but microstructural impediments to efficient removal result in the underutilization of active surfaces. Bijel templated electrodes improve gas transport through the same microstructural qualities discussed above and are shown to reduce energy losses associated with this inefficiency.

1. Introduction

1.1. Motivation

Recent concerns over the environmental and economic impact of the energy economy have motivated research into the responsible generation, conversion, storage, and use of this important resource. Next-generation technologies aim to be cheaper, more efficient, or have a smaller environmental impact over device lifetime. Many so-called “green technologies” have been proposed and extensively developed (wind and solar, for example) however, deployment on the grid scale necessitates enormous capacity for energy storage due to their intermittent availability.[1]

Li-ion batteries dominate the market for energy storage in personal electronics and electric vehicles (EV’s), due to the high reversibility and tolerance for variable charge cycling.[2] The reactivity [3,4] and availability of required materials[5,6] present challenges to responsible processing and use. In addition to this, improvement to electrochemical metrics have nearly reached the theoretical limit associated with the materials. To overcome these limitations, new technologies must be adopted.

A Ragone plot is illustrated in Figure 1-1 and compares the normalized energy and power of selected energy storage devices. In general, there is a trade-off between these two metrics, either of which may be preferred depending on application. For example, mobile phones prioritize battery lifetime over processing capabilities, while battery powered tools are designed to deliver energy quickly. Modern vehicles that are fully electric have cells and cooling systems designed to meet these power demands simultaneously.

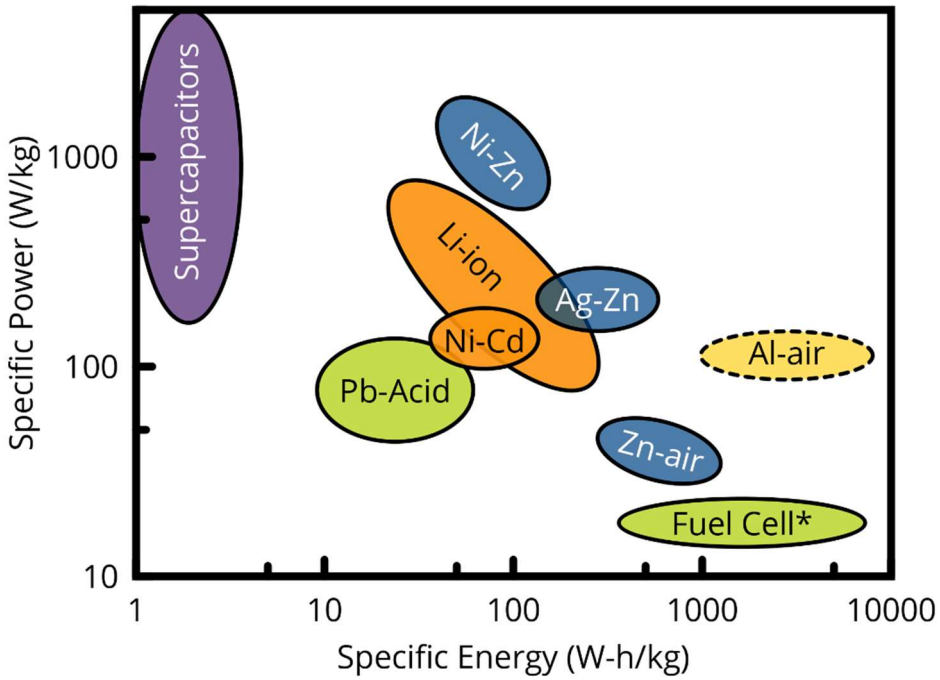

*Figure 1-1: Ragone plot comparting specific power and specific energy of selected electrochemical storage devices. The upper-right portion of the plot is targeted for next-generation secondary cells. *Energy in a fuel cell is dependent on the size of the fuel container. Nota Bene, Al-air cells are non-rechargeable.*

Devices that can simultaneously deliver high energy density and high power density are targeted for the next-generation of electrochemical storage. Strategies toward these goals include hybridizing existing technologies, developing new electrochemically active materials,[7–9] and improvements to established technologies[10–13]. As part of these improvements, the microstructure of active material has recently come under investigation.[10,14–16]

Electrochemical processes involve simultaneous transport and reaction kinetics that are inextricably influenced by electrode microstructure:

a) Transport pathways for reactants

b) Transport pathways for charge

c) Efficient electron transfer between charge collector and reactants.

Generally, (a) takes place in an electrically conducting phase, (b) takes place in an insulating electrolyte phase, and (c) takes place at the interface between the two. To maintain conditions favorable for these three processes, the ideal electrode is expected to comprise interpenetrating phases with high interfacial area. Proposed microstructures satisfying these requirements include those templated from colloidal crystals,[15,17,18] foams,[19,20] and fibers,[7,21,22], among others. The architecture in these electrodes have been carefully engineered to efficiently utilize active material and improve the energy and power densities simultaneously.

Conversely, microstructures with random architecture do not benefit from these design considerations and are prone to deactivation by preventing the processes described above. Interruption of reactant transport or electron transfer compromises material utilization, resulting ultimately in lower power and energy densities or reduced cyclability in the case of rechargeable cells. In this dissertation, porous electrodes deliberately designed to mitigate inefficiencies are compared against stochastically generated analogs. The engineered electrodes are derived from bijels, a relatively new class of soft material with unique microstructural characteristics that prevent material deactivation by maintaining robust transport pathways for reactants. In addition, bijels are attractive templates for electrochemical devices due to their synthesis via self assembly and tunable length scale, which allows deliberate design of power and energy density for a given device.[23]

1.2. Experimental Techniques

Characterization tools used for experiments in this dissertation are illustrated schematically below, with details specific to each project discussed in the respective chapters.

1.2.1. Confocal Microscopy

The first confocal scanning microscope was created in 1955 and patented in 1957 by Mavin Minsky to prevent out of focus planes from contributing signal to the collected data and therefore improve contrast during traditional fluorescent microscopy.[24] In 1969 this concept was further developed into the scanning confocal laser scanning microscope (CLSM), which is even more selective in its imaging plane. The basic concept of confocal microscopy is illustrated in Figure 1-2.

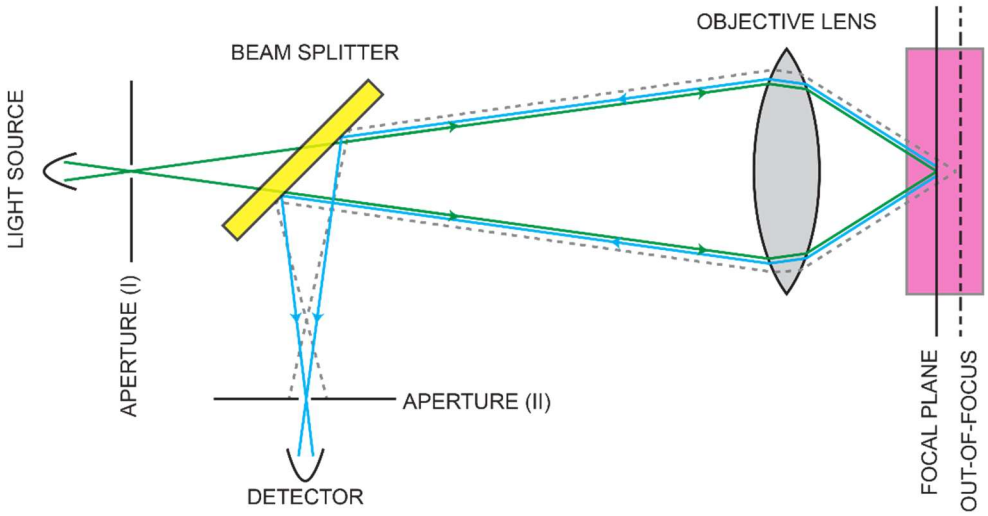

Figure 1-2: Schematic illustration of confocal microscopy

Incident illumination passes through a beam splitter before being focused on the sample with an objective lens. Fluorescent molecules in the sample are excited by this incident radiation. The fluorescent signal traveling backwards along the same optical path is reflected by the beam

splitter toward a detector. Signal from out-of-focus planes has a different path length to convergence and is ultimately rejected by the final aperture before the detector.

Images from CLSM used throughout this dissertation were collected with a monochromatic laser source (Calypso, Cobolt AB, $\lambda = 491$ nm) and confocal scanner (VT-eye, Visitech International, UK) coupled with an inverted microscope (Axio Observer A1, Zeiss). Rhodamine B dye, either in a fluid or conjugated to a solid phase, fluoresces under this illumination and allows qualitative observations on particles synthesized for colloidal processing.

1.2.2. Scanning Electron Microscopy (SEM)

The electron microscope was invented by Ernst Ruska in 1931, and only two years later exceeded the magnification attainable in optical system.[25] The magnification in most* optical imaging systems is limited on a theoretical basis by the Abbe diffraction limit, about one half of the wavelength of visible light ($\frac{\lambda}{2} \cong 250\ nm$).[26] Electron imaging systems, utilizing a beam of shorter λ, can observe features much smaller than optical microscopes. The first electron microscopes were analogous to a transmission light microscope, with the image generated by either attenuation (bright field) or diffraction (dark field) of incident radiation which illuminates the entire field simultaneously. The scanning electron microscope extends this concept by converging and rastering the beam over specific x,y coordinates on a sample and collecting spatially resolved signals. A block diagram is presented in Figure 1-3 and illustrates beam generation and conditioning, as well as the scanning apparatus and signal processing necessary to recreate an image.

* Some optical methods, for example, near-field scanning optical microscopy overcomes the diffraction limit by limiting propagation of incident light with an aperture much smaller than λ. An evanescent (non-propagating) wave is generated around this aperture and interacts with the sample surface. Because the wave does not propagate beyond the near-field, the signal has high spatial resolution.

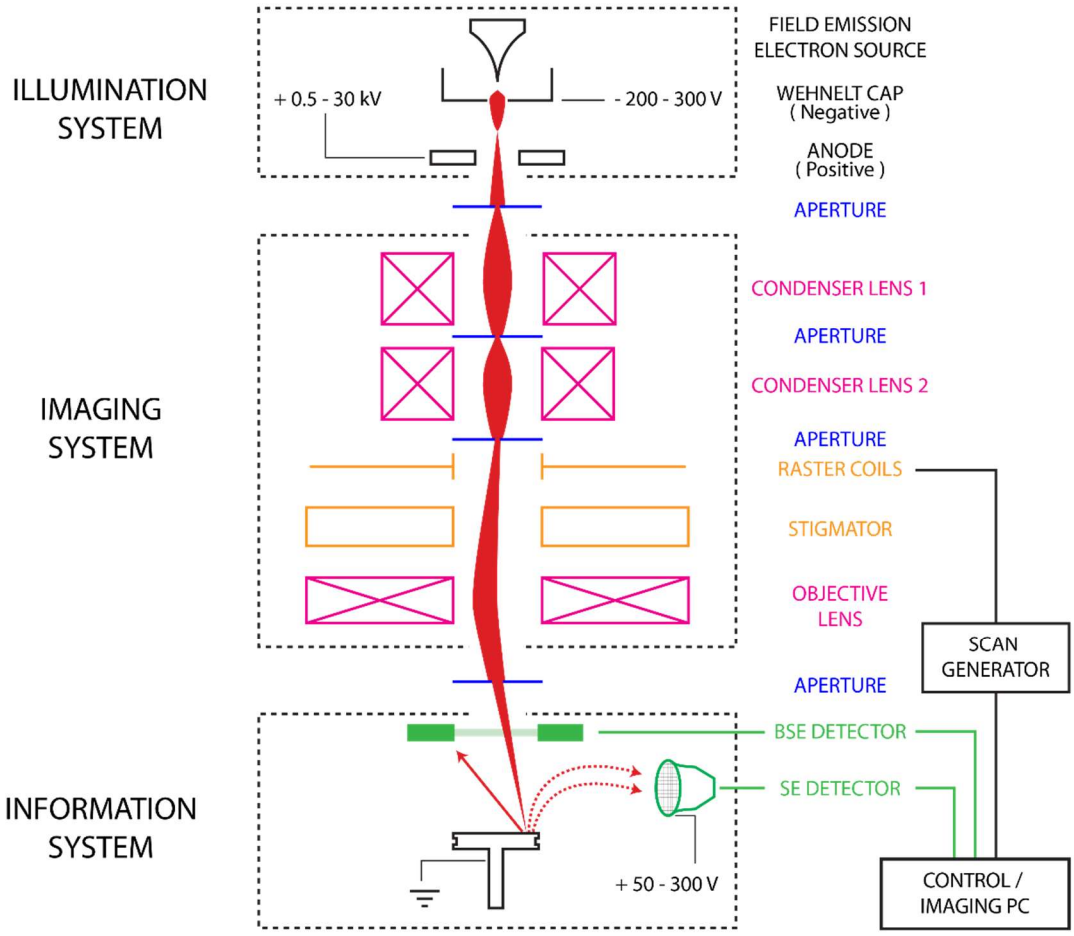

Figure 1-3: Schematic illustration of a scanning electron microscope (SEM). The illumination system generates an electron beam (red) which is conditioned in the imaging system and generates signals in the information system, collected by detectors (green)

The electrons in an SEM are generated by a filament or field emission gun (FEG) and shaped into a beam by the compressive electromagnetic force from the negatively charged Wehnelt cap. This beam is accelerated into the imaging column with a strong positive potential applied to an anode. Condenser lenses and apertures collimate the beam before it reaches raster coils, which deflect the electrons to a specific point on the sample. The objective lens determines the distance at which the beam converges on itself (the working distance) and is therefore responsible for focusing the system.

Secondary electrons (SE) are scattered inelastically from the sample and are lower energy than the incident beam. Because they move relatively slowly, SE can be attracted toward a positively biased detector. This detector does not require line-of-sight with the observed surfaces and can therefore collect information on the texture and morphology of features in the sample. Elastically scattered electrons have nearly the same energy as the incident beam and are therefore not significantly deflected from their direction of propagation, which is strongest normal to the sample surface. The flux of these backscattered electrons is a function of local electron density and can therefore be used to infer information on the chemical composition of the observed features. The image is generated by reassembling these signals into the array of (x,y) coordinates targeted by the raster coils.[27]

Unless otherwise noted, all electron microscopy was performed on a FEI Magellan SEM equipped with a FEG electron source and Everhart-Thornley (secondary electron) detector.

1.2.3. X-ray Diffraction (XRD)

Constructive or destructive interference between waves is characteristic of the phase relationship between them. Periodic interference of propagating waves is known as diffraction and the resulting pattern is characteristic of the experiment geometry. X-ray diffraction is a technique to measure the internal dimensions of a crystal from this pattern. These so-called d-spacings are dependent on several factors, most importantly symmetry and short-range order, and are unique to a crystal and can be used as a rudimentary tool for phase identification. A schematic of an XRD experiment is illustrated in Figure 1-4.

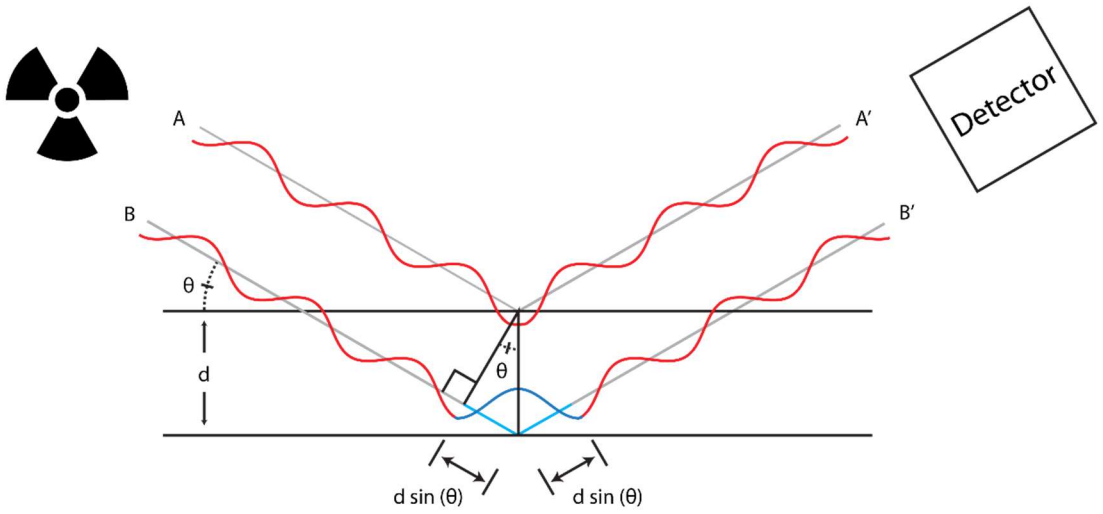

Figure 1-4: Schematic illustration of Bragg conditions necessary to collect a diffraction peak during an X-ray diffraction (XRD) experiment.

An X-ray source illuminates a sample with a collimated, coherent, and monochromatic beam. Consider two of these beams propagating toward a sample (A and B in Figure 1-4). The beams land on the sample at an angle θ and are scattered by electrons in the sample, which approximate atomic positions. In Figure 1-4, incident X-rays A and B are scattered from atoms on adjacent planes, separated by distance d and therefore have a path length difference equal to $d \sin\theta$ before the scattering event. The scattered X-rays A' and B' propagate toward a detector, which will register a signal provided A' and B' are in phase such that they interfere constructively. To satisfy this prerequisite, the total path length difference for the two X-rays (blue, in Figure 1-4) must be a multiple of the wavelength λ, giving rise to the Bragg relationship:

$$n\lambda = 2\mathrm{d}\ \sin\theta$$

Collected data from an XRD experiment is typically plotted as intensity *vs.* diffraction angle, reported as °2θ. Example data is shown in Figure 1-5.

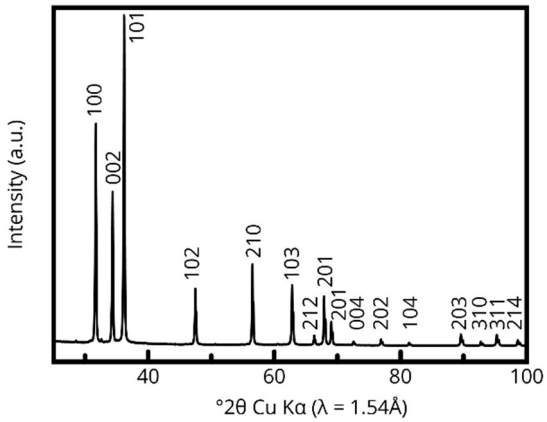

Figure 1-5: Example XRD data showing peaks characteristic of a crystalline phase. The data is matched to hexagonal zinc oxide with Miller indices above each peak.

Peak position and intensity are characteristic of (and often unique to) a crystalline phase. With data collected from the experiment, peaks can be compared to a database and a pattern matched to a crystalline material. Within this dissertation, XRD is used only for phase identification, but more complicated analyses can be performed to extract information on (for example) microstrain, crystallite size, or preferred orientation in a polycrystalline solid.

1.2.4. Electrochemical Measurements

To determine the performance of electrodes described in Chapters 4 and 5, a variety of electrochemical tests were performed with primarily a Solatron CellTest System (Model 1470E, Ametek Inc, Berwyn PA) or a Keithley Sourcemeter (Model 2400, Tektronix, Inc, Beaverton OR). These instruments are controlled with computer scripts through either proprietary CorrWare/Multistat software (for the Solartron instrument) or custom Python 3 scripts and the PyVISA library (for the Keithley instrument).

1.2.4.1. Cyclic Voltammetry (CV)

A schematic experimental setup and representative data for CV is reported in Figure 1-6

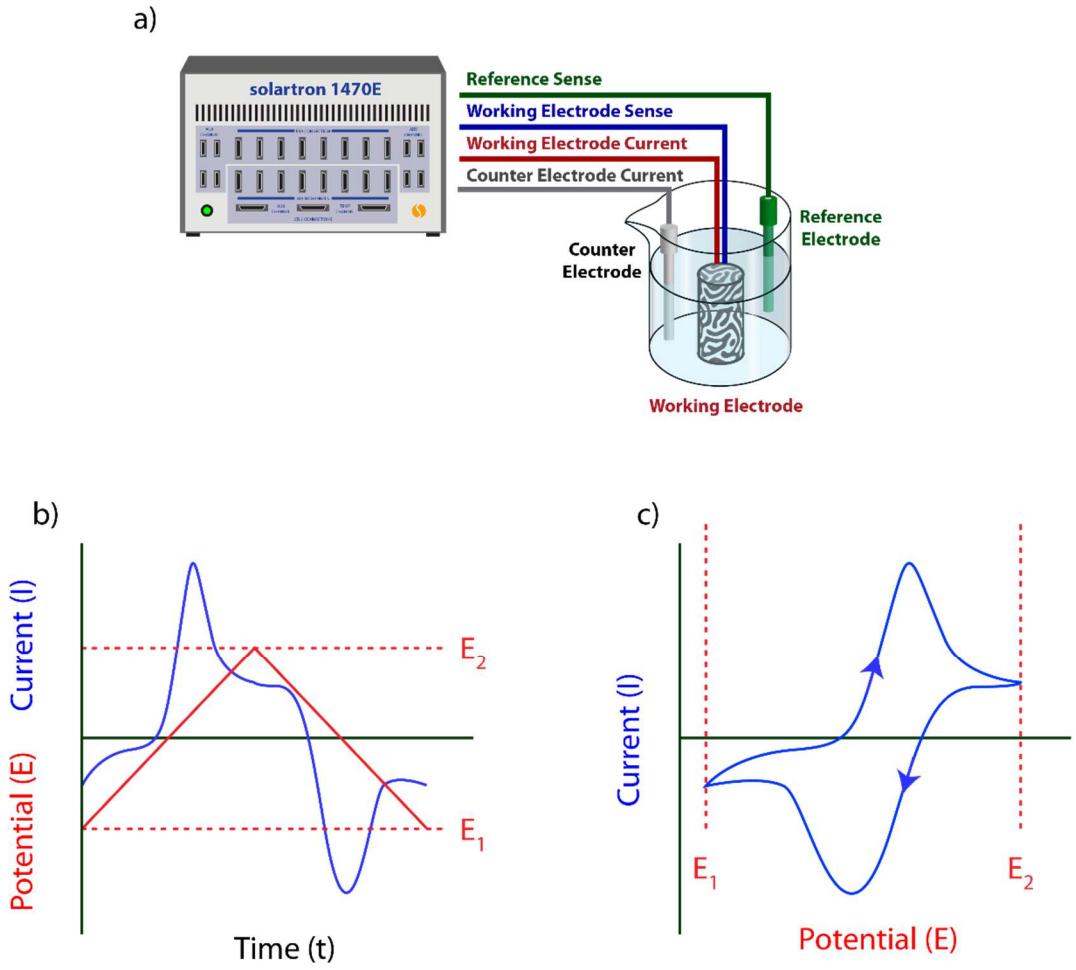

Figure 1-6: (a) Schematic illustration of a three-electrode experimental setup for cyclic voltammetry experiments. (b) Example data collected over the course of the experiment (c) Data from (b) replotted as I vs. E.

Current (I) between a working electrode and a counter electrode is measured as a function of potential (E) at the working electrode. Ideally, E is measured against a third reference electrode, which is non-polarizable (constant E). Peaks in current can be attributed to specific reactions in a system. The test proceeds by sweeping E of a working electrode linearly between limits (E_1, E_2 in Figure 1-6b) and measuring current through a counter electrode. Plotting these data as *I vs. E* results in the characteristic 'duck curve' (Figure 1-6c).[28]

1.2.4.2. Galvanostatic Charge / Discharge

Galvanostatic experiments were carried out by supplying constant I between a working electrode and a counter electrode and measuring E as a function of time.

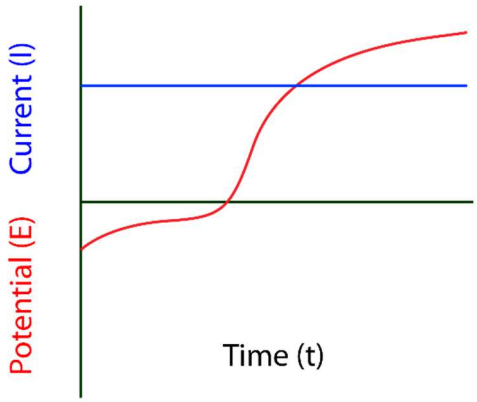

Figure 1-7: Example data from a galvanostatic experiment

For experiments in Chapters 4, galvanostatic experiments were carried out between E limits and the capacity of experimental electrodes calculated as the integral of current with respect to time, $\int I\,dt$.

In Chapter 5, the overpotential (η) required to drive a reaction is measured at the end of the galvanostatic experiment. In this case, constant I is supplied until the system reaches steady state conditions, after which a single measurement is extracted from the data.

1.3. Structure of the Dissertation

The following chapters of this dissertation are structured as follows: Chapter 2 introduces bijels, a unique class of soft materials, and the fundamental science behind their formation. The morphology and topology of these materials is discussed and compared quantitatively to similar

porous media in Chapter 3. These two chapters provide a basis with which to explore electrochemical functionalization of the bijel morphology and microstructural-based techniques to mitigate electrode deactivation. The first example is presented in Chapter 4, in which rechargeability of two different styles of Zn/ZnO electrodes (bijel-templated *vs.* those derived in a stochastic process) are compared. The bijel-derived electrodes consistently retained more recoverable capacity than the stochastic type throughout charge cycling. Simulations suggest capacity loss in this system is related to electrical disconnections inspired by the discharge process, and that the advantage in spinodal-like electrodes is derived from a more homogenous current density and resistance to these disconnections. In Chapter 5, Bijels are converted into gas-evolving electrodes, which can be deactivated by shielding of active surfaces imposed by the evolved product. Observations on gas escaping these pores and electrochemical measurements together suggest a smaller impediment to the product escaping through the pore phase of a spinodal-like sample compared to stochastic analogs.

2. On Bijels and Their Derivatives

The bicontinuous interfacially jammed emulsion gel (bijel) is a class of soft matter that forms by kinetically arresting spinodal decomposition phase separation. Driven by the reduction of interfacial energy between phases, bijel morphology develops in a dynamically self-similar fashion with a near-minimal surface. The following sections describe briefly the fundamentals of spinodal decomposition and how bijel processing is used to stabilize its unique microstructure. A brief discussion of materials templated from bijels follows.

2.1. Introduction

Porous materials are used in a broad range of applications, for example, as electrodes,[23,29] perfusion bioreactors,[30,31] microfiltration materials,[32,33] and tissue regeneration scaffolds.[34,35] Scalable generation of three-dimensional (3D) porous materials has been achieved using a variety of processing techniques including porogen templating,[36,37] powder pressing,[38,39] high internal phase emulsion polymerization,[40,41] and electrospinning.[42,43] While these techniques can yield materials with tunable porosity and average pore size, the pore and solid volumes are typically distributed in a random and heterogeneous manner, which can negatively impact their utility. For example, in applications that involve mass transfer or fluid flow through the pore phase, a random distribution of pores can result in transport pathways with drastically different resistances, as well as constrictions, discontinuities, and isolated pockets, in turn rendering part of the material underutilized or resulting in low permeability. Similarly, a randomly architected solid phase can result in weak spots, in turn limiting the mechanical properties salient to emerging porous material applications.[44] Inverse opals have been considered as an alternative for tissue engineering[45] and electrochemical[46] applications due to their highly ordered pore structure and bicontinuity.

However, these materials suffer from difficulty of scale-up to macroscopic sizes, and a pore structure that consists of spherical pockets interconnected by much smaller throats, which again limits their transport properties.[23,36,47] More consistent pore size and surface curvature throughout the structure is expected to benefit transport characteristics of porous materials.[48,49] Mathematically defined minimal surfaces such as the Schoen's G (gyroid) and Schwarz P[50] have received interest as microstructures that address this need.[51,52] However, experimental realization of such structures requires deliberate design and fabrication and can be time consuming or cost prohibitive. In contrast, a naturally occurring, dynamically self-similar structure evolves during spinodal decomposition, a phase separation process driven by interfacial minimization in mixtures with partial miscibility between their constituents, resulting in many of the same important microstructural qualities.[53,54]

2.2. Spinodal Decomposition

Spinodal decomposition was first observed in the early 1940's *via* sidebands in XRD peaks, suggesting demixing distinct from nucleation and growth, which presents as a second series of peaks (i.e. another phase with a unique pattern).[55] The concept was further explored in one dimension by Mats Hillert in 1955[56] and subsequently generalized by John Cahn and John Hilliard[57]

During this unique type of demixing, immiscible phases are separated into compositionally distinct bicontinuous domains.[57] It is dissimilar to a nucleation and growth process which involves a large free energy barrier to form the initial microscopic clusters. In both processes, minimization of interfacial energy drives microstructural development, but the dominant mechanisms responsible for this coarsening are distinct. Coarsening during a growth and nucleation process proceeds through aggregation and Ostwald ripening, which require either

forming new interfaces or dissolution of the discontinuous phase, while in the spinodal system, microstructural evolution occurs through a strictly diffusive process along the continuous domains.[55]

Some thermodynamic conditions must be met for spinodal decomposition to be the favored demixing process. To help discuss these, a schematic phase diagram is shown in Figure 2-1a, alongside a curve representing the temperature dependent free energy in Figure 2-1b.

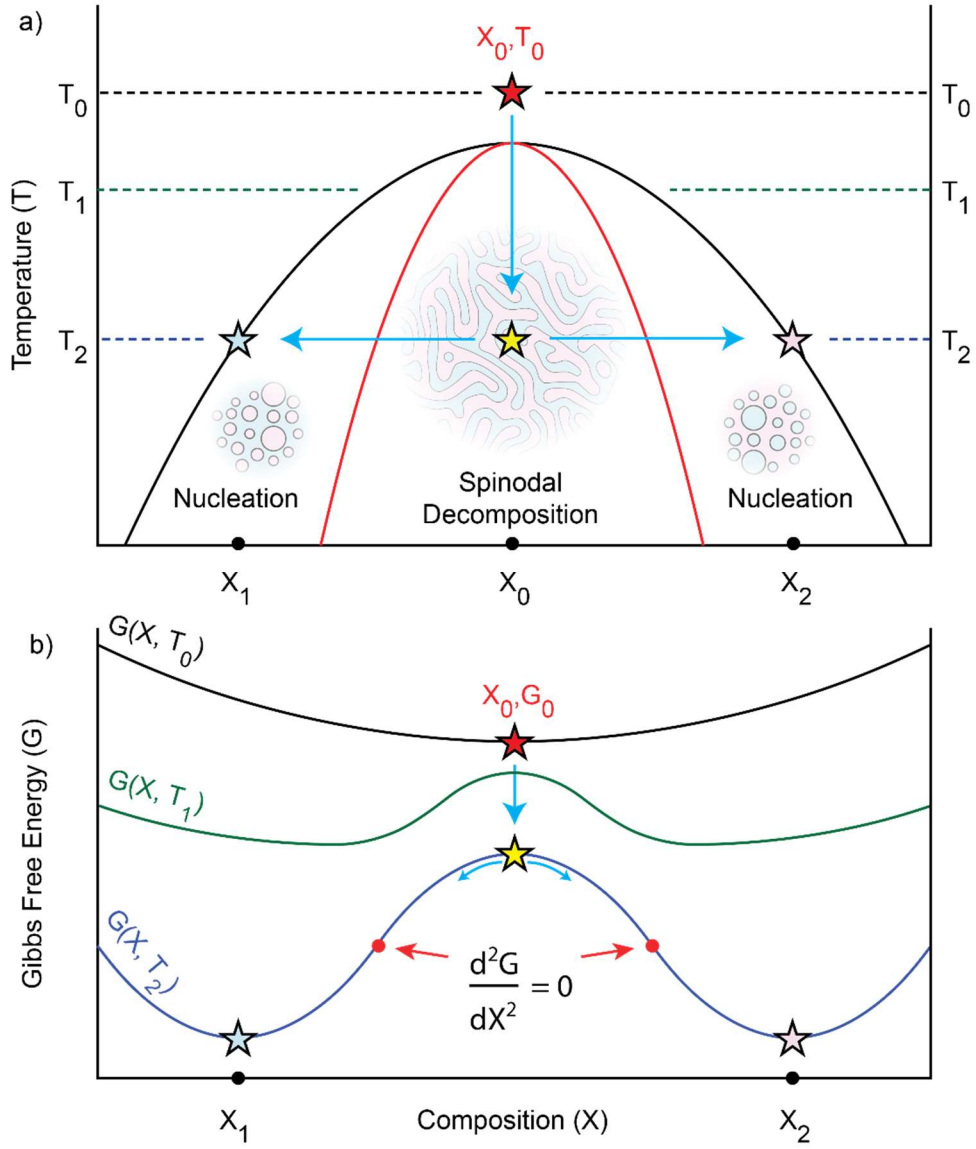

Figure 2-1: Phase diagram (a) and free energy (b) diagram describing spinodal decomposition

As seen in the phase diagram in Figure 2-1a, a binary mixture at composition X_0 will be single phase at high temperatures (red star). If this alloy is quenched quickly into the immiscible region (for example $T = T_2$), the composition is initially homogenous and the free energy is relatively high (G_0 in Figure 2-1b). The mixture will phase separate and approach the compositions at minima in the $G(X,T)$ curve (marked by blue and pink stars in panel b).

The energy balance during small compositional variance plays an important role in determining the dominant demixing process. For compositions at or near the $G(X,T)$ maxima, as in the example of X_0 in Figure 2-1, the change in energy is negative and both phases quickly approach X_1 and X_2 and separate *via* spinodal decomposition. Small deviations from this critical point composition may still separate in this fashion provided the change in energy associated with one phase is enough for the other to overcome the $G(X,T)$ maximum and approach its own minimum. Conversely, large deviations from the critical point will behave differently during this process, where discontinuous nuclei form and grow through aggregation or Ostwald ripening (nucleation and growth). Observations on the curvature in the $G(X,T)$ curve (Figure 2-1b) help illustrate this. Regions that are concave up ($\frac{d^2G}{dX^2} > 0$) demix *via* nucleation and growth, while concave down regions ($\frac{d^2G}{dX^2} < 0$) separate through spinodal decomposition. Inflection points (marked red) in the $G(X,T)$ curve establish compositional limits for these processes at a temperature T.

To help visualize the resulting microstructure, 3D models of spinodal decomposition simulated through the Cahn-Hilliard equation are presented in Figure 2-2.

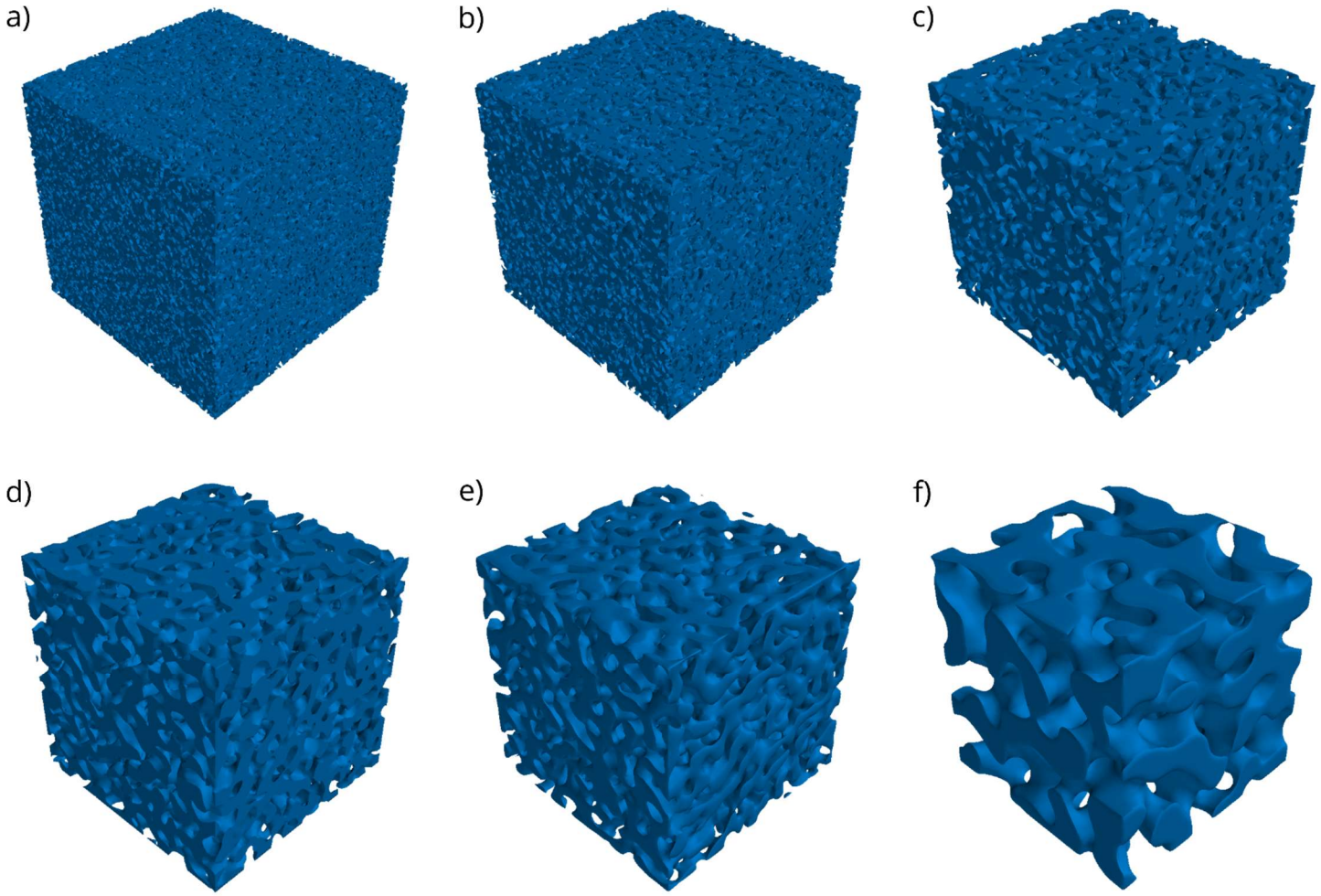

Figure 2-2: Isosurfaces in a 3D solution to the Cahn-Hilliard equation, which approximates spinodal decomposition. The isosurfaces are from solutions at: (a) 1 timestep (b) 10 timesteps (c) 100 timesteps (d) 1000 timesteps (e) 10000 timesteps (f) 100000 timesteps

2.3. Particle Adsorption

Particles stabilizing fluid interfaces was first observed by Walter Ramsden in 1903[58] and explored in detail by Spencer Pickering in 1907.[59] These so-called Pickering emulsions have since been well incorporated into cosmetics and food sciences, among other industrial applications.[60] Recently, more advanced applications of colloid science have shown promise in areas such as drug delivery, catalysis, and composite materials. These systems are still under investigation to better understand how stability and rheology are related to the adsorption mechanisms.

To reduce free energy in a system, a particle can become strongly associated with (adsorb to) the fluid-fluid interface. This concept is shown schematically in Figure 2-3.

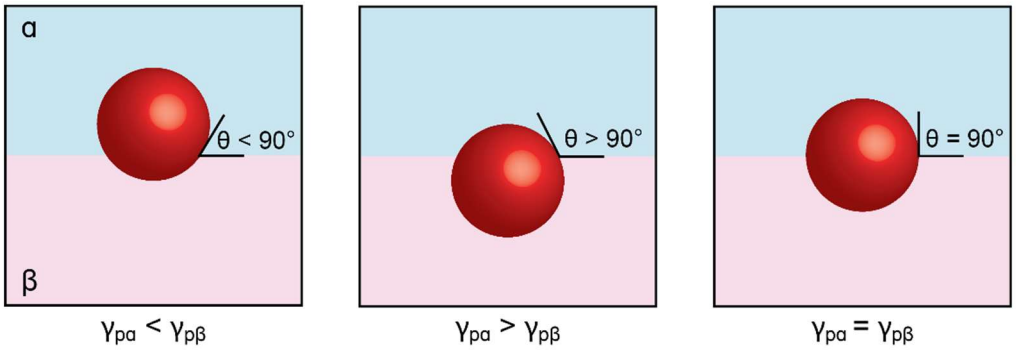

Figure 2-3: A particle adsorbed to a fluid-fluid interface.
The relative interfacial energies determine displacement into a phase.

If the particle has equal interfacial energy with the fluids in an emulsion, it will present an equal amount of its own surface area to the constituent phases (neutrally wetting). If this equality is broken, the particle will be displaced into the phase with which it has a lower interfacial energy. This is described quantitatively by Young's equation, which relates the interfacial energies with the contact angle created at the junction of these three phases:

$$\cos\theta = \frac{\gamma_{p\beta} - \gamma_{p\alpha}}{\gamma_{\alpha\beta}}$$

Where $\gamma_{\alpha\beta}$, $\gamma_{p\alpha}$, and $\gamma_{p\beta}$ are energies for α-β, particle-α and particle-β interfaces, respectively and θ is the angle measured into the α phase, as illustrated in Figure 2-3.[61]

2.3.1. Arrested Spinodal Decomposition

Bijels bear the geometrical fingerprints inherent to spinodal decomposition, having been derived through this method of demixing.[54] First simulated in 2005 by Stratford *et al.*[62] and experimentally realized in 2007 by Herzig *et al.*,[63] bijels are generally formed by dispersing colloids in a mixture of semi-miscible fluids and initiating demixing through a chemical or thermal stimulus. During demixing, adsorbed particles at the fluid-fluid interface jam, which halts the process and marks a sharp transition from liquid-like to gel-like properties in the suspension.[64,65] The resulting out-of-equilibrium gel comprises bicontinuous liquid phases separated by a percolating, interfacial area-minimized, jammed nanoparticle monolayer. This concept is illustrated schematically in Figure 2-4 and demonstrated experimentally in Figure 2-5.

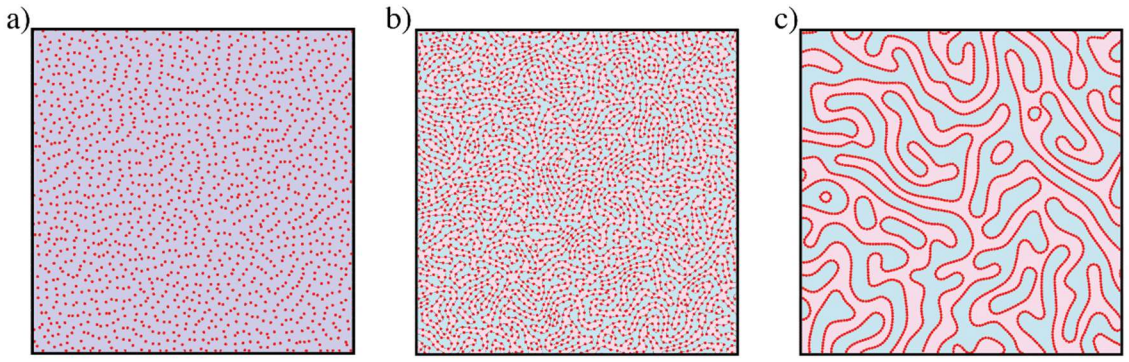

Figure 2-4: Adsorbed particles arresting spinodal decomposition to create a bijel. (a) Particle suspension in a homogeneous medium. (b) Spinodal decomposition, particle adsorption to the fluid-fluid interface. (c) Particles in contact with neighbors, arrested spinodal decomposition (bijel)

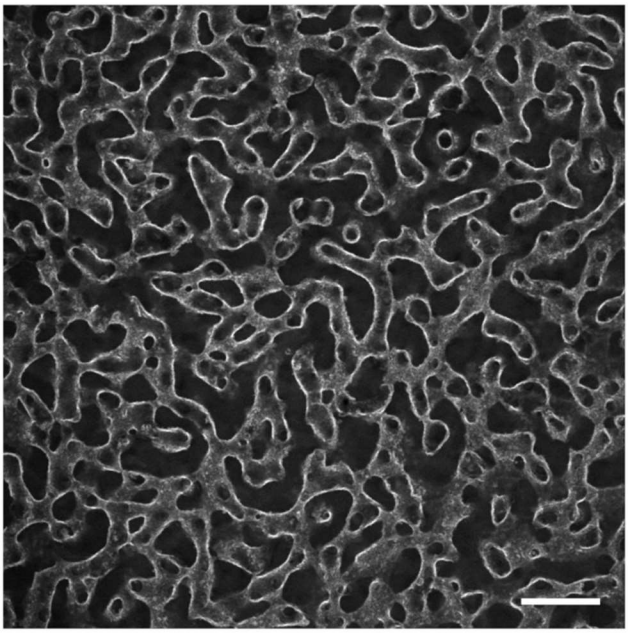

Figure 2-5: Confocal micrograph of a bijel. In this example, silica nanoparticles labeled with rhodamine B (bright pixels in micrograph) have kinetically arrested spinodal decomposition of water and 2,6-luitidine. Scale bar: 100 μm.

Lee and Mohraz demonstrated using confocal microscopy 3D reconstructions that this interface indeed displays the characteristics of a spinodal surface with negative Gaussian curvature and vanishing mean curvature, and pioneered materials processing routes to synthesize polymeric, ceramic, and metallic constructs using bijels as templates, thereby imprinting the morphological attributes of the parent template onto the resulting porous materials.[66] Further, Reeves *et al.* quantified bijel topology using interfacial curvature, as a function of both the colloidal particle size and depth of the phase separation quench, also showing that the interface has near minimal surface signatures.[67] Witt *et al.* demonstrated that the bijel characteristic domain size and subsequent pore size of the templated solid could be tuned across a wide range (5-800 μm) relevant to the applications discussed in Section 2.1 by adjusting colloidal particle loading and surface chemistry.[68]

2.4. Materials Templated from Bijels

The bijel structure has been previously converted to a variety of materials, including polymers, metals, ceramics, and composites that inherit the unique morphology. Generally, this templating begins by exploiting the incompatibility of the two fluids and segregating monomers or oligomers to one of the phases before polymerization, which stabilizes the structure. A number of functional bijel-derived materials have since been developed from these polymeric scaffolds for applications in energy systems, catalysis, or human health, including 3D electrodes for electrochemical energy storage and conversion,[23] composite electrolytes,[69] cell delivery composites,[70] and separation fibers.[71,72] Some processing routes for templating functional materials from a bijel are illustrated schematically in Figure 2-6, and a photograph of these templated materials is presented in Figure 2-7.

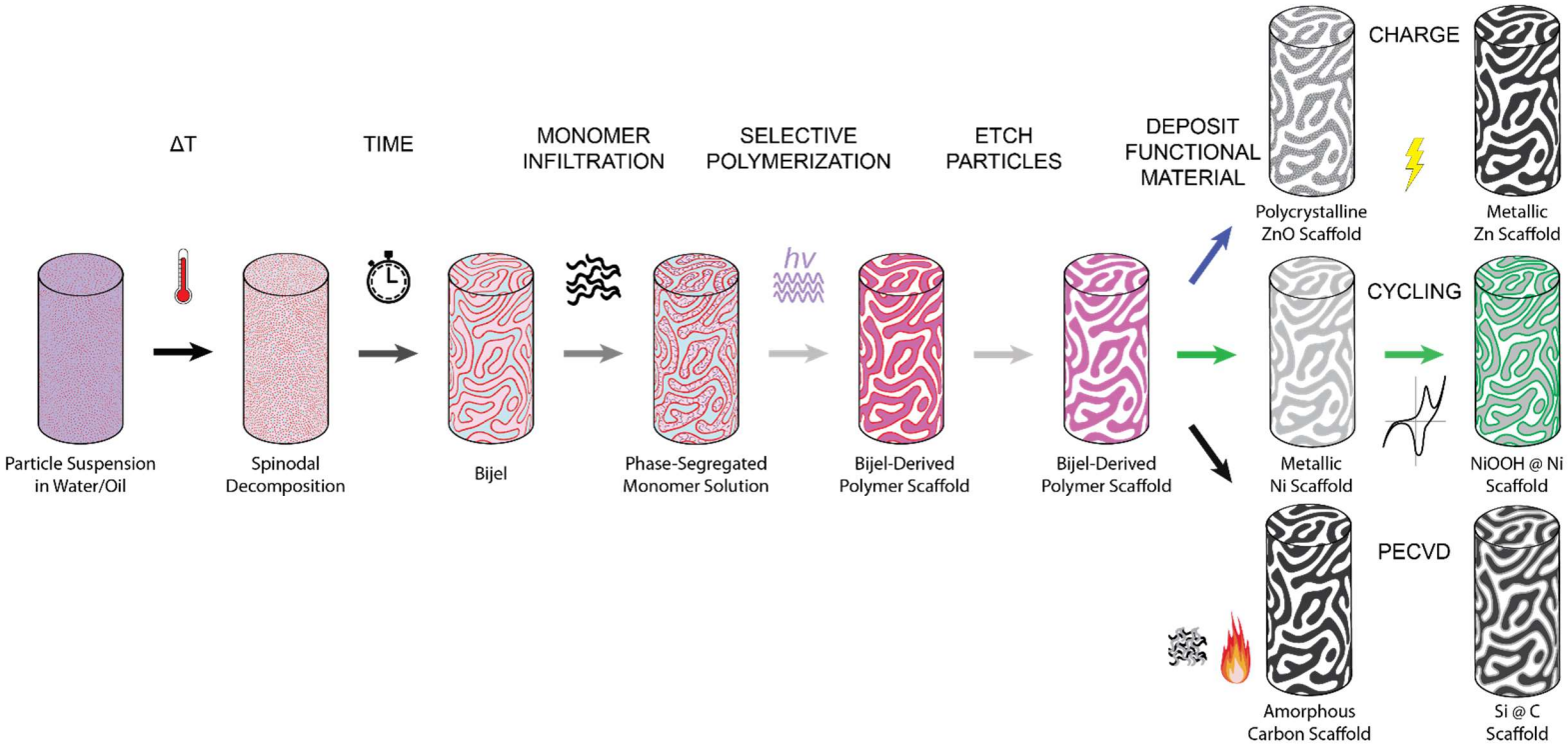

Figure 2-6: Using a bijel structure to template a polymer scaffold and functionalizing the scaffold by active material deposition.

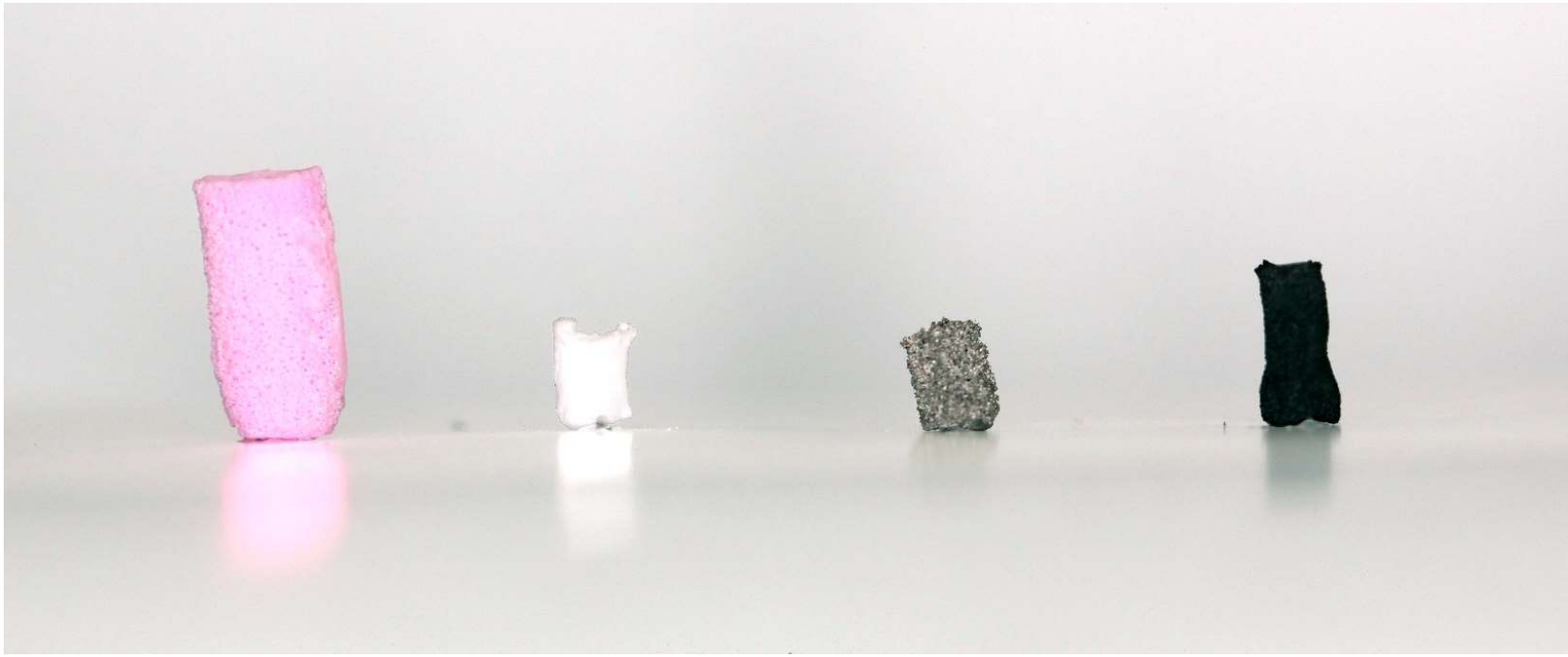

Figure 2-7: Materials templated from a bijel structure. From left to right: PEGDA, Zinc Oxide, Nickel, Carbon

3. On Morphology and Microstructure of Bijel-Derived Materials

3.1. Abstract

The geometric arrangement of pore features is a critical aspect of three-dimensional (3D) materials design for a diverse set of applications. Transport properties such as diffusivity and conductivity are intimately linked to this pore arrangement, and thus, significant effort has been invested into designing processes and systems that offer predictable final morphologies. Minimal surface structures comprising bicontinuous, symmetric phases are predicted to provide optimal transport properties. Here, bijels were used as template structures to generate carbon and polymer scaffolds, and morphological characterization of distinctive features was carried out on 3D reconstructions of micro-computed tomography (μCT) data. Specific emphasis is placed on the characterization of size distribution, interfacial curvature, continuity, tortuosity, and self-similarity exhibited by pore networks within these structures. Microstructural attributes are compared to three additional porous media to demonstrate bijel-derived materials as near-minimal surface structures with high transport potential.

3.2. Introduction

To better understand how the unique microstructure of bijel-derived materials contributes to their performance in applications discussed previously, a more complete characterization of these near-minimal surface structures, and their comparison to other porous materials that have commonly been used in these applications, is needed.

Computational methods have been previously employed to analyze coarsening[73] and channel size distributions[74] in spinodal structures formed by Cahn-Hilliard[57,75,76] and Allen-Cahn dynamics.[77] Further, Frijters and Harting used Lattice Boltzmann simulations to examine tunable fluid permeability as a function of particle hydrophobicity and volume fraction

of solidified bijels.[78] Nevertheless, a comprehensive microstructural analysis of experimentally-generated bijel-derived materials, particularly as relevant to their transport properties, remains lacking. Herein, we use micro-computed tomography (μCT) to generate micrometer-resolved 3D reconstructions of two bijel-derived materials – one processed as an electrically conductive copolymer, and the other pyrolyzed to form a carbon scaffold – and three other technologically relevant porous materials: porous metal, polymerized high internal phase emulsion (polyHIPE), and inverse opal. We quantitatively analyze and compare among these the interfacial curvature, pore network geometry, connectivity, tortuosity, and self-similarity, and demonstrate that bijel-derived materials possess a unique combination of microstructural features salient to their transport properties, which, importantly, are maintained across different length scales due to the dynamic self-similarity that is inherent to spinodal decomposition.

3.3. Materials and Methods

3.3.1. Preparation of Porous Materials

All reagents were used as received from Sigma-Aldrich unless otherwise stated.

3.3.1.1. Bijel-Derived Materials

3.3.1.1.1. Particle Synthesis

Silica nanoparticles with an average diameter of 440 nm and a coefficient of variation of 4.7% were synthesized using a modified Stöber process.[79] Briefly, 12.5 mg rhodamine B isothiocyanate (RBITC) was conjugated to 26.3 μL 3-aminopropyltriethoxysilane (APTES, TCI America) in 10 mL anhydrous ethanol by stirring at room temperature for 24 hours. The resulting solution was then split evenly into two flasks each containing 44 g ethanol, 10 mL 18.1M ammonia solution (Fisher Scientific) and 4.180 mL tetraethylorthosilicate (TEOS) and stirred at room temperature for 24 hours. The resulting silica nanoparticles were rinsed with deionized

water repeatedly *via* centrifugation and dried at 135°C under vacuum for 28 hours to achieve near-neutral wettability with respect to Milli-Q water (Millipore, 18.2 MΩ·cm at 25ºC) and 2,6-lutidine.

3.3.1.1.2. Bijel-Templating of Polymer Scaffolds

Silica nanoparticles were dispersed in Milli-Q water using an ultrasonic horn (Branson Ultrasonics) and mixed with 2,6-lutidine (mole fraction of 2,6-lutidine, $x_L = 0.064$). Samples were heated in a microwave (15 seconds, 230 W) to induce spinodal decomposition, then transferred to a 70°C oven to maintain sample temperature above the critical point (34.1°C). Polyethylene glycol diacrylate (PEGDA, M_n: 250 g/mol) was added to the top of each sample with 1% (v/v*)* 2-hydroxy-2-methylpropiophenone (Darocur® 1173, Ciba Specialty Chemicals) photoinitiator. Monomer was allowed to diffuse into the lutidine-rich phase for 4 hours before radical polymerization was carried out using UV irradiation for 100 seconds (Lumen Dynamics, wavelength: 320 – 390 nm, 100 W). The water-rich phase was drained from the system leaving a free-standing porous polymer scaffold. Silica nanoparticles were etched from the scaffold's internal surfaces overnight using 6M hydrofluoric acid (HF, Fisher Scientific).

3.3.1.1.3. Polymer Bijel Sample Processing

Poly(3,4-ethylenedioxythiophene) (PEDOT) was cast into a bijel-templated PEGDA scaffold to create an electrically conductive, PEGDA-PEDOT copolymer. For casting, PEG scaffolds were soaked in 3,4-ethylenedioxythiophene (EDOT) for 30 minutes, then placed in 0.195 g/mL iron(III) p-toluenesulfonate hexahydrate in isopropyl alcohol. Oxidative chemical polymerization was carried out in an oven at 135ºC for 1 hour. The copolymer sample was washed twice by sonication in isopropyl alcohol and dried under atmospheric conditions.

3.3.1.1.4. Carbon Bijel Sample Processing

A bijel-templated PEGDA polymer scaffold was treated with an oxalic acid/furfuryl alcohol solution (4 mg/mL) for 1 hour before heat treatment under vacuum at 135°C for 8 hours. The sample was then carbonized by pyrolysis under flowing argon at 800°C for 2 hours.

3.3.1.2. Porous Metal

A Metapor® air permeable composite used in vacuum forming molds (porous metal, nominal pore size: 15 μm) was purchased from McMaster-Carr and used as received.

3.3.1.3. PolyHIPE

A polyHIPE was synthesized following a method described in Sergienko *et al.*[80] Briefly, an aqueous phase containing deionized water, potassium sulfate, and potassium persulfate (90.0 g, 0.2 g, and 0.5 g, respectively) was added dropwise into a stirred organic phase containing styrene, divinylbenzene, and sorbitan monooleate (9.0 g, 1.0 g, and 2.0 g, respectively) in a 250 mL glass beaker to form an emulsion of 90% (v/v) aqueous in 10% (v/v) organic. The beaker was covered and placed in an oven maintained at 65°C for 18 hours for polymerization. The synthesized polystyrene polyHIPE was dried under vacuum at 60°C overnight. To enhance X-ray contrast, the polyHIPE was soaked in a solution of iron(II) chloride in acetone (61.5 mg/mL) for 2 days and dried under atmospheric conditions for an additional 2 days.

3.3.1.4. Inverse Opal

A colloidal crystal was formed by first loading 300 μL ethylene glycol into a 5 mm inner diameter glass cylinder adhered to a glass cover slip using polydimethylsiloxane (PDMS, Dow Corning). The cylinder was placed in a sonication bath, and approximately 6 mg soda lime silicate microparticles (123-127 μm diameter, Cospheric) were added to the cylinder every 15 minutes. After six cycles, the sample was left in the sonication bath for an additional 30 minutes.

Ethylene glycol was dried under vacuum overnight at 160ºC. To form connections between the glass microparticles, the crystal was annealed in a furnace held at 650ºC for 3 hours. The annealed crystal was infiltrated with PEGDA and 1% (v/v) Darocur® 1173 under vacuum for 30 minutes, which was subsequently crosslinked *via* UV irradiation of the top and bottom of the sample, 5 minutes each. The sample was treated with 6M HF for 1 week to etch the soda lime silicate microparticles, resulting in a PEGDA inverse opal. However, to enhance X-ray contrast, the μCT scan was performed with the particles in place.

3.3.2. Microstructural Characterization

3.3.2.1. Scanning Electron Microscopy and μCT

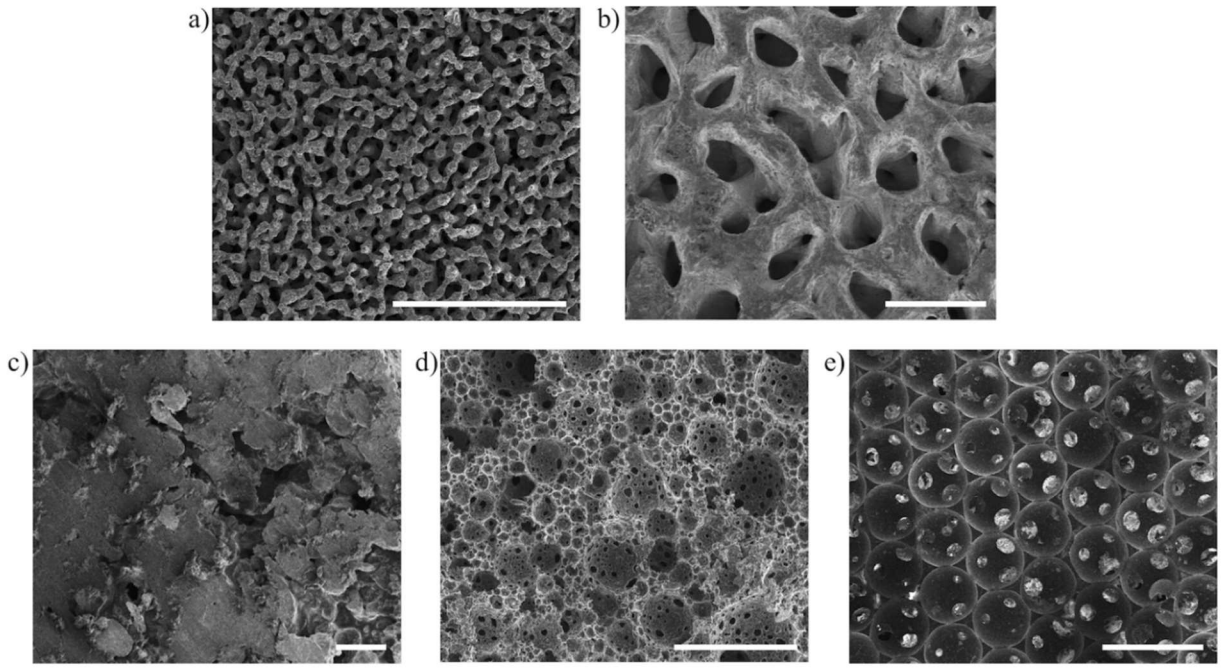

Figure 3-1: SEM micrographs of study samples: a) carbon bijel, b) polymer bijel, c) porous metal, d) polyHIPE, and e) inverse opal. Scale bar: 200 μm

Scanning electron microscopy (SEM) and μCT were performed at the UC Irvine Materials Research Institute (IMRI). SEM was carried out using a Quanta 3D FEG Dual Beam Microscope (FEI). Representative SEM micrographs of the sampled materials are presented in Figure 3-1.

μCT was performed using a Xradia VersaXRM-410 scanning system (ZEISS) capable of resolving 900 nm features under 40X magnification. X-ray scan image sequences were exported as digital imaging and communications in medicine (DICOM) files for processing.

DICOM μCT data were imported and processed in the ScanIP® module of Simpleware® (Synopsis), a proprietary meshing software capable of reconstructing image sequences into surface models.[81] Raw image data were segmented into 3D surface reconstructions of the solid and pore phases of each sample using pixel intensity thresholding.[82] A Gaussian smoothing operation was performed in ScanIP® with a radius of 1 pixel to match resolution of the initial scan and reduce jagged surfaces during processing. These smoothing operations developed by Simpleware® were designed specifically to preserve important microstructural details.[83] Stereolithography (STL) surface reconstructions were generated for all data.[84]

3.3.2.2. Triangular Meshes and Analysis

3D shapes are often approximated digitally with surface meshes comprising vertices (points on the surface) and faces (connections between vertices). To identify the solid and pore phases, the surface normal is also required for every face. Detailed models are efficiently described in computer memory with dynamic surface density of vertices. In other words, highly detailed regions are described with more vertices and smaller faces. To avoid under-sampling smooth regions, surface qualities such as curvature are measured at points sampled uniformly across the surface with spacing equal to the resolution in the μCT. Unless otherwise stated, all computer programs were written and executed using Python 3.6.3 with open source libraries, most notably PyMesh and Voro++.[85]

3.3.2.3. Medial Axis

For microstructural analysis, the domain size (or characteristic pore size) is often estimated by calculating the ratio of volume to surface area.[73,74] This single-value approximation offers no information on the domain size distribution, which can strongly impact the performance of porous materials. To better describe this distribution, the domain size at various points within the material's scanned volume is calculated using its solid and void medial axes, as detailed below.

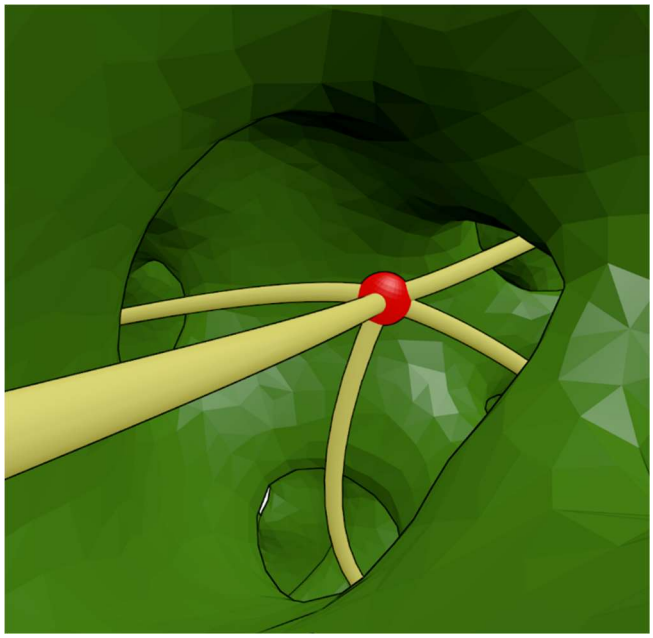

Figure 3-2: Illustration of a branch point (red dot) connecting several medial axes (yellow lines) in connecting pore channels of the carbon bijel (with its solid phase shown in green).

The medial axis was first proposed by Blum[86] as the "topological skeleton" to describe complex morphologies using a set of inscribed spheres and their respective centers, and is commonly used in shape analysis,[87] pattern recognition,[88] and path planning.[89] There exist several techniques for calculating the medial axis such as the original grassfire transform[86] or approaches based on Voronoi tessellation.[90] However, for data-rich 3D sets, many of these techniques are computationally impractical. For our data generated *via* μCT, the medial axis was resolved using the shrinking balls algorithm with appropriate de-noising filters

applied.[91,92] The shrinking balls algorithm projects a sphere tangential to a surface and aligned along the surface normal. The radius is reduced until no other surface points are contained inside the sphere, and the collective centers are gathered to approximate the medial axis for both solid and void phases. By resolving the medial axis and calculating the radius of the largest inscribed sphere, each point on the axis is associated with a local domain size (its corresponding sphere radius). To compare measurements across varying length scales and different materials, the data for each sample are divided by their respective mean values to center distributions around one before statistical analysis. To ensure an accurate representation of the domain size distribution, points exterior to the reconstruction boundaries are not included in the calculations, as they are not associated with a real solid-pore interface. The points at which the medial axis branches into two or more connecting pore channels are defined as branch points (Figure 3-2), which are identified using ScanIP® and used for characterizing the material's self-similarity (see Section 2.2.7).

3.3.2.4. Curvature

Curvatures were measured by fitting a quadratic function to each vertex and its neighboring vertices. The eigenvalues of the Hessian matrix of this quadratic are the principal curvatures, k_1 and k_2, which were multiplied for Gaussian curvature and averaged for the mean curvature.[44,93] A curvature toward the solid phase (convex) is defined as positive. Points at the (x,y,z) limits of the model, representing the limits of μCT sampling, are removed from analysis so that all calculations consider only the real internal surfaces in the model. To enable direct comparison between different samples, the Gaussian curvature was scaled with respect to the characteristic length by multiplying each measured value by the Voronoi area of each vertex to return the integrated Gaussian curvature, a dimensionless quantity.[94]

3.3.2.5. Connectivity

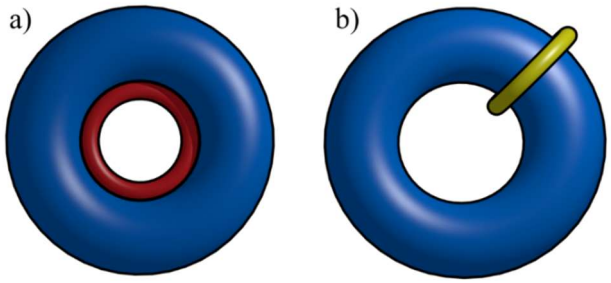

Figure 3-3: Illustration of a a) tunnel (red) and b) handle (yellow) on the surface of a toroid.

To characterize the phase connections in a structure, the genus of the object, g, is calculated from the vertices (n), edges (e), and faces (f) on its surfaces.[94,95] Informally, g is the number of cuts along non-intersecting closed curves that can be made onto an object, without separating the structure into multiple pieces. As a simple example, a topologically closed shape such as a sphere has $g = 0$ because it cannot be in two. Alternatively, a toroid can be cut once along its closed surface without breaking the shape, so it has $g = 1$, indicating a higher connectivity. For complex co-continuous structures, values of g much greater than one are expected, and can be calculated with the Euler-Poincare characteristic, χ, *via* the relationship $\chi = n - e + f$.[74] The value of g is subsequently calculated as $g = 1 - \chi/2$. For the structures measured in the current study, continuities in the void phase are defined as 'tunnels' and continuities in the solid phase as 'handles' (see Figure 3-4 for a schematic representation), both of which increase the value of g. Conversely, isolated solid and void regions (islands and cavities, respectively) decrease g, indicating a detriment to bicontinuity of the composite structure as a whole. However, the value of g does not make a distinction between the two phases, and purely concerns their connectivity.

To construct an intrinsic metric and enable comparison between different samples, the genus is divided by bulk volume and the cubed ratio of surface area to volume. The resulting scaled genus is a unitless, length-independent measure of connectivity.[96,97]

Continuity measurements are sensitive to size effects. If part of a continuous path is intersected by any of the interrogated volume boundaries, the intersection will falsely appear as a discontinuity in the model. To account for this, discontinuous features in contact with any of the x,y,z limits and with centroids within one domain size of these limits are ignored from analysis.

3.3.2.6. Tortuosity

To quantify tortuosity, the Euclidian distance between test points within the volume was compared to their connecting path along the medial axis. Briefly, a path was identified by randomly selecting an initial point from those representing the medial axis, and Dijkstra's algorithm was used to find the distance from this to every other point on the medial axis.[98] The process was repeated with 50 different initial points, and pathways were built outward until all locations along the medial axis had an associated pathway and distance from each initial point. Tortuosity, τ, was then calculated for each starting point as $\tau = L_e/L$ where L_e is the length of the longest measured path, and L is the Euclidean distance between its endpoints.[99] The arithmetic mean of the 50 independent τ measurements was used as the representative tortuosity, $\bar{\tau}$, for each sample.

For porous materials, the effect of microstructure on diffusivity of a given species, as a representative measure of transport properties, can be expressed by $F = D/D_e = \bar{\tau}^2/\varepsilon$ where F is called the formation factor, D is the intrinsic bulk diffusivity of the same species in the material filling the pore space (e.g. air), D_e is the effective diffusivity, and ε is the porosity defined as the ratio of pore volume to total volume.[99,100] This relationship has been used in the study of gas diffusion layers,[101] lithium-ion batteries,[102] and sedimentary rocks.[103] Archie's Law, $F = 1/\varepsilon^{m_A}$, is commonly employed in sedimentary rock analysis, where m_A is an empirical parameter specific to pore microstructure.[104,105] In the present study, m is

extracted using $\bar{\tau}$ and ε data. To provide a normalized metric for comparison of transport between the different materials, the calculated $\bar{\tau}$ was rescaled to 50% porosity using $\bar{\tau}_{0.5} = \bar{\tau}\sqrt{0.5^{1-m_A}/\varepsilon^{1-m_A}}$.

3.3.2.7. Self-Similarity

To assess self-similarity of the selected porous materials, in addition to the domain size distribution, the spatial arrangement of medial axis branch points and quantify the volume of the corresponding Voronoi cells. A Voronoi tessellation is a space-filling set of cells built around input points within a volume, constructed such that cell boundaries are equidistant from their respective points, and is used in computational fluid dynamics,[106] molecular charge distributions,[107] and structural biology.[108] In this study, medial axis branch points[86] calculated in ScanIP® (recall Figure 3-2) were used as the input seeds to create a Voronoi tessellation for each sample. Because of the finite spatial resolution of the medial axis calculation in ScanIP®, points where several medial axes meet (e.g. sphere centers in the inverse opal) can be falsely identified as a cluster of branch points. To prevent false oversampling in such cases, branch points that within 1/2 of a domain size from each other were collapsed to one point at their average position as illustrated in Figure 3-4. The filtered data were used as input positions for the Voro++ library[85] and a Voronoi tessellation was performed. The volume of each calculated cell was measured, and the resulting distribution was used to compare morphological self-similarity in each material.

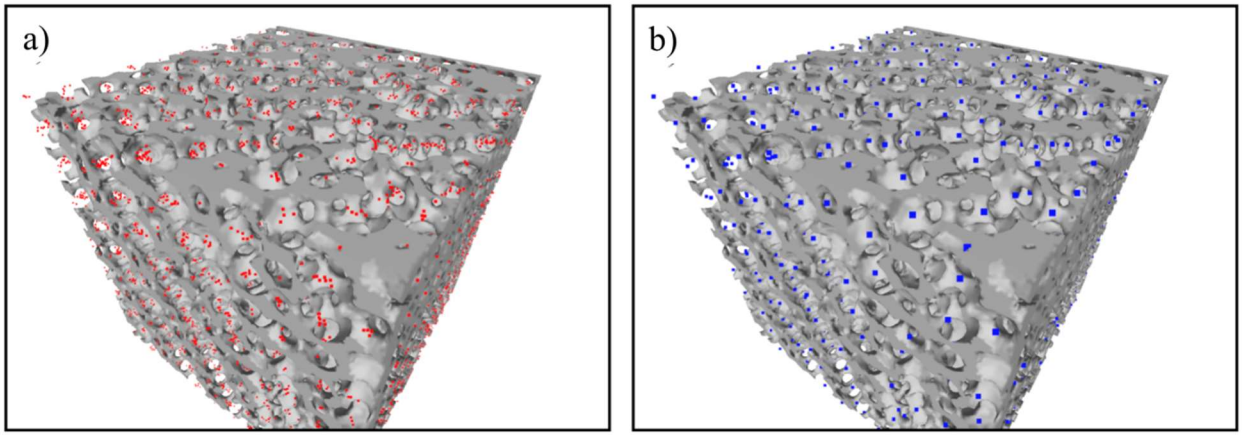

Figure 3-4: Illustration of branch points generated automatically (a) and the collapse of clusters (within ½ of a domain) to a point.

3.4. Results

3.4.1. Volume Reconstructions and Medial Axes

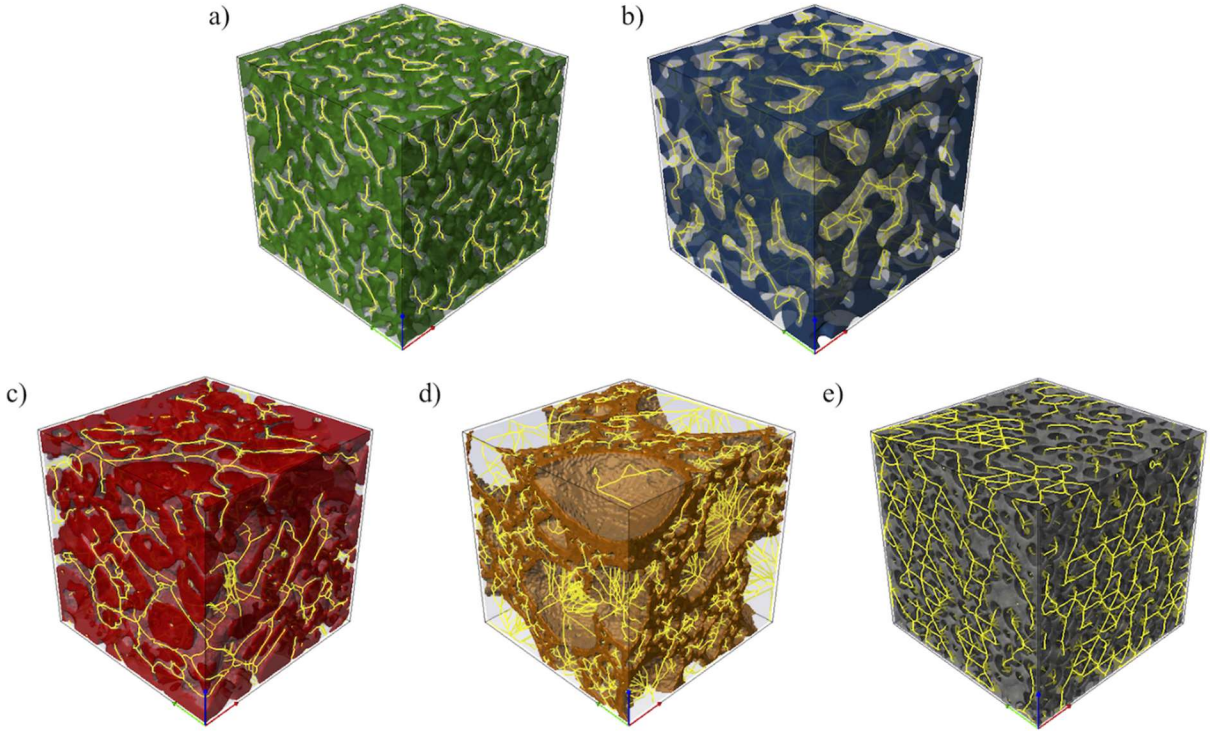

Figure 3-5: 3D reconstructions of μCT data. The colored mask for each reconstruction represents the solid phase of the scanned material. The medial axis in the pore phase is represented by yellow lines. Pictured are the a) carbon bijel, b) polymer bijel, c) porous metal d) polyHIPE, and e) inverse opal

The 3D surface reconstructions processed from μCT scans for all tested materials are shown in Figure 3-5. Additionally, the medial axes calculated in the pore phases are shown as yellow lines and will be used in the calculations of the domain size distribution (Section 3.4.2) and self-similarity (Section 3.4.6). Qualitatively, the surface reconstructions of the bijel-templated materials (Figure 3-5a and Figure 3-5b) resemble a spinodal-like volume. Conversely, the inverse opal (Figure 3-5e) is mostly periodic as a result of the crystalline template. The porous metal (Figure 3-5c) and polyHIPE (Figure 3-5d) show more random microstructures, particularly the polyHIPE which contains large pores due to the variable bubble sizes present in the template emulsion. A similar trend is observed in the medial axes, which exhibits periodicity in the inverse opal, and random turns and junctions in the other materials, although the bijel-derived materials' medial axes appear more uniform in density when compared to the porous metal and polyHIPE. The remaining analyses presented in this study will use sample-specific color coding consistent with the solid phase in Figure 3-5.

3.4.2. Domain Size Distribution

The characteristic domain size for both solid and void phases is measured through the medial axis transform for each structure. Histograms of these data centered around one are presented in Figure 3-6, and salient statistical measures of the domain size distributions are reported in Table 3.1. For the non-spinodal structures, qualitative descriptors of these distributions do not necessarily match between the solid and pore phases. For example, note the distributions of void and solid domains in the polyHIPE. By contrast, the solid and void domain size distributions in the bijel-derived materials mirror each other, which is a hallmark of symmetric structures derived from spinodal decomposition.[49]

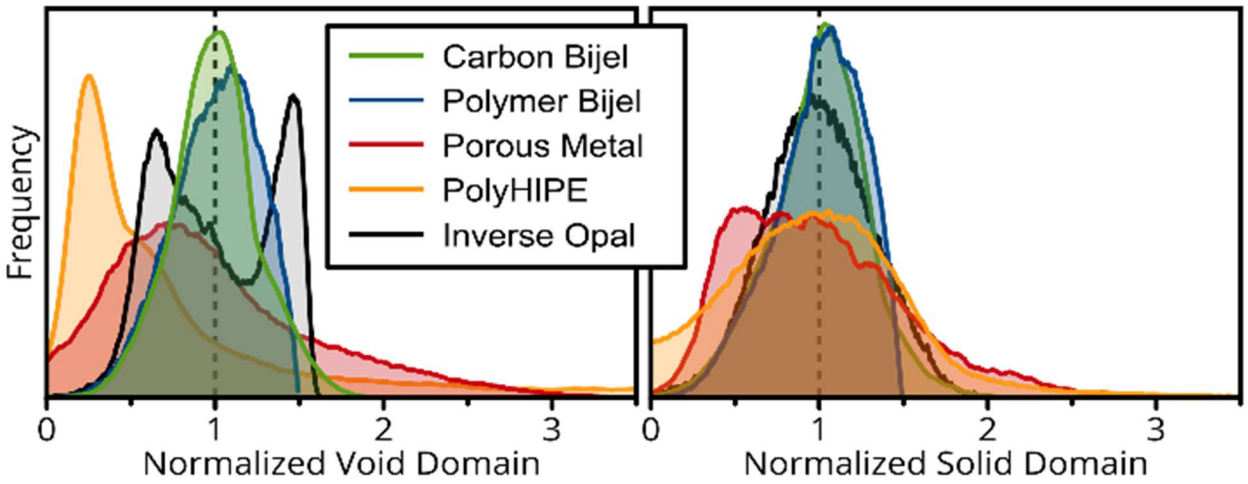

Figure 3-6: Histograms of the domain size measured as twice the distance from the medial axis to the material surface. The measured distance is normalized to the mean of the respective data set so that the distribution is centered around 1 (dashed line).

In addition, the bijel-derived samples exhibit a tight distribution about the mean, while the materials derived from polydisperse elementary shapes (porous metal and polyHIPE) have >50% coefficient of variance. In the inverse opal, the characteristic size of the solid phase shows variance intermediate to these limiting cases, which is likely due to the particular shape of the interstitial volume in the original crystal. The distribution for void size is bimodal, with normalized peaks around 1.44, corresponding to points within void pockets created by spheres, and 0.63, from tunnels between template spheres commonly referred to as pore throats.[109] The size distribution measured in the polyHIPE has a similar pattern, but with a much weaker mode from elementary shapes presenting as a shoulder to the main peak. We hypothesize this relatively weak mode to reflect the size polydispersity of the initial droplets. Constrictions in the pore phase, such as the pore throats observed in the inverse opal and polyHIPE samples, lower hydraulic permeability of a porous material by adding local resistance to flow.[47]

Table 3.1: Domain sizes calculated from MicroCT scans of porous media

	Carbon Bijel		**Polymer Bijel**		**Porous Metal**		**PolyHIPE**		**Inverse Opal**	
	Void	Solid	Void	Solid	Void	Solid	Void	Solid	Void	Solid
Mean (μm)	8.10	7.25	36.5	36.9	17.2	37.2	20.1	5.37	70.6	20.8
Median (μm)	8.08	7.37	37.4	38.4	15.1	34.8	10.5	5.24	68.1	20.7
Mode (μm)	8.16	7.52	39.2	40.3	11.7	20.9	4.80	5.22	45.6, 102*	19.7
Coefficient of Variance (%)	25.8	28.9	25.6	27.3	128	53.1	60.8	50.9	35.1	31.6

**Void phase in the inverse opal model has two modes, corresponding to tunnels (smaller mode) and the elementary shape (larger mode)*

High permeability is particularly important for applications that require uniform and predictable flow for reliable operation, such as filtration and porous catalysts. Advantages in uniform domain size distribution have also been recognized in electrochemical[110] and tissue engineering applications.[111] Bijel-derived materials can offer a unique advantage in such applications due to their uniform domain size distribution.[71,72]

3.4.3. Curvature

Curvature measurements are presented in Figure 3-7 as interfacial shape distributions (ISDs), 2D density plots of the principal curvatures k_2 *vs.* k_1.[112] Statistics on the mean and Gaussian curvatures are tabulated in Table 3.2. Because curvature (inverse length units) is inherently dependent on feature size, the measurements are normalized to the characteristic domain size to return a unitless curvature. Structures that approximate minimal surfaces are marked by a mean curvature approaching zero and dominantly negative Gaussian curvature.[67] This should present in the ISD as $k_2 \cong -k_1$, (i.e. a dense cluster of points near the blue dashed line in the second and fourth quadrants of each plot in Figure 3-7: ISDs for a) carbon bijel b) polymer bijel c) porous metal d) polyHIPE, and e) inverse opal. The blue dotted line shows k_2=-k_1.Figure 3-7). This clustering is observed only on bijel-derived samples, with observable deviation from the line for the other materials.

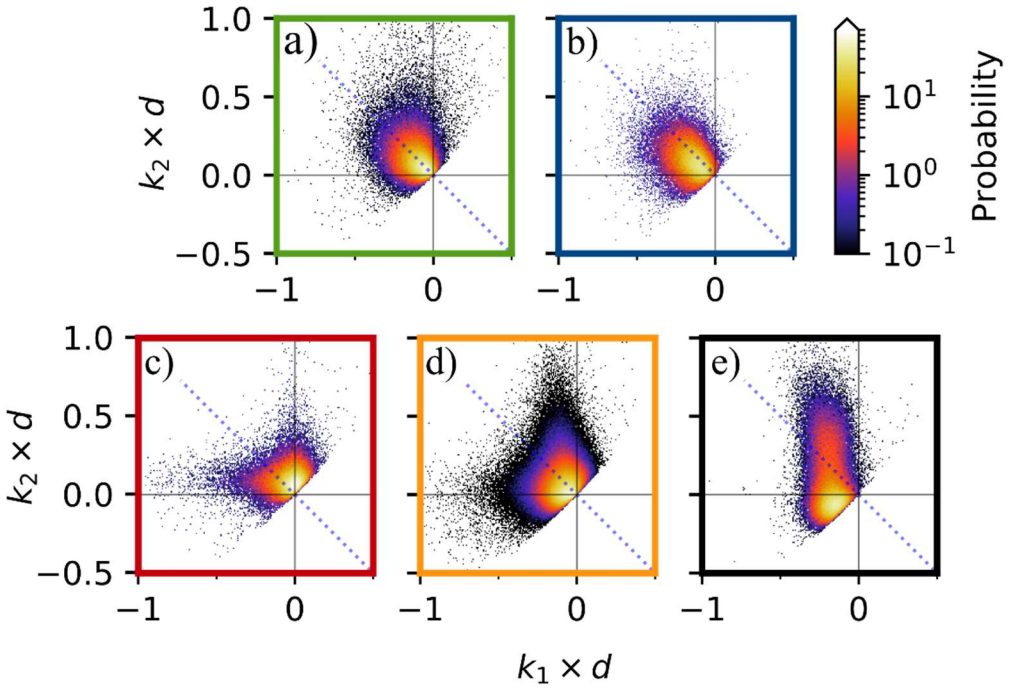

Figure 3-7: ISDs for a) carbon bijel b) polymer bijel c) porous metal d) polyHIPE, and e) inverse opal. The blue dotted line shows k_2=-k_1.

Table 3.2 Curvature Statistics calculated from MicroCT scans of porous media

	Carbon Bijel		**Polymer Bijel**		**Porous Metal**		**PolyHIPE**		**Inverse Opal**	
	Mean ($\times 10^4$)	**Gauss** ($\times 10^{-2}$)	**Mean** ($\times 10^4$)	**Gauss** ($\times 10^{-2}$)	**Mean** ($\times 10^4$)	**Gauss** ($\times 10^{-2}$)	**Mean** ($\times 10^4$)	**Gauss** ($\times 10^{-2}$)	**Mean** ($\times 10^4$)	**Gauss** ($\times 10^{-2}$)
Mean (μm)	-2.94	-4.71	-25.0	-3.12	29.7	-0.51	-17.9	-0.89	-43.4	1.16
Median (μm)	-3.10	-2.56	-23.8	-2.63	30.1	-0.29	-18.1	-0.47	-45.8	1.39
Mode (μm)	-5.46	-0.01	-27.4	-0.87	27.6	-0.04	-12.6	0.00	-48.6	1.15
Standard Deviation	46.9	6.17	33.5	2.95	38.9	1.95	42.3	2.26	26.6	3.96

The ISDs generated by the porous metal and polyHIPE are shaped away from the line $k_2 = -k_1$, such that principal curvatures are infrequently of the same magnitude and local values of mean curvature are consequently non-zero. Projections of the Gaussian curvature onto the reconstructed interface are shown in Figure 3-8 as blue (negative) and red (positive) colors, and suggest that the fundamental mechanism for this mismatch is contact points between elementary shapes (e.g. spherical pockets), where one of the principal curvatures is inverted, resulting in sharp curvature in one of the principal directions. This presents as intensely blue colorizations in these areas and gray or slightly red values in other regions. This effect is also observable in the inverse opal where the densest clustering of points is in the lower left quadrant of the ISD, corresponding to a negative k_1 and k_2. This cluster results from the surfaces generated by the elementary shapes (spheres) in the original crystalline template. At the contact points where the glass particles had sintered together, one of these curvatures has inverted to be strongly positive, appearing in the ISD as points clustered in the upper left quadrant of the graph. The inversion points in all of these structures create regions of negative Gaussian curvature, but the magnitude mismatch between k_1 and k_2 is much more extreme than in a bijel-derived sample, as shown in Figure 3-7.

For intermediate stages of spinodal decomposition, previously published analysis on the curvature suggests hallmarks similar to the known minimal surface gyroid.[67] It should be noted that a minimal surface in this sense refers to its mathematical description, in which the mean curvature is equal to zero at all points, not a thermodynamic minimization of interfacial area per volume. For a rigorous discussion on minimal surfaces, the reader is referred to published reviews.[113,114] The bijel-derived structures cluster strongest around the $k_2 = -k_1$

line in the ISD indicating these are the closest approximation of a mathematically defined minimal surface for the materials evaluated in this study.

In addition to marking approximations of a minimal surface, curvature has recently been identified as an important feature of biomaterials, affecting cell migration and differentiation.[115,116] The curvature distribution of internal surfaces is also expected to significantly influence the mechanical properties of a porous or composite material.[44,117] It is well understood that sharp cracks and porosity act as strength-limiting defects, especially in brittle materials.[118] Recently, simulations and experiments on shapes with dominantly negative Gaussian curvature have shown an efficient distribution of stresses and an approach toward full theoretical strength,[119] while curvature in general can be used to steer or even arrest crack propagation.[120] Therefore, the observed predominance of negative Gaussian curvatures is expected to impart unique and desirable mechanical properties to bijel-derived porous materials and composites.

3.4.4. Connectivity

Table 3.3 presents the scaled genus, G_s, and the relevant parameters involved in its calculation, for the materials investigated in this study.

Table 3.3: Connectivity parameters

	Carbon Bijel	Polymer Bijel	Porous Metal	PolyHIPE	Inverse Opal
S_v^{-1} (µm)	6.25	37.3	23.5	10.0	36.9
G_s	0.146	0.162	0.151	0.293	0.199

Materials with microstructures similar to the non-spinodal samples studied here have recently been employed in electrochemical, catalysis, and tissue engineering applications, and have

demonstrated advantages in active material utilization,[68,121] mitigation of degradation mechanisms,[10,15] high power operation,[46,122] and cell infiltration,[123,124] all of which are generally attributed to enhanced phase connectivity.

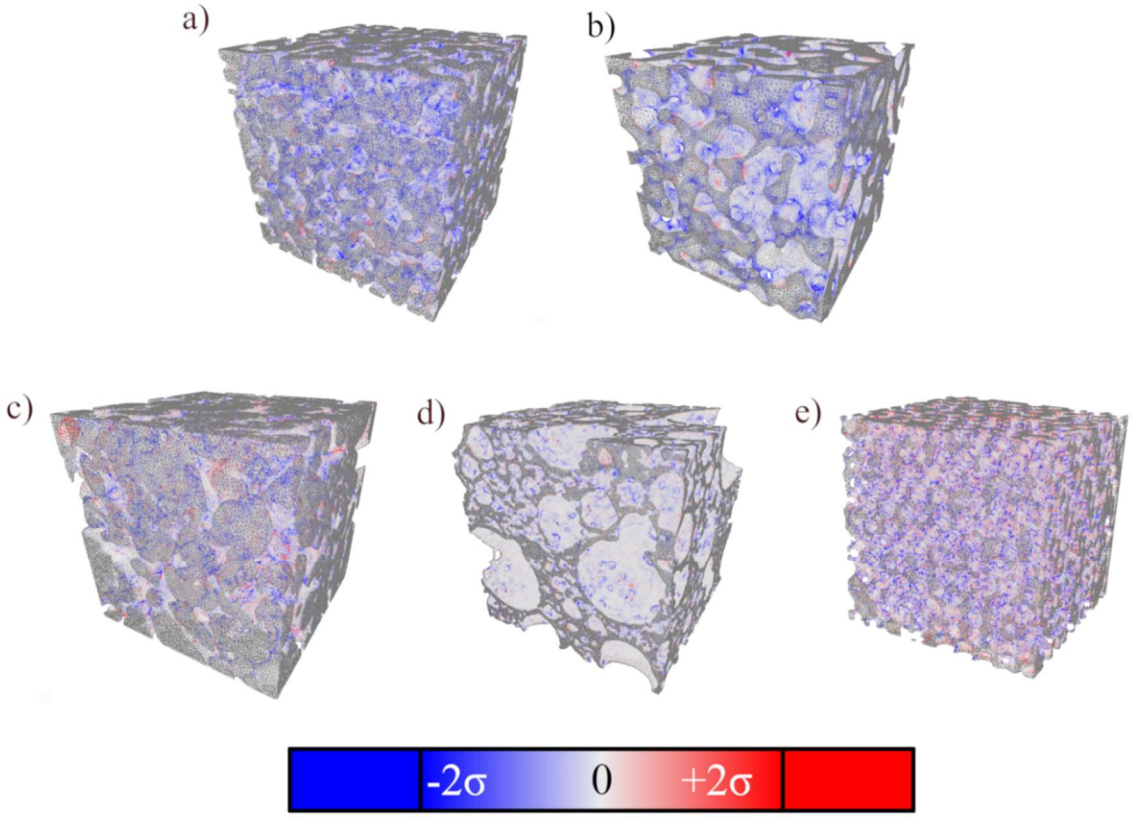

Figure 3-8: Per vertex integrated Gaussian curvatures projected onto the models as blue - red values. The color span ranges from two standard deviations below (blue) to two standard deviations above (red) a Gaussian curvature of zero. Values below and above this range have the maximum blue and red values, respectively. a) carbon bijel b) polymer bijel c) porous metal d) polyHIPE, and e) inverse opal.

Additionally, the mechanical properties of lightweight porous structures are generally related to their solid phase connectivity, as this is a key determinant of stress propagation pathways through the structure.[125] Previous computational studies have reported scaled genus values of $G_s = 0.132$ and $G_s = 0.165$ for spinodal and gyroid structures, respectively.[74,96] Our

measurements are generally in agreement with these reports (G_s = 0.146 and 0.162 for the carbon and polymer bijels, respectively), and notably suggest a similar degree of connectivity (G_s = 0.15 – 0.20) for the non-spinodal samples studied, with the exception of the polyHIPE (G_s = 0.293). In order to scale G_s across materials, a characteristic length scale is estimated by the ratio of area to volume (reported in Table 3.3 as S_v^{-1}).

Therefore, bijel-derived structures enjoy phase connectivity on par with most other classes of porous materials commonly utilized in applications. However, this comes with the critical and unique advantage of uniform pore and solid domain size distributions, which can be highly advantageous for the applications discussed earlier. The less uniform domain sizes in non-spinodal structures can translate to poor quality connections in both the solid and void phases. Narrow solid phase connections, pore phase constrictions and sharp curvatures are expected to compromise the mechanical properties[96,126] or functionality of catalysts and electrochemical devices,[10,15] as well as the species transport or cell migration pathways through the porous material.[111] It should be noted that the characteristic length used in the calculation of G_s, estimated as S_v^{-1}, is insensitive to size heterogeneity and therefore may not fully capture the dependence of phase connectivity on domain size distribution. As such, these two aspects must be considered separately when assessing the morphological advantages of bijel-derived porous materials for applications.

3.4.5. Tortuosity

Plots of L_e *vs.* L for all 50 points tested in each sample for the calculation of $\bar{\tau}$ are shown in Figure 3-9, and the calculated $\bar{\tau}$, ε, m_A, and $\bar{\tau}_{0.5}$ for each material are presented in Table 3.4. None of the measured materials allow perfectly straight pathways through the pore phase, however, the straightest and most predictable lengths are measured in the inverse opal due to the

crystalline and periodic nature of this material. This is reflected in the lowest calculated $\bar{\tau}$ (1.16) and individual L,L_e points clustered close to the $L_e = L$ line ($\tau = 1$) in Figure 3-9e. Pathways through the randomly porous materials (porous metal, Figure 3-9c and polyHIPE, Figure 3-9d) require large and unpredictable deviations from the shortest path, resulting in relatively large $\bar{\tau}$ (1.73 and 1.43, respectively) and points scattered above the $L_e = L$ line. $\bar{\tau}$ in the non-periodic carbon and polymer bijels (Figures 9a and 9b) are intermediate to the ordered and random materials (1.26 and 1.30, respectively), yet the clustering of L,L_e points parallel and close to the $L_e = L$ line for both these materials suggest a more predictable behavior than those in the porous metal and polyHIPE potentially due to the regularity of the microstructure.

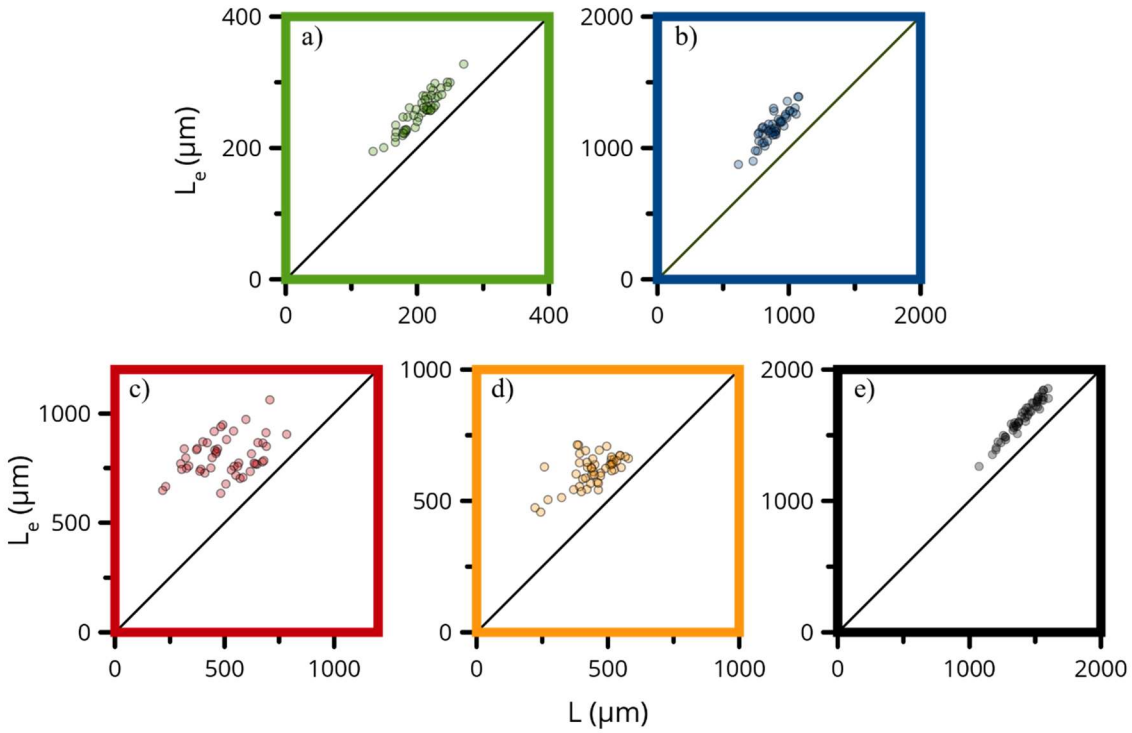

Figure 3-9: Individual L_e vs. L data in a) carbon bijel b) polymer bijel c) porous metal d) polyHIPE and e) inverse opal. L_e=L is plotted as a solid line and represents τ=1

Table 3.4: Tortuosity of tested porous materials and relevant parameters used for scaling

	Carbon Bijel	Polymer Bijel	Porous Metal	PolyHIPE	Inverse Opal
$\bar{\tau}$	1.26	1.30	1.73	1.43	1.16
ε	0.529	0.433	0.406	0.674	0.739
m_A	1.73	1.63	2.22	2.81	1.98
$\bar{\tau}_{0.5}$	1.29	1.24	1.52	1.87	1.40

$\bar{\tau}$ is expected to decrease with increasing ε in randomly porous materials (e.g. porous metal and polyHIPE) as there are fewer solid phase impediments to any path through the structure. The pore geometry-specific Archie's Law exponent, m_A, is highest for the polyHIPE and porous metal, reflecting a greater impact on $\bar{\tau}$ with changing porosity. Of note, the m_A values of the bijel-derived materials are reasonably close, supporting findings that the characteristic bijel microstructural features are preserved after pyrolysis and polymer casting post-processing, and over a range of characteristic domain sizes. Bijel-derived materials have the lowest m_A, indicating a lesser contribution from pore morphology to tortuosity. Further, these materials have the lowest normalized tortuosity, $\bar{\tau}_{0.5}$, translating to the greatest D_e through the structure ($F = D/D_e = \bar{\tau}^2/\varepsilon$). Low tortuosity is advantageous in many applications, particularly fuel cells,[127] chromatography,[128] and tissue engineering scaffolds,[129] which benefit from more robust transport pathways for reactants, analytes and nutrients, respectively.

Tortuosity calculations based on geometric measurements are dependent only on the shape and topology of the medial axis, qualities not directly related to porosity. Decreasing ε for the inverse opal by dilating the solid phase is not expected to impart changes to the medial axis until constrictions between pores are closed, and to this point, $\bar{\tau}$ remains constant. Here we include m_A

and $\bar{\tau}_{0.5}$ for the inverse opal for the sake of comparison (dashed borders in Table 3.4), but it should be noted that these values do not necessarily represent a real scenario.

3.4.6. Self-Similarity

The spatial distribution of branch points (recall Figure 3-2) throughout a structure can be measured by calculating the volume distribution of the corresponding Voronoi cells. The cumulative distribution function for Voronoi cells in each structure is plotted in Figure 10 and is shown to closely fit a modified logistic function:

$$CDF = \frac{-1}{\left(1 + e^{\frac{(\ln(d) - \ln(x))}{\ln(s)}}\right)} + 1$$

where d is the inflection point (i.e the average volume of a Voronoi cell) and s is the steepness term, whose magnitude reflects how uniformly branch points are distributed in space (a large value of s corresponds to a small spread in the Voronoi volume distribution). The independent variable, x, is the cumulative volume of the cells (plotted on the horizontal axis in Figure 3-10).

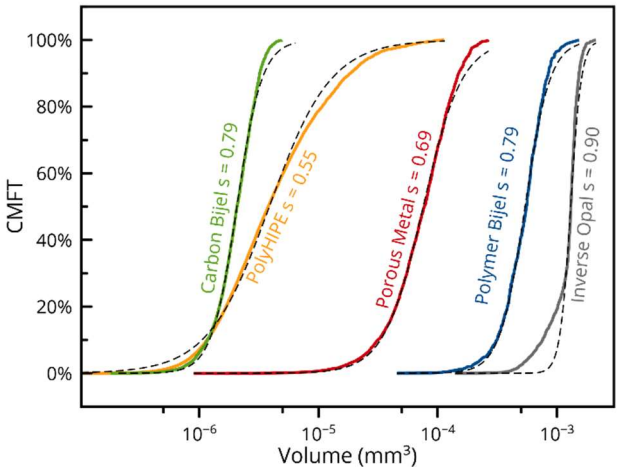

Figure 3-10: Volume distribution of Voronoi cells in selected porous media plotted as Cumulative Mass Finer Than (CMFT) vs. volume. The curves fit a logistic function on a logarithmic scale for the carbon bijel (green), polymer bijel (blue), porous metal (red), polyHIPE (orange), and inverse opal (grey). Dotted lines show fits to the modified logistic function.

The inverse opal structure has the greatest steepness factor of 0.90 in the modified function, indicating the most uniform spatial distribution of branch points. We expect this to be the case as junctions in the medial axis are by nature uniformly distributed in such a periodic structure. The two bijel-derived samples display the next tightest Voronoi volume distributions. Interestingly, the steepness factor matches for both of these samples with a value of 0.79, indicating that, in this unique class of porous materials, self-similarity is maintained across different length scales, and even after pyrolysis processing. The porous metal and polyHIPE structures, derived from more random processes, have broadly distributed Voronoi volumes with steepness factors of s = 0.69 and 0.55, respectively. Therefore, bijel processing provides access to a unique class of porous materials that, without relying on a periodic backbone, enjoy a relatively uniform distribution of medial axis branchpoints within the pore phase.

A broad distribution of Voronoi cell volumes indicates a non-uniform spatial arrangement of medial axis branch points in the structure. Oversized Voronoi cells indicate regions poorly populated by these junctions, while conversely, small Voronoi cells can be attributed to a high local density of branch points. Therefore, we expect the relatively steep distributions for bijel-derived materials seen in Figure 10 to play into advantageous transport properties such high hydraulic permeability in these systems, which will be the topic of a future investigation in our laboratory.

Self-similarity in either the pore or solid phase is important in uniform active material utilization for electrochemical systems. The observed advantages in inverse opal derived electrodes are attributed to enhanced homogeneity and connectivity working together to uniformly expose active elements.[46] We expect the previously identified qualities in bijel-derived materials (i.e. curvature, domain size distribution, connectivity, tortuosity) to work synergistically with the self-similarity in complex systems using this new morphology.[23]

3.5. Conclusions

Using 3D reconstructions from μCT data, bijel-derived materials were demonstrated to possess a unique combination of microstructural features. These include dominantly negative Gaussian surface curvature, tight distributions of domain size, high connectivity, moderate tortuosity, and structural self-similarity. Furthermore, these morphological features are maintained across a range of length scales typical for bijel processing. The full microstructural analysis demonstrated how the bijel, formed in a dynamically self-similar manner, can be processed into porous materials possessing the distinctive morphological attributes of the parent structure for future development of porous materials with enhanced transport and mechanical properties. These inherent advantages of near-minimal surfaces are applicable across a large range of disciplines, and bijel processing is currently being explored as a scalable engineering route for highly permeable, mechanically robust materials for energy systems, catalysis, filtration, and biomedical devices. This self-assembly technique has inherent advantages in scalability over conventional routes toward gyroid-like minimal surfaces that rely on deliberate material design, adding cost and time to the fabrication process.

4. On Deactivating the Solid Phase of an Electrode

4.1. Abstract

Secondary zinc/zinc oxide electrodes have traditionally suffered from electrochemically-driven material redistribution during recharge, leading to cell failure through short circuits or compromised transport pathways. Maintaining a homogeneous current density by increasing connectivity in an electrode has been shown to limit material redistribution and delay capacity loss during cycling. In this work, microstructures derived from spinodal decomposition enable a more uniform current density within the electrode and mitigate the loss mechanisms associated with material redistribution, due to their unique topological characteristics. 2D simulations show that spinodal structures are able to maintain better connectivity and a more uniform distribution of current densities during one full discharge, than their stochastically-derived analogs. Inspired by these results, zinc electrodes with spinodal-like morphology were generated and their cycling performance compared to powder-derived stochastic analogs, up to a depth of discharge competitive with commercial Li-ion technology. Our synthesis protocol is based on soft matter templating techniques described previously in Chapter 2. While the stochastic electrodes lose their entire capacity in 40 galvanostatic charge-discharge cycles, the spinodal-like structures maintain >90% of their original capacity over the same cycling duty, and show significant improvement in lifetime to approximately 100 cycles. *Ex-situ* SEM observations show that material redistribution is effectively delayed in the spinodally-derived electrodes, which we attribute to more uniform current densities during cycling as motivated by our simulations. Our findings establish a facile strategy based solely on microstructural design, to improve the cyclability of zinc oxide electrodes.

4.2. Introduction

The emerging market for electric vehicles and the demand for higher performance batteries in personal electronics have fueled a need for advanced electrochemical cells with high power and energy densities and motivated scientific research to enable their development. Lithium ion-based technologies dominate these markets; however, the reactivity[3,4] and availability of required materials[5,6] present challenges to their safe processing and pervasive use. Recently, systems using cyclable Zn-based electrodes have attracted interest as a competing technology,[130] offering electrochemical characteristics competitive with Li-based systems, but with advantages of raw material availability, safety,[131] and recyclability.[132] Zn anodes can be paired with nickel, silver or oxygen to create primary cells with high power density[131,133] or high energy density.[132,133] However, enabling rechargeability in this technology has presented a challenge, due primarily to the solubility of the zincate ion – an intermediate reactant during charge cycling:

$$Zn + 4OH^- \leftrightarrow Zn(OH)_4{}^{2-} + 2e^-$$

$$Zn(OH)_4{}^{2-} \leftrightarrow ZnO + H_2O + 2OH^-$$

For systems based on the dissolution and reprecipitation of active material from the electrode surface, a limit in cyclability and capacity is reached as internal conduction pathways change through redistribution of active material, creating non-uniformities, discontinuities for charge conduction, or short-circuits.[134–138] This typically corresponds to an observable evolution to electrode morphology.[11,139,140] Strategies to mitigate material redistribution in Zn systems are frequently in the form of additives to the electrolyte[12,141,142] or electrode material,[143–146] or adsorbed barriers at the interface of the electrode and the electrolyte.[137,138,145,147–

149] As an alternative or complementary strategy, tuning the electrode microstructure to be naturally resistant to “hot spots” (i.e. local regions responsible for a disproportionate amount of current density) has only recently become an active research topic.[10,150,151] For Zn electrodes, the opportunity to perform electrochemistry uniformly over the entire internal surface is highly advantageous and has been shown to mitigate the currently accepted degradation mechanisms.[10,150] In this paper, we investigate a new strategy in the design of Zn-based electrodes, based solely on the design and tailoring of the microstructure, to achieve a more uniform current density along the electrochemically active surfaces, thereby discouraging undesired microstructural evolution during operation and enhancing electrode cyclability.

Bicontinuous interfacially jammed emulsion gels (bijels) are a new class of soft materials based on the arrested spinodal decomposition of two partially miscible fluids.[54,63] Briefly, colloidal particles, tailored to be neutrally-wetting for the separating phases, are adsorbed to the interface of demixing fluids during spinodal decomposition, and become jammed as the coarsening of the structure reduces interfacial area between the fluid phases. This structure can be further stabilized *via* selective polymerization of one phase,[66] and functionalized through a variety of processing techniques, including: electroless deposition,[23] nanocasting,[152] carbonization (pyrolysis), and chemical vapor deposition. Several important features in the topology of bijels – unique to the mode of demixing (spinodal decomposition) that they are formed by – are transferred to their derivatives through templating,[153] most importantly:

a) Phase continuity
b) Uniform and dominantly negative Gaussian curvature of internal interfaces[66]
c) Uniform and tunable domain size and specific interfacial area[23]
d) Accessibility and uniformity of active material at the reaction interface[23]

e) Microstructural self-similarity

We expect that this unique combination of qualities offers electrochemical advantages in transport (relating to items a – c),[154] power delivery (items c and d) and uniform discharge (items a, d and e), as well as enhanced mechanical properties (item b).[44]

In this work, experimental investigation of spinodally-derived ZnO electrodes was first motivated by computer simulations that suggest spinodal topologies are more robust against electrochemical degradation than their stochastically-derived analogs. Uniformity in domain size and interfacial curvature, characteristic of spinodal structures, were shown to work synergistically to reduce highly-preferred sites for redox reactions, or "hot spots", that can drive heterogenous microstructural evolution within the material. With insight from these findings, experiments on Zn-based electrodes were performed to illustrate the advantages of a spinodally-derived microstructure for cycling in this class of electrochemical cells. Zn precursors were precipitated in the solid phase of a bijel-derived polymer scaffold and subsequently sintered to form an electrochemically active ZnO structure templated from the bicontinuous emulsion. These carefully designed bijel-derived electrodes were cycled repeatedly in charge-discharge experiments, and showed higher recoverable capacity upon cycling than stochastic powder-derived analogs. Scanning Electron Microscopy (SEM) observations at various points of cycling showed that microstructural evolution instigated by charge-discharge cycles is delayed in the spinodal, compared to the stochastic, electrode microstructures. Based on the results of our computer simulations and SEM observations, we attribute the enhanced cyclability in our materials to microstructural characteristics inherited from the parent bijel – particularly the uniform domain size and interfacial curvature – leading to a more uniform rate of redox reactions along electrochemically active surfaces during cycling.

4.3. Materials and Methods

Figure 4-1 shows schematic representations of the synthesis processes used in this study to create the bijel-derived and stochastically porous electrodes for electrochemical cycling.

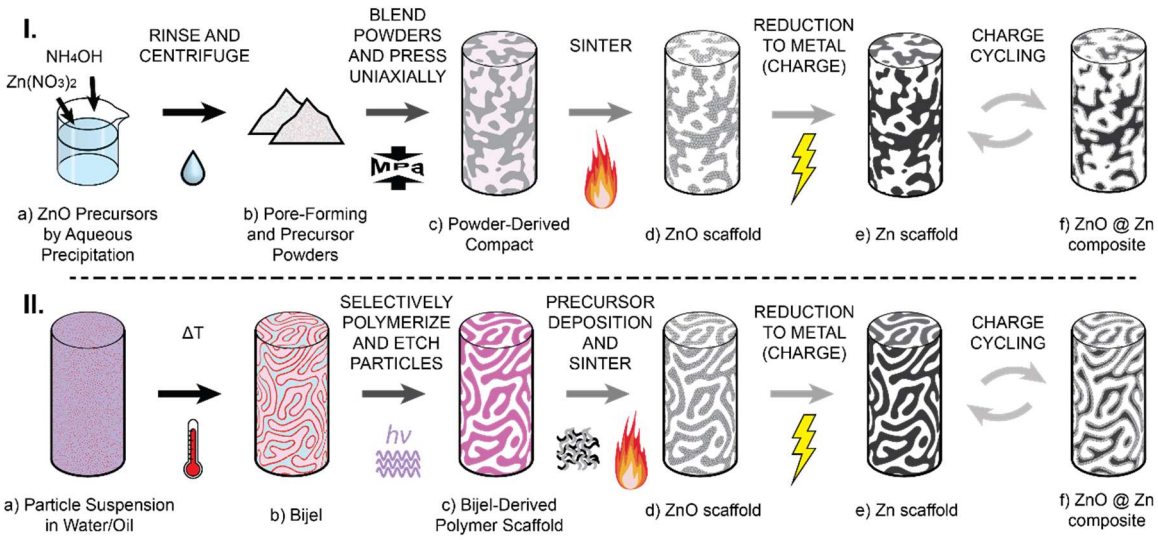

Figure 4-1. Schematic representation of synthesis routes for stochastic (I) and bijel-derived (II) electrodes.

4.3.1. Particle Synthesis

Spherical, sub-micron silica particles were synthesized *via* a modified Stöber process.[79,155] Briefly, 12.5 mg rhodamine B isothiocyanate (RBITC, CAS# 36877-69-7, Sigma-Aldrich, St. Louis MO) was conjugated in 10.0 mL anhydrous ethanol (EtOH, CAS# 64-17-5, Gold Shield Distributors, Hayward CA) with 26.3 µl 3-aminopropyltriethoxysilane (APTES, CAS# 919-30-2, TCI America, Portland OR) for 24 h. Half of this dye solution was added to a solution of 55.0 mL EtOH, 10.0 mL 18.1 M ammonia solution (NH_4OH, CAS# 1336-21-6, Fisher Scientific, Fair Lawn NJ) and 4.18 mL tetraethylorthosilicate (TEOS, CAS# 78-10-4, Sigma-Aldrich, St Louis MO). The silica precursors were allowed to hydrate and oxidize for 24 h before being rinsed with deionized water through five centrifugation/redispersion cycles.

The particles were subsequently dried at 135 °C under vacuum (~25 in Hg) for 28 h to achieve near-neutrally wetting conditions between water (>18 MΩ, Millipore-Sigma, Burlington, MA) and 2-6 lutidine (CAS# 108-48-5 Sigma-Aldrich, St. Louis MO).

4.3.2. Scaffold Synthesis

After drying, silica particles were dispersed in water *via* an ultrasonic horn (Model Sonifier 250, Branson Ultrasonics, Danbury CT) and mixed with 2-6 lutidine such that the volume fractions for silica, water, and 2-6 lutidine were 0.030, 0.669, and 0.301, respectively. Tubular glass cuvettes charged with 0.205 mL of the suspension were heated in a microwave for 15 s at a power of 230 W to induce spinodal decomposition of water-rich and lutidine-rich phases, with the neutrally-wetting silica particles trapped in a monolayer at the interface as shown in Figure 4-1 IIb. The samples were then transferred to a 70 °C oven to maintain temperature above the lower critical solution temperature (LCST) of 34.1 °C. The oven was controlled to the higher 70 °C temperature to resist cooling below the LCST during oligomer addition outside of the oven. Polyethylene glycol diacrylate (PEGDA, CAS# 26570-48-9, Sigma-Aldrich, St. Louis MO) was added to the top of each sample (35 µl) with 1 vol% Darocur 1173 (Ciba Specialty Chemicals, Basel Switzerland) as a photoinitiator, and the oligomer solution allowed to selectively diffuse into the lutidine-rich phase for 4 h before polymerization *via* 30 s ultraviolet radiation (Omnicure Series 1000, 100 W power). After curing, the scaffolds were rinsed with deionized water to remove unreacted oligomers. Silica particles were etched from internal surfaces *via* a 5 h treatment with 6 M hydrofluoric acid (HF, CAS# 7664-39-3, ThermoFisher Scientific, Hampton NH) and the PEGDA scaffolds were left to dry in a convection oven at 70 °C.

4.3.3. Precipitation and Sintering of ZnO Precursors

Precursors to ZnO were precipitated in the solid phase of the porous polymer template by controlled reaction of $Zn(NO_3)_2$ and NH_4OH, similar to the templating approach by Park and Meldrum.[156] Briefly, the dried, etched polymer scaffold was treated with equal volumetric amounts of 4 M aqueous NH_4OH and 8 M nitrate salt solution to selectively precipitate solid Zn precursors in the hydrophilic solid phase of the scaffold. 500 ppm indium and bismuth were included as nitrate salts to suppress hydrogen evolution.[157] A 0.127 mm diameter Pt wire was attached to the scaffold as a current collector before heat treating the samples in air at 1350 °C for 3 h in a box furnace (Model 51314, Lindberg/Blue M Electric, Watertown WI) to burn away the polymer template and densify the ZnO scaffold.

4.3.4. Preparation of Stochastic Electrodes

To provide a structure of similar chemistry and stochastically porous morphology, a precipitated ZnO powder was blended with a pore former and sintered alongside bijel-derived scaffolds. To enable direct comparison of these stochastic electrodes to their bijel-derived counterparts, the pore former was selected from a variety of starch-based organics to create a pore phase with a similar average domain size (observed *via* SEM) to the bijel-templated electrode. Electrode porosities, estimated from density measurements, were also matched between the stochastic and bijel-derived samples by manipulating the relative concentrations of precursor and fugitive pore-former powders in the stochastic specimen formulations. This produced an array of stochastically porous structures, in which the chemistry, average pore size, and porosity were similar between each sample and its bijel-derived counterpart.

4.3.5. Electrochemical Reduction of ZnO to Zn: Charging a Half Cell

The sintered ZnO scaffolds were electrochemically reduced to metal by maintaining a –1.55 V bias (*vs.* Ag/AgCl in 1 M KCl) in 1 M KOH with a Pt wire counter electrode. Potential was applied and current recorded *via* a Keithley 2400 Sourcemeter (Tektronix, Beaverton OR) controlled by a computer and the PyVISA library. Maintaining a negative potential drives the cathodic transformation of ZnO to Zn metal at the working electrode, and anodic evolution of oxygen at the counter electrode. No hydrogen evolution was observed at the working electrode.

4.3.6. Post-Reduction Sintering

To further solidify the conductive backbone, the reduced Zn samples were sintered in ultra-high vacuum ($<10^{-8}$ Torr) at 405 °C, 98.6 % of the melting temperature of Zn. In the absence of a liquid phase, low T_m metals tend not to sinter until very close to the melting temperature.[158] After this initial heat treatment, electrodes were exposed to air and heated to 600 °C for 3 h to further enhance connectivity. This follows the procedure of Parker, *et al.* to create a structure of electrochemically active Zn(O).[10,143,150]

4.3.7. Cell Assembly

A schematic illustration of the components assembled into a cell is shown alongside photographs of a cell during assembly in Figure 4-2.

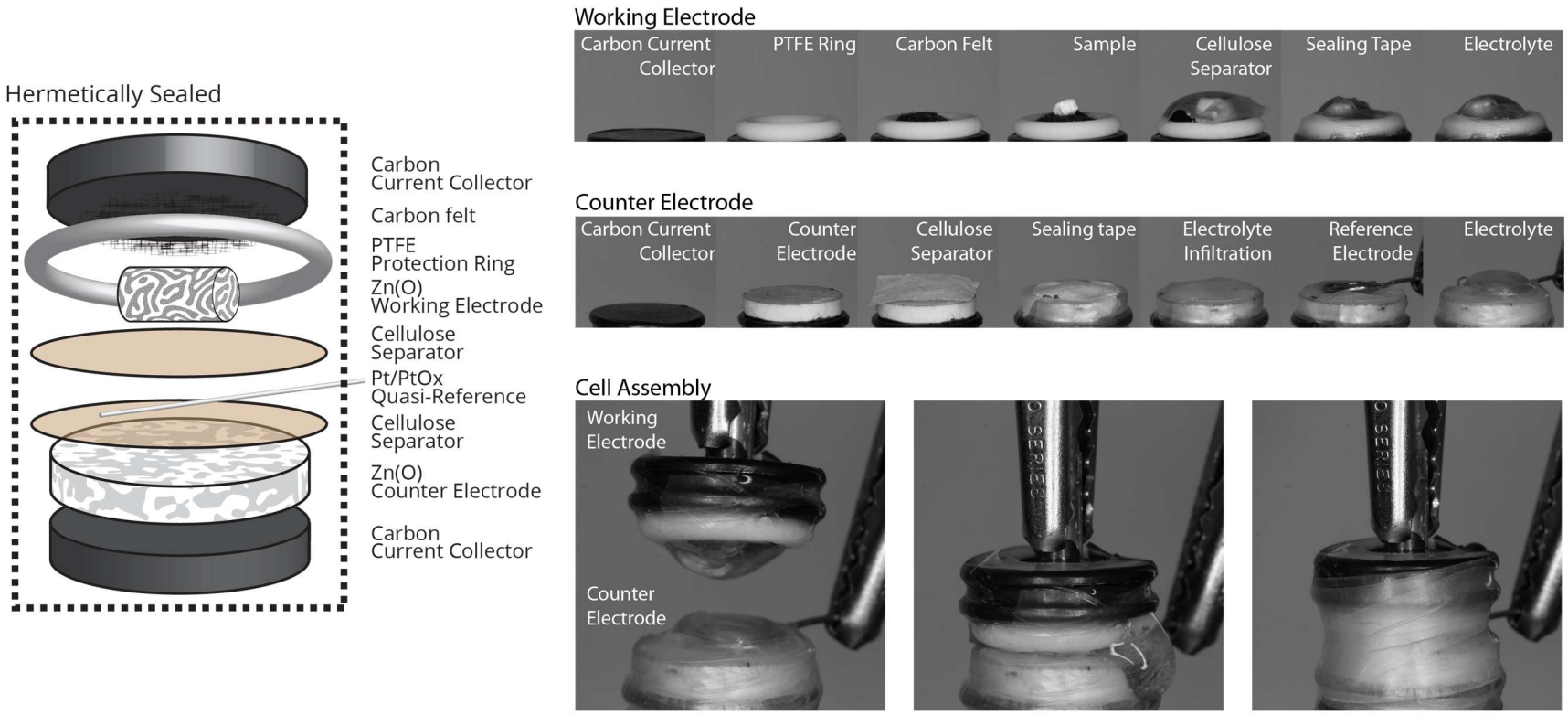

Figure 4-2: (Left) Schematic of cell components used for galvanostatic cycling (not to scale). A bijel-derived sample is illustrated here, but an identical assembly was used for stochastic samples. (Right) Photographs during assembly of a cell.

To minimize experimental contributions from counter electrode degradation, the associated depth of discharge (DOD) was limited to ~1% by using at least 100× more material to create the counter electrode. Prior to assembly, the 0.1 M KOH electrolyte was saturated with soluble Zn to mitigate dissolution of the active material and gelled with polyacrylic acid (40 mg/mL). This viscous electrolyte solution was then vacuum infiltrated (~25 in Hg) into both the working and counter electrodes. Axial pressure was applied through dense current collectors at the ends to maintain electrical contact with the zinc. To prevent crushing the experimental sample during the assembly and sample testing procedures, the working electrode was packed in carbon felt and protected inside of a 1.85 mm thick (poly)tetrafluoroethylene ring. The electrodes were separated by cellulose filters to prevent electrical contact, and the entire cell hermetically sealed after assembly to limit electrolyte evaporation.

4.3.8. Characterization

4.3.8.1. Galvanostatic Charge-Discharge Cycling

The experimental Zn samples were electrochemically cycled in the cell described above. Potential during cycling was measured against a Pt/PtO_x quasireference electrode (QRE). The working electrode was initially charged potentiostatically to –1.30 V *vs.* the QRE, corresponding to metallic Zn. A potentiostatic charge minimizes overpotential by gradually reducing the current as the material is converted. When the current was reduced below 1 mA/g ZnO (roughly equivalent to a C/500 charge rate, i.e. 500 hours for 100% charge or discharge), the charging current was stopped and the full capacity of the electrode measured as $\int I\,dt$. The working electrode was subsequently cycled galvanostatically at a C/5 rate between potential limits of –1.30 V and –0.01 V *vs.* the Pt QRE, until the recoverable capacity dropped below 10% of its

value in the first cycle. Coulombic efficiency was calculated as the ratio of discharge capacity *vs.* the charge capacity.

4.3.8.2. Scanning Electron Microscopy (SEM)

Unless otherwise noted, all electron microscopy was performed on a FEI Magellan SEM equipped with a field emission gun electron source. The ZnO samples required no conductive coating and were attached to aluminum sample stubs with carbon tape. Images included herein were acquired as secondary electron (SE) images using the equipped Everhart-Thornley SE detector, with 18-25 kV accelerating potential.

4.3.8.3. X-Ray Diffraction (XRD)

Uncycled, sintered ZnO electrodes (step d in Figure 4-1) were crushed *via* mortar and pestle, dispersed in isopropanol alcohol, and applied as a paste in a thin layer onto a silicon zero-background holder. XRD measurements were performed over the range 10-100 °2θ with a Rigaku Smartlab diffractometer equipped with Cu Kα radiation to confirm the phase(s) present.

4.3.9. Simulations

Square projections of spinodal and stochastic microstructures were generated for discharge simulations and each divided into 1024 × 1024 pixels for analysis. The spinodal projection is a solution to the Cahn-Hilliard equation, a partial differential equation approximating spinodal decomposition. [57]

The non-spinodal projection was generated stochastically with a noise filter and threshold settings to create elements of random size and topology as a representation of powder-derived assemblies and contrast the uniformity and connectivity of the spinodal structure. The fraction of active pixels in each structure was set to 0.5 and scaled such that characteristic feature size

(measured as active material area/interfacial length) was equal between the two structures. This enabled an initial assessment of how the architecture of the solid phase affects the discharge dynamics and active material topology in these systems.

A demonstration of the discharge algorithm is shown in Figure 4-4 and Figure 4-3.

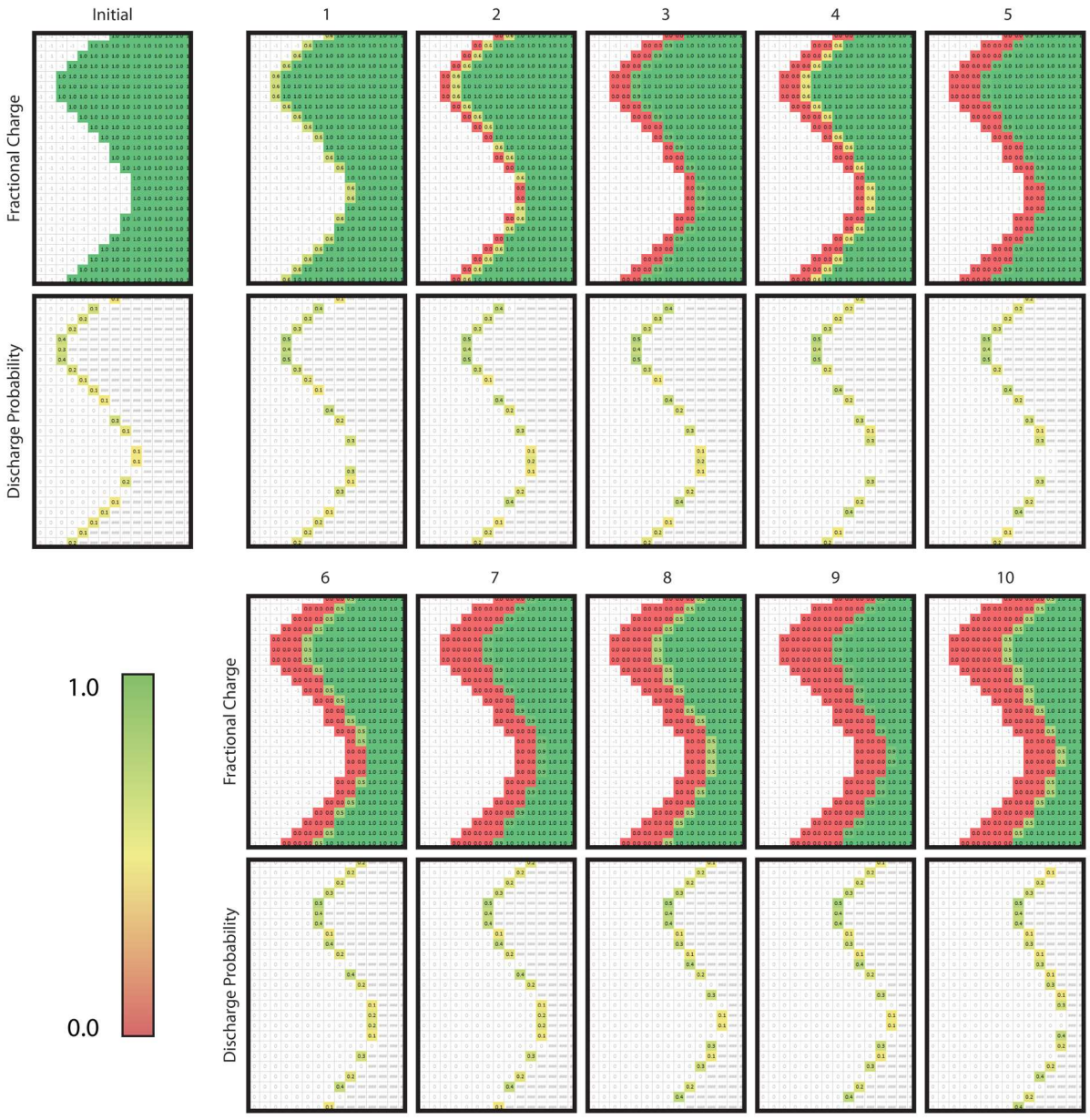

Figure 4-3. Fractional charge of pixels in a simulation (top) showing increased probability of discharge on positively curved surfaces (bottom). The first ten time steps are shown.

As illustrated in Figure 4-3, each active pixel in the simulation was initially assigned a fractional charge of one, which decayed to zero as the electrode was discharged (top panels in Figure 4-3). Each time step in the simulation discharged 1% of the initial capacity, analogous to a galvanostatic experiment. To convert between charged and discharged states, material in an electrode requires electrical contact with the current collector and exposure to the pore phase, which will move reactants and products to and from the reaction sites. In these simulations, the discharge product is considered permeable to reactants. Electrical and chemical conductivity in 2D were maintained throughout the entire structure. Consequently, the probability of a pixel discharging was calculated only from the charge state of its neighbors and its relative exposure to the pore phase. To evaluate this exposure, a blur filter was applied across the simulation and the relative intensity of each pixel used as an indicator. For example, a pixel with a fractional charge of one is unlikely to change state if its neighbors are also fully charged. Conversely, a pixel with neighbors in the pore phase (effectively zero charge) will be blurred to a lower value. Small value pixels in the blurred array were assessed as more reactive and discharged by a higher probability than pixels with larger values (bottom panels in Figure 4-3).

To identify material degradation during simulated discharge, continuous regions of charged material (groups of connected pixels with fractional charge of one) were identified at each time step to compare the active phase topologies between the two structures. Topological events such as disconnects and fully discharged elements were quantified by locating these active bodies as

described below, and monitoring their number and shapes through subsequent frames, as illustrated in Figure 4-4

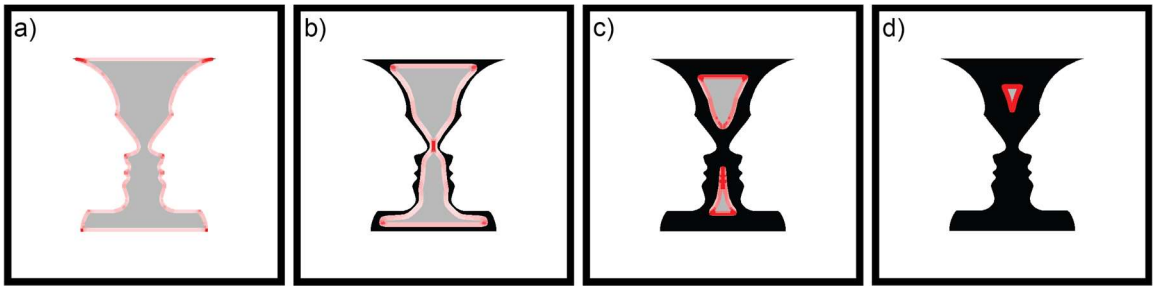

Figure 4-4: Discharge simulations on a Rubin vase at (a) 1%, (b) 40%, (c) 80%, and (d) 95% DOD. A disconnect at the vase nose is demonstrated between panels (b) and (c), and a destroyed body is demonstrated in the bottom half of the vase between panels (c) and (d). Points at sharp features (e.g. base of vase) will experience higher current density (red contour).

Identifying two separate active bodies in the footprint of what was previously only one indicates a disconnection. Conversely, no active bodies in a previously active region suggests complete discharge of one body. To calculate the local rate of material conversion (i.e. the specific current), the interfacial speed between charged and discharged material was calculated as the maximum gradient vector from its components in the x and y directions, $\frac{\partial x}{\partial t}$ and $\frac{\partial y}{\partial t}$. Fast-moving interfaces indicate the material near this interface is transforming quickly and suggest a high local rate of charge transport across the boundary, i.e. a large current density. When calculated in this way, heterogeneities in the specific current, a known driving force for material redistribution, can be quantified.

4.4. Results and Discussion

4.4.1. Simulations

Figure 4-5 shows simulation snapshots at 20, 45 and 80% DOD for the spinodal and the stochastic electrodes, with active material presented in either gray (charged) or black

(discharged, passivation layer). White pixels represent the electrolyte, which is responsible for transporting chemical precursors to reaction sites. The red contour pixels between charged and discharged material indicate interfacial speed in shades of red, with more intense red colors indicating faster-moving boundaries. Examples of disconnects, destroyed bodies, and locally shallow depths of discharge are highlighted by pink, yellow, and green arrows, respectively. The results of Figure 4-5 provide an overall visual basis for the various topological and electrochemical changes that are subsequently analyzed and quantitatively discussed in Figure 4-6. Throughout the rest of this dissertation, I will use color coding consistent with the frames in Figure 4-5, where the results of bijel-derived (spinodal) and stochastic samples are represented in blue and red (symbols or frames), respectively.

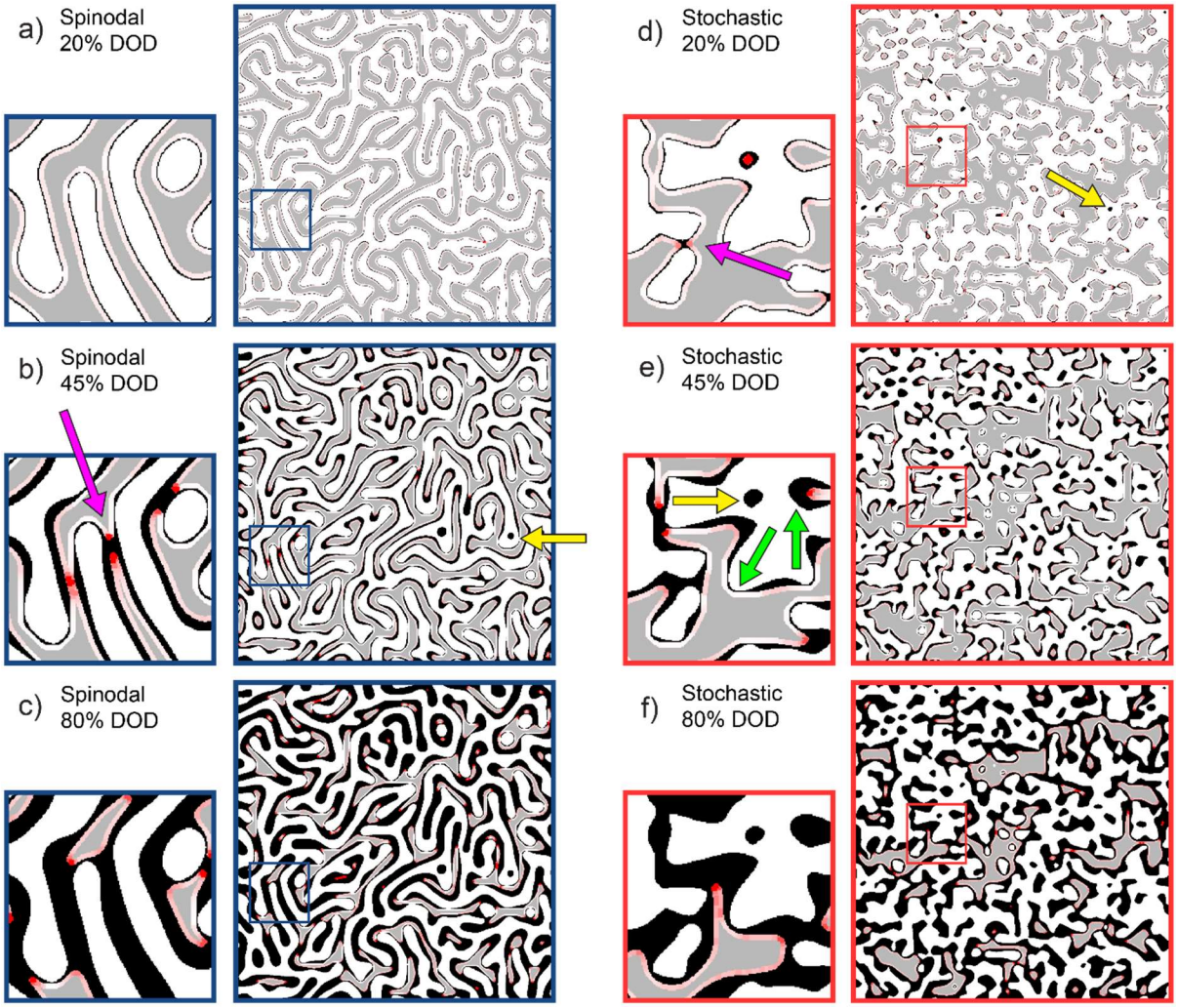

Figure 4-5. (top to bottom) Snapshots in the simulation for 20%, 45%, and 80% DOD, for the spinodal-like (panels a-c) and the stochastic (panels d-f) structures. Higher magnifications of both structures are also presented. The pink, yellow, and green arrows show examples of disconnects, destroyed bodies, or regions with vastly dissimilar local depths of discharge, respectively.

To transition between oxidation states, the material requires both charge, conducted through the solid phase, and reactants, supplied by the electrolyte.[159] As expected, material on the electrode surface is seen in Figure 4-5 to have transformed before the interior elements. In general, growth of the passivation layer began at the solid-electrolyte interface and moved toward the interior, eventually converging and interrupting continuity of the core as a disconnect, or destroying an active body by complete discharge. Qualitatively, these topological events were

observable relatively early in the stochastic microstructure (Figure 4-5, panel d), while the spinodal sample resisted such changes until a larger DOD was reached (Figure 4-5, panel b). Also, close inspection of Figure 4-5 suggests that: 1) variability in the local DOD, as indicated by green arrows in Figure 4-5 panel e, can be caused by variations in the curvature and specific interfacial length of the associated solid features, leading to non-uniform active material utilization. Further, the DOD at which a disconnect occurs depended on the same morphological characteristics (for example, the earliest disconnect in Figure 4-5 is observed at a narrow neck in the stochastic structure); and 2) when a disconnect forms, the oxidation interface moved rapidly away from it as active material continued to be converted under galvanostatic conditions (see the intense red contour colors at the points of disconnect, which are marked by pink arrows in Figure 4-5). These regions are identified as "hot spots" by their fast-moving interfaces, and must be compensated for elsewhere in the structure by regions with locally low current densities. These qualities are characteristic of uneven utilization of active material, and the snapshots presented in Figure 4-5 demonstrate how the non-uniform domain size distribution in a stochastic structure made it more prone to such nonidealities. Our findings in Figure 4-5 are in agreement with previous simulated and experimental observations, in which current density was shown to depend upon the relative exposure an electrode surface has to the electrolyte.[139] In addition, recent Finite Element Analysis (FEA) simulations of current density on electrode interfaces show that even small perturbations to a smooth surface encourage dendritic growth by establishing a non-uniform diffusion front and preferred deposition sites protruding into the electrolyte bulk.[134,139,160,161]

To better understand the topological and morphological changes that occur during discharge, and their impact on local current densities within the electrode, quantitative measurements of

active material connectivity and interfacial speed were extracted from the simulations, and are reported in Figure 4-6. Panels a and b quantify the changes in topology and interfacial speed throughout the simulation, respectively, while panel c shows the spatial distribution of current within each electrode.

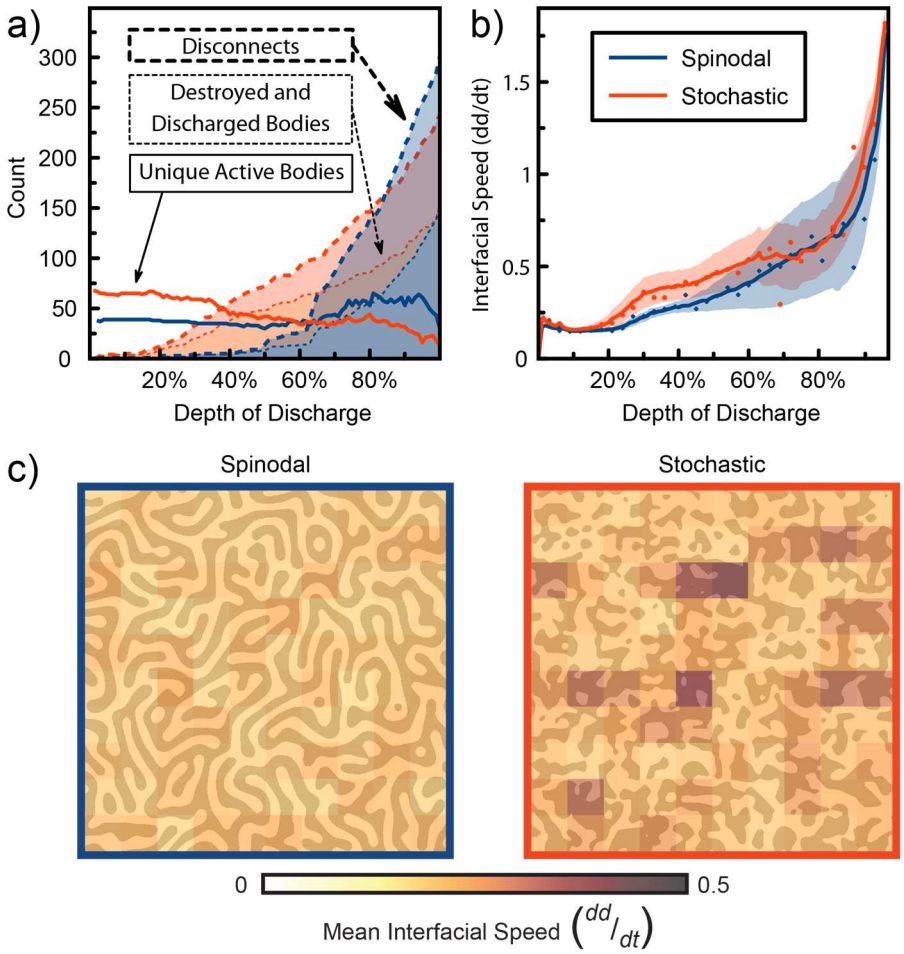

Figure 4-6. (a) Active bodies in a simulation (solid line) and events marking material degradation (shaded/dashed). Material degradation is divided into destroyed bodies (bottom) and disconnects (top) in the stacked line plot. (b) Mean interfacial speed with standard deviation vs. DOD. Markers represent average values at each time step and the solid lines are ten-point moving averages. A confidence envelope shows standard deviation from the mean. (c) Colorized grid overlay of time-averaged interfacial speeds. The spinodal structure (left) distributes current better than the stochastic structure (right), which features lasting hot spots.

Key topological measures reported in Figure 4-6a include unique active bodies shown as a solid line, and material degradation as a stacked line plot (shaded area) comprising destroyed bodies on the bottom and disconnected elements on the top. Both degradation measures increased monotonically after the onset of topological change, which was immediate in the stochastic structure, but largely delayed until about 45% DOD in the spinodal structure. From Figure 4-5, this is when the interface began to pinch the narrowest points in the microstructure and hot spots were qualitatively observable. During late-stage discharge, the topologies of both structures had degraded to nearly the same state (the stacked plots intersect each other at about 85% DOD).

The mean interfacial speed for each structure up to 100% DOD is reported in Figure 4-6b. Here, the solid markers represent the measured mean interfacial speeds at different points in the simulation, and the solid lines represent a ten-point moving average of the same quantity. Variability in the measured speeds is shown as a shaded confidence envelope generated by the standard deviation of all measurements at each time step. Initially, the average interfacial speed was slow, suggesting a low current density, but as material is converted, the perimeter of active bodies in the system is decreased resulting in an increased current density to maintain galvanostatic conditions, and consequently, faster moving interfaces. The perimeter of active material in the simulation is quantified in Figure 4-7.

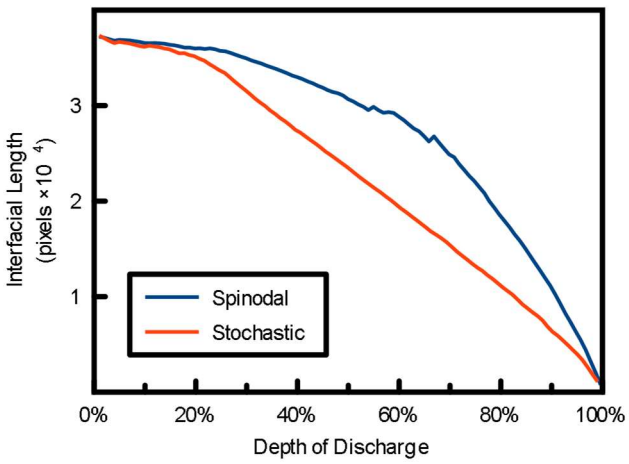

Figure 4-7. Interfacial length of both electrodes during the discharge simulation. The spinodal structure maintains a larger interfacial length to a greater depth of discharge than the stochastic structure.

Interestingly, the increased scatter in these measurements correlates closely with the degradation events tracked in Figure 4-6a, suggesting fast-moving interfaces were inspired by these topological events. The variations in interfacial speed seen in Figure 3a also agree with our qualitative observations in Figure 4-5, where the interfacial speed appeared to be more uniform in the spinodal structure (panel a) than its stochastic counterpart (panel d) up to about 45% DOD. In addition, Figure 4-5 can also help explain the notable increase in the variance seen in Figure 4-6b after 45% DOD: because of the nearly uniform domain size in the spinodal structure, upon formation of a disconnect, the oxidation interface will have to advance very rapidly along the filament core to maintain galvanostatic conditions (for example, see the intense red colors at the point of disconnect in Figure 4-5 panel b), while regions without such topological changes continued to discharge with a much slower-advancing interface. By contrast, the heterogeneous distributions of domain size and interfacial curvature in the stochastic structure, which led to topological changes at a shallow DOD as seen in Figure 4-5, panel e, also contributed to an

earlier onset of non-uniform current densities (increased variance in interfacial speed) as seen in Figure 4-6b.

To provide information on the spatial distribution of hot spots within the electrode, the simulation frame is divided into a 10x10 grid, and the time-averaged interfacial speed in each sector is presented in Figure 4-6c as a color overlay. Dark purple tiles in Figure 4-6c represent regions that were discharged quickly by fast-moving interfaces throughout the experiment. In the spinodal electrode, the interfacial speed was relatively consistent throughout the structure, as indicated by the uniformity of the color overlay. Conversely, in the stochastic structure, the microstructural (size and curvature) heterogeneity of the active material resulted in lasting hot spots, as identified by the dark purple tiles in Figure 4-6c. As discussed earlier, an electrode with lasting hot spots is envisioned to experience more aggressive material redistribution during cycling, leading to earlier failure.

Collectively, the results of Figure 4-6 suggest that the uniformity of domain size and interfacial curvature in a spinodal structure can delay the onset of topological changes during discharge, and also lead to a more homogeneous distribution of current within the electrode, a known strategy to mitigate material redistribution and deactivation. In addition to the microstructural and topological issues analyzed in our simulations, non-uniform currents can also be driven by concentration polarization and increased ion transport to sites protruding into the bulk of the electrolyte.[134,149,161] The regions surrounding these extended features experience a steeper profile in reactant concentration, and diffusion-limited kinetics.[139,161,162] The non-uniformities in current density caused by these issues are known to contribute to dendritic growth and redistribution of active material, especially in Zn-air batteries.[139,161,163] It has been shown previously, that pulsed electrodeposition is effective

in minimizing dendritic growth by allowing the concentration profile to recover and replenishing precursors close to the electrode surface.[139,164] However, this strategy is impractical to meet the demands of modern secondary batteries.

Our simulations provide a rudimentary assessment of how discharge kinetics and current density distribution may be affected by the electrode's topological characteristics, but many important processes that mediate the overall performance of these systems are not modeled here. Notwithstanding this limitation, and given the importance of maintaining a uniform current density distribution in Zn-based electrodes during charge and discharge, our simulations motivate an experimental investigation of how cyclability of ZnO electrodes may be enhanced through microstructural design. Particularly, we aim to assess the efficacy of the synthesis platform illustrated in Figure 4-1 for creating porous ZnO electrodes with enhanced topology, thereby improving their electrochemical performance and cyclability in service.

4.4.2. Synthesis

In order to confirm successful synthesis of porous ZnO electrodes, XRD and SEM analysis was performed on the final, oxidized specimens illustrated in Figure 4-1 step d of both routes. Figure 4-8 shows the XRD patterns obtained from representative samples. Based on the observed diffraction patterns, the oxidized electrodes were confirmed to be single-phase ZnO in the hexagonal wurtzite structure. Figure 4-9 shows SEM micrographs of representative bijel-derived and stochastic structures at three different magnifications to examine both the overall pore phase morphology and surface texture. The important features expected to contribute to device operation are connectivity, curvature, and domain size, and it is qualitatively discernable in the SEM images (Figure 4-9, comparing panels a and e) that the bijel-derived electrode has greater

uniformity across these metrics. The average domain size for the bijel-derived sample, estimated by the line intercept method, was 10.0 ± 1.77 μm, illustrated in Figure 4-10.

The dry-pressed analog shows a non-uniform and stochastic arrangement of pores with a broad size distribution (11.8 ± 2.70 μm). The sub-micron texture was observed in Figure 4-9 panels d and h to be similar in both electrodes, as expected from their analogous synthesis protocols.

Based on these observations, we expect the main differences in the electrochemical behavior of the two electrodes to be attributable to disparities in their microstructural uniformity and connectivity, and not the porosity, average pore size, or potential faceting of the surfaces of the solid phase itself.

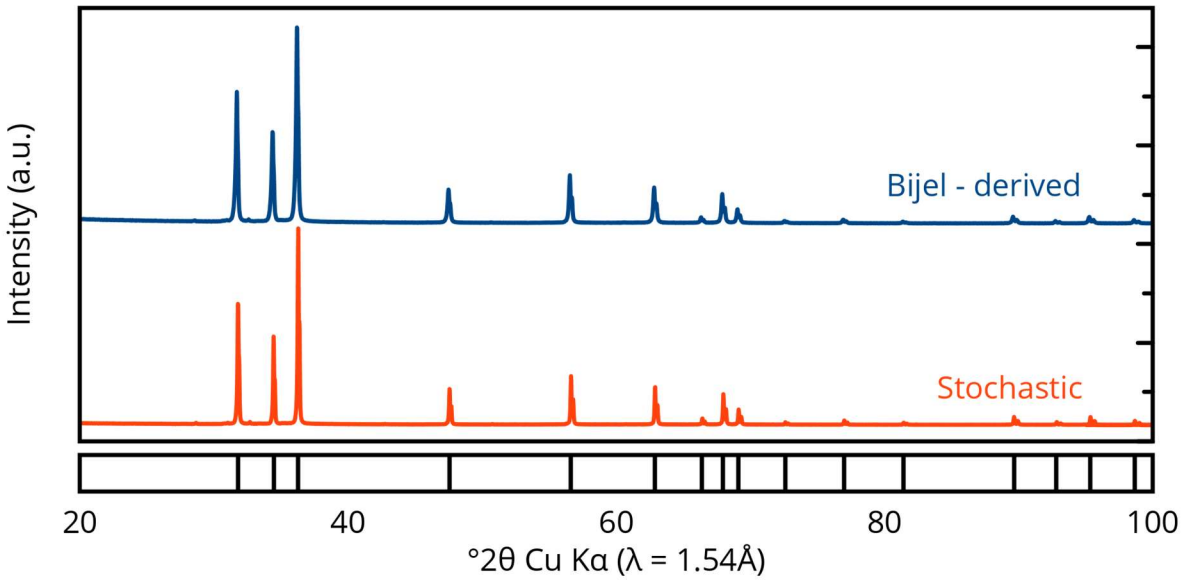

Figure 4-8. XRD patterns between 20 and 100 °2θ, collected after template removal. All peaks are identified as reflections from hexagonal ZnO.

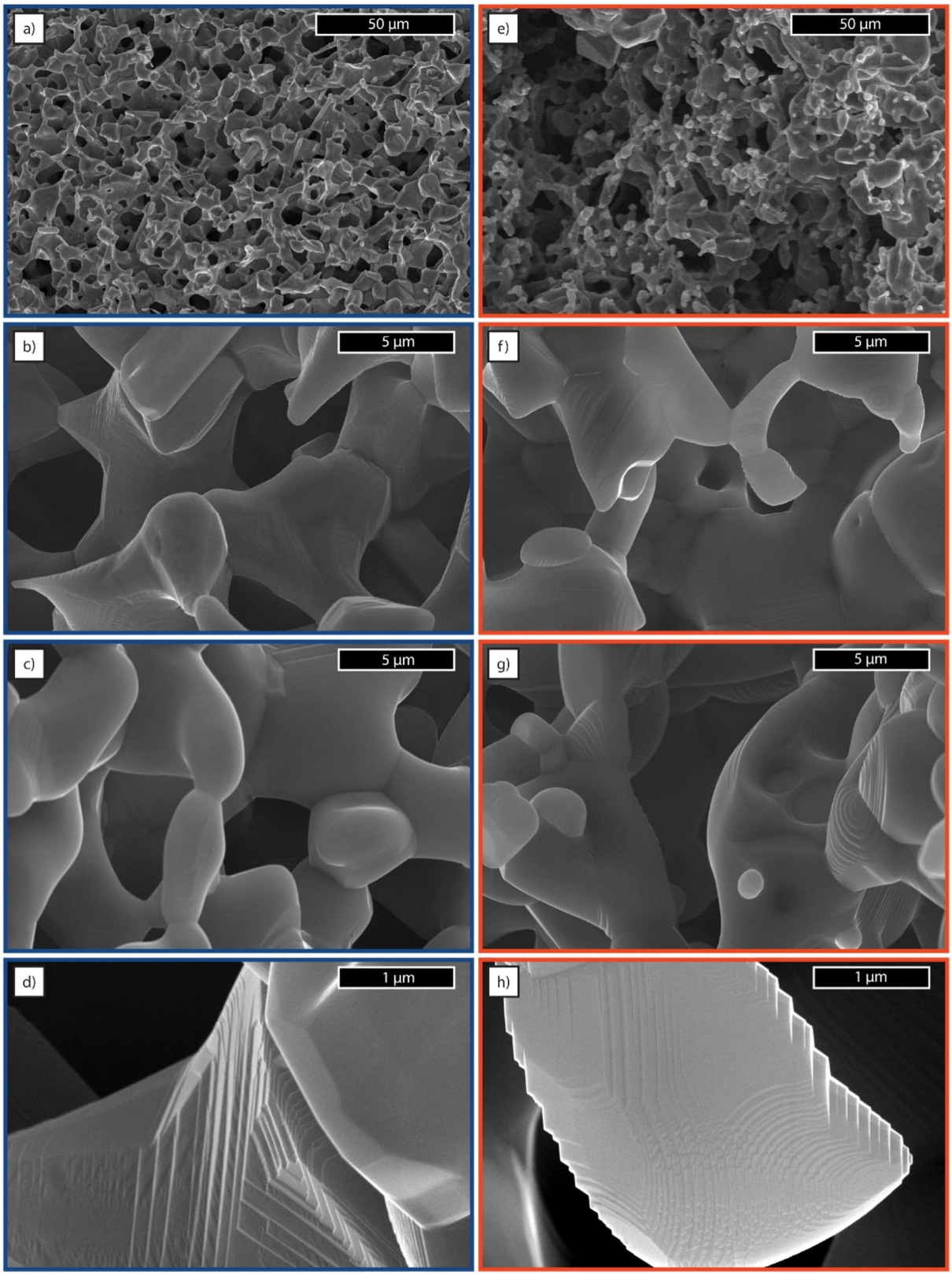

Figure 4-9: Photomicrographs of bijel-derived (a-d) and stochastic (e-h) ZnO scaffolds at various magnifications, showing microstructure and texture. The microstructural difference is apparent in the macro image, while sub-micron faceting between the two materials is similar.

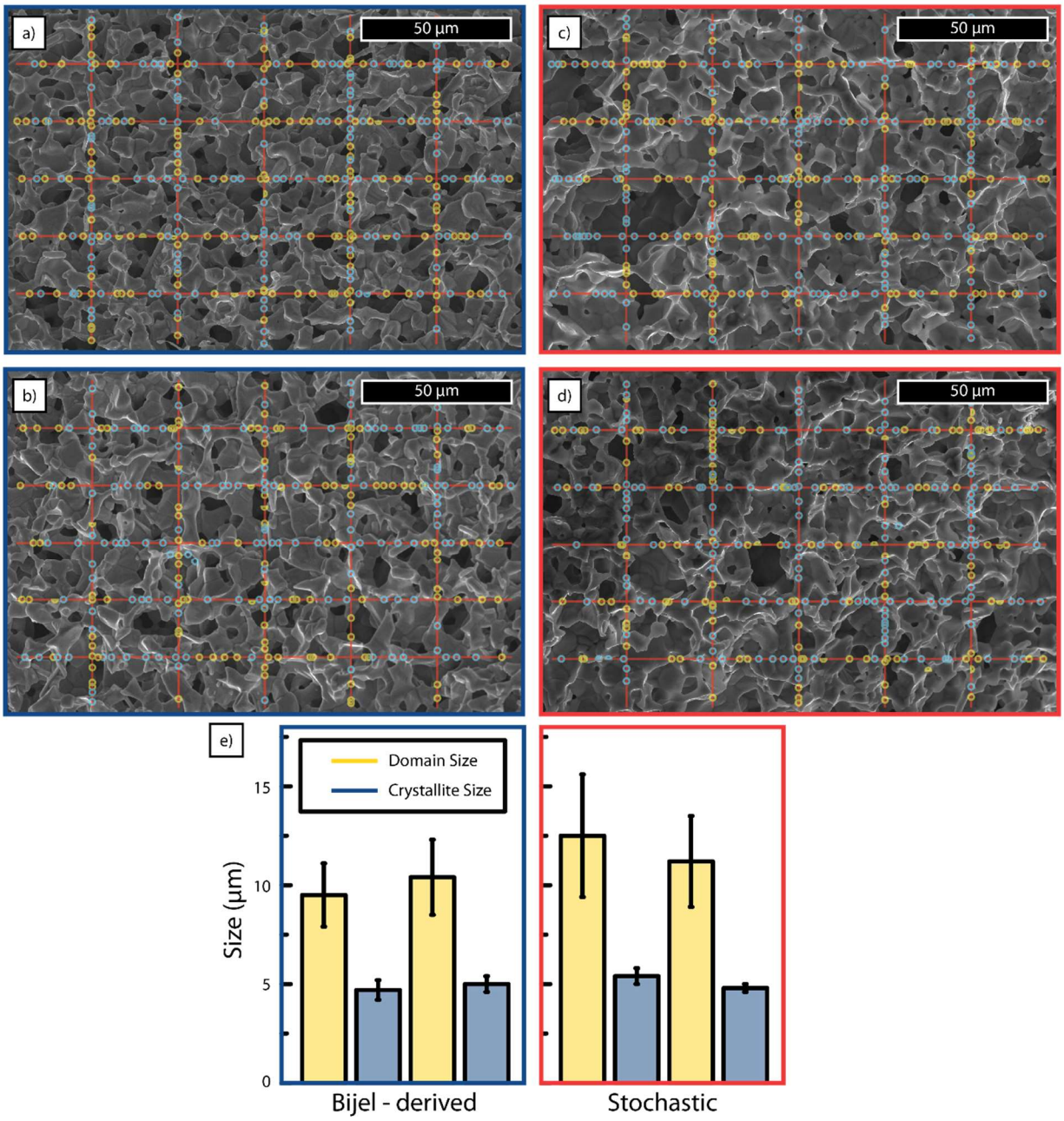

Figure 4-10. Microstructural analysis via line intercept on bijel-derived (left) and stochastic (right) electrodes.

4.4.3. Electrochemistry

After synthesis, the oxidized electrodes were electrochemically reduced (charged) to Zn, as schematically shown in Figure 4-1 between steps d and e and described in Materials and

Methods. Figure 4-11 shows the current applied to representative bijel-derived and stochastic ZnO electrodes during this conversion. The bijel-derived structure experienced a peak specific current >5× higher in magnitude than its stochastic analog, resulting in a much faster and nearly complete conversion to the metallic state (815 mA-h / g Zn metal, 99.4% utilization). The stochastic electrode did not fully convert to metal (704 mA-h / g Zn metal, 85.9% utilization). Decay of the current to zero suggests that parasitic hydrogen evolution did not contribute to the signal during this process (note we also did not observe any bubble formation). The overpotential required to evolve hydrogen on a zinc electrode is high,51 especially in the presence of indium and bismuth41 (these elements were included as salts in the precursor solution as mentioned earlier, and it is plausible to expect them to be present in trace quantities within the scaffold).[165] While it is feasible and even expected to reach these potentials locally during a galvanostatic reduction (as in the cycling experiments), the initial potentiostatic charge reported in Figure 4-11 likely limited the overpotential to a range where hydrogen evolution was kinetically halted.[166]

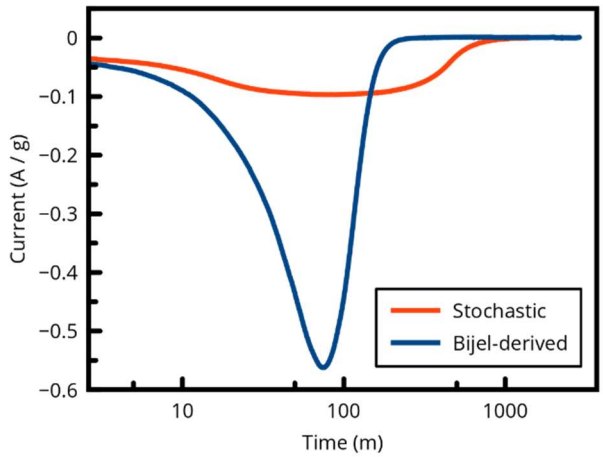

Figure 4-11. Representative curves for potentiostatic conversion of ZnO to Zn in 1 M KOH for different morphologies (logarithmic time scale).

We attribute the difference in charging behavior to the unique topological qualities of the bijel-derived electrode. The incomplete conversion of the stochastic electrode indicates that some regions in the microstructure were poorly accessible to either charge or electrolyte transport within the timescale of our experiment, while enhanced exposure and accessibility of active material to reactants in the bijel-derived structure enabled its efficient conversion.[159]

Representative raw measurements from galvanostatic charge/discharge cycles (here for a bijel-derived electrode) at C/5 are reported in Figure 4-13, and highlight two important aspects of the electrode's electrochemical behavior. First, in early stage, the electrodes can sustain current at C/5 for only about 1.5 h (instead of 5 h) before reaching the threshold overpotentials set in the experiment. This corresponds to an active material utilization of about 30% and indicates that the passivation layer has built up to a rate-limiting thickness at this point.[167] Second, this behavior changed during the cycling experiments, as shown by the qualitative difference between the left and right panels of Figure 4-13. Late-stage cycles were even shorter, which, as we will demonstrate shortly, corresponds to a loss in capacity and electrochemically-accessible active material. The experiment was terminated when the recoverable capacity fell below 10% of the first cycle. Charge cycling performed at higher rates than C/5 failed to reach a level of material utilization that highlights differences in the probed microstructures (see Figure 4-12).

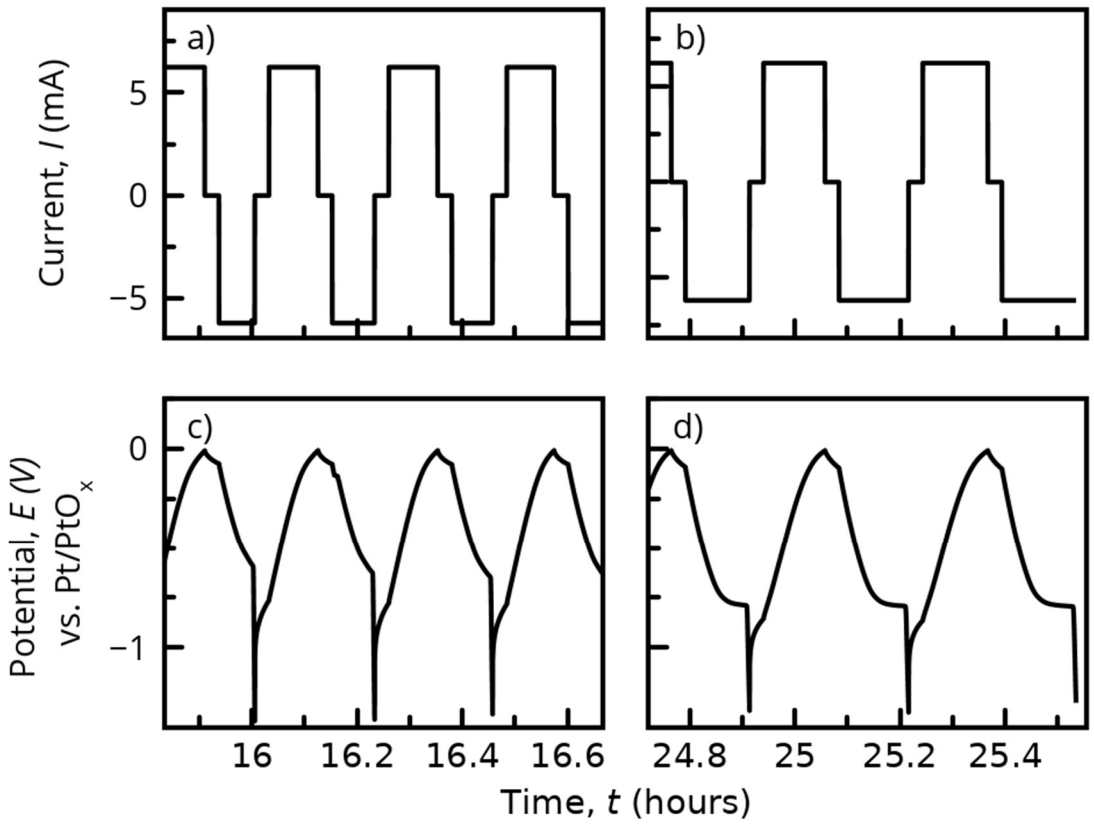

Figure 4-12. Current (a,b) and potential (c,d) throughout galvanostatic charge-discharge cycles at C1 for a bijel-derived electrode.

Repeatability of the experiments is demonstrated in Table 4.1, where measured capacities and 1st cycle material utilizations for all working electrodes is tabulated. Capacities normalized to zinc material at the working electrode were comparable to current state-of-the-art anodes.[151] Because the cell was designed with excess material at the counter electrode, the capacities normalized to the entire cell average 0.680 mA-h / g and 0.650 mA-h / g for the spinodal and stochastic electrodes, respectively. Using a silver or nickel counter electrode with a matched capacity would improve this metric.

Table 4.1. Capacity, utilization and depth of discharge for electrodes in the current study

	Specific Capacity (Potentiostatic charge)	Volumetric Capacity	1st Cycle Utilization at C/5	Depth of Discharge
B1 (5.99 mg)	763 mA-h / g-Zn	1.63 A-h / L-Zn	226 mA-h / g-Zn	29.7 %
B2 (12.7 mg)	748 mA-h / g-Zn	1.60 A-h / L-Zn	252 mA-h / g-Zn	33.7 %
B3 (12.6 mg)	753 mA-h / g-Zn	1.61 A-h / L-Zn	278 mA-h / g-Zn	37.6 %
S1 (6.22 mg)	734 mA-h / g-Zn	1.57 A-h / L-Zn	180 mA-h / g-Zn	24.5 %
S2 (11.2 mg)	685 mA-h / g-Zn	1.47 A-h / L-Zn	202 mA-h / g-Zn	29.5 %
S3 (14.3 mg)	751 mA-h / g-Zn	1.61 A-h / L-Zn	238 mA-h / g-Zn	34.7 %

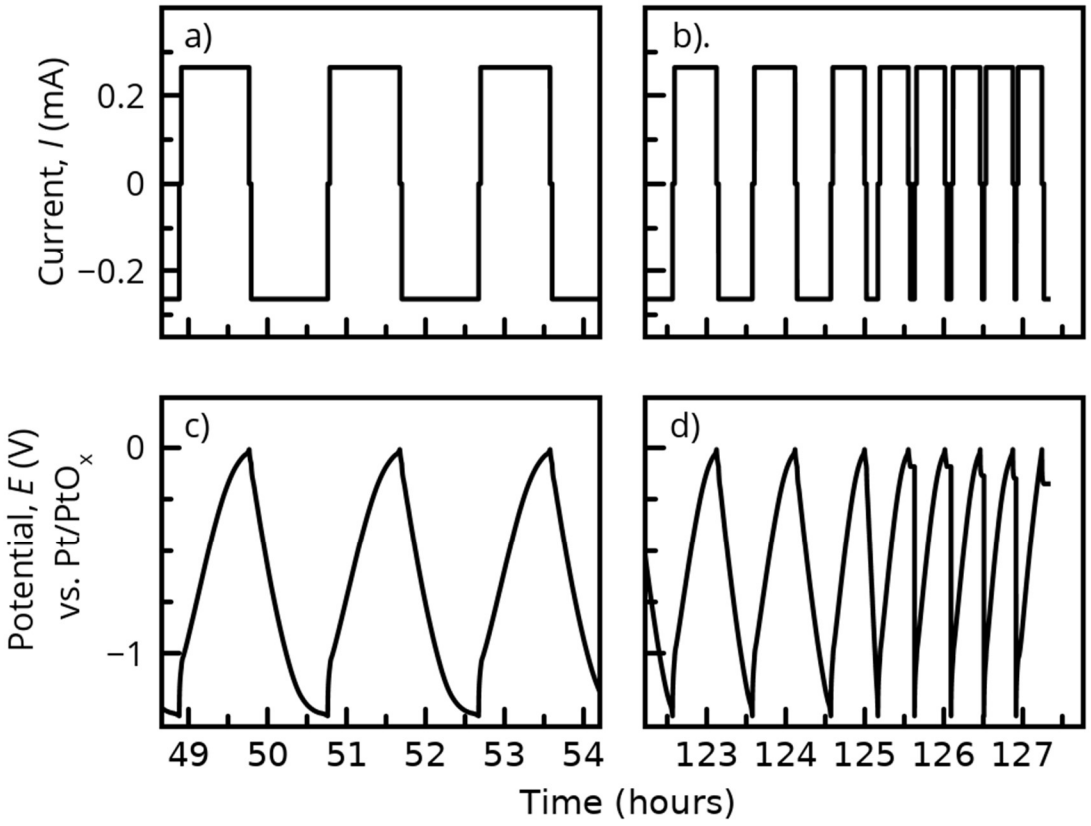

Figure 4-13. Current (a,b) and potential (c,d) throughout galvanostatic charge-discharge cycles for a bijel-derived electrode (B1) at C/5 rate. Reversible operation is observed during early cycles (a,c), but extended cycling degrades cell capacity, indicated by extremely short cycle times (b, d)

The recoverable capacities of various (a total of six) bijel-derived and stochastic electrodes, measured during the charge/discharge cycles as described earlier, are shown in Figure 4-14a,

alongside the Coulombic efficiency, shown in Figure 4-14b. Individual measurements are shown as filled symbols, and a ten-point moving average is indicated by a dashed line to help visualize each electrode's trend. The stochastic electrodes quickly lose capacity, reaching 50% of their initial values in approximately 35 cycles. This is consistent with previously published results with electrodes of similar morphology.[10] However, importantly, the bijel-derived electrodes are able to retain >90% of their initial capacities through the same cycling duty.

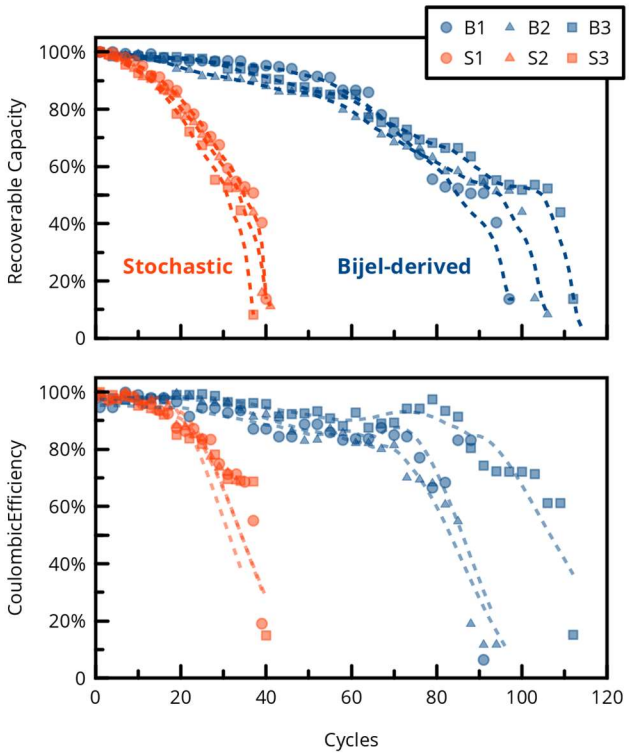

Figure 4-14. Recoverable capacities (top) and Coulombic efficiencies (bottom) of stochastic and bijel-derived electrodes during galvanostatic cycling.

Coulombic efficiency remained near 90% until the onset of rapid degradation. We propose that as material morphology evolved and active material became electrochemically inaccessible, water electrolysis was exacerbated by local overpotentials, a known inefficiency in zinc anodes that can be mitigated through the use of electrolyte additives or interface engineering of the electrodes.[168,169]

Interestingly, once the capacity has faded to approximately 50% of its first cycle value, the degradation rate becomes comparable between the two electrode types (this happens at approximately 30 and 100 cycles for the stochastic and bijel-derived electrodes, respectively). The microstructural characterizations that follow will help gain a deeper understanding of the morphological changes that accompany these transitions.

4.4.4. *Ex-Situ* Microstructural Analysis

Figure 4-15 shows SEM images of representative electrodes at various points during their electrochemical cycling. While the electrodes were shown in Figure 4-9 to have similarly smooth surfaces before any electrochemical activity, a roughened texture is observed on the stochastic structure after the initial charge and before galvanostatic cycling experiments. Immediate dendritic growth and roughening is apparent in the stochastic structures, while no change in sub-micron texture is observed in the bijel-derived materials for approximately 25 cycles. After 50 cycles, the bijel-derived material begins to develop chain-like features and non-uniform pore characteristics. Interestingly, as seen in Figure 4-14, the capacities of bijel-derived electrodes begin to fade noticeably past this point. This directly establishes a correlation between microstructure and electrochemical performance and introduces a new paradigm for mitigating capacity degradation in these systems.

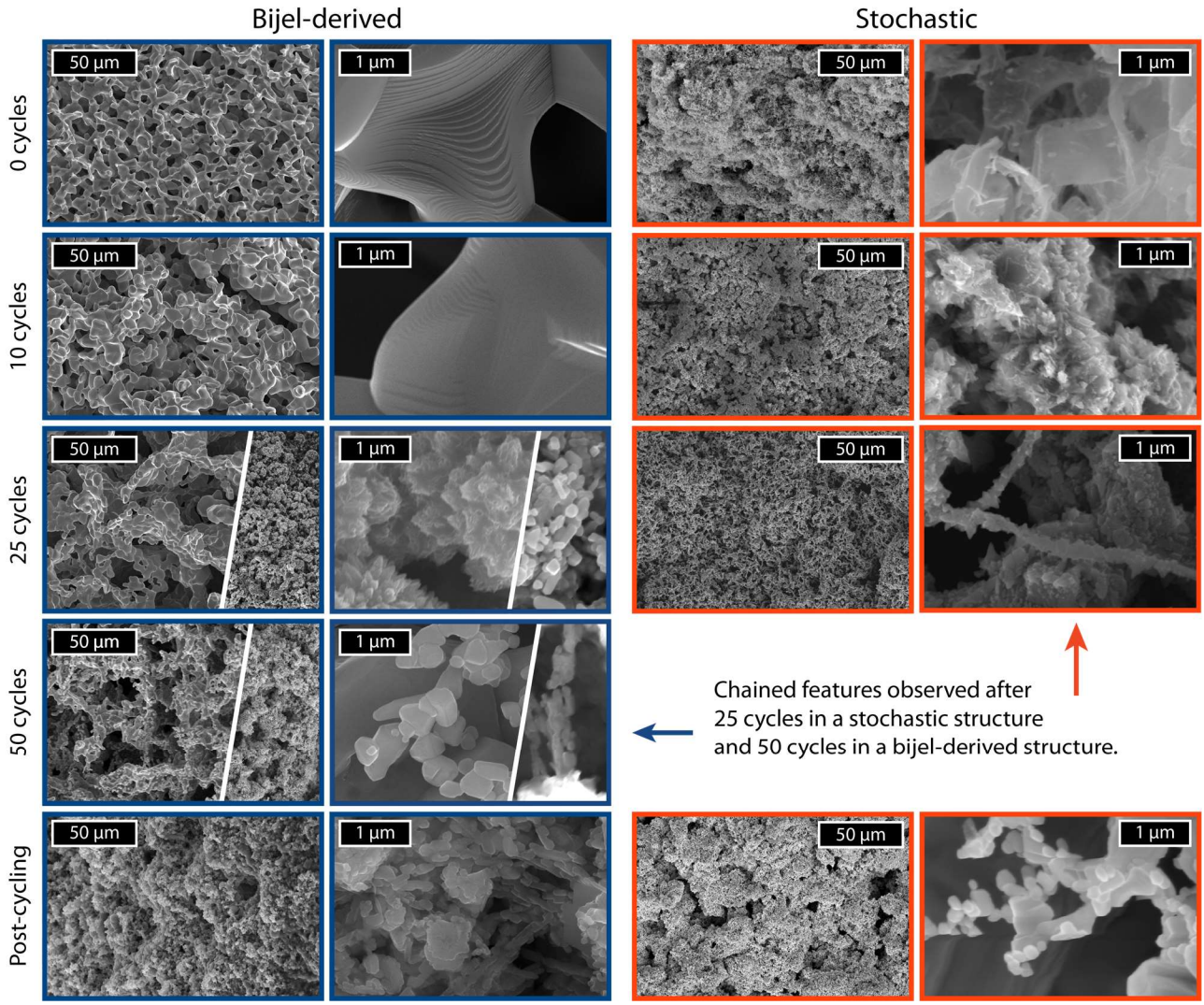

Figure 4-15: Photomicrographs of bijel-derived (left) and powder-derived (right) ZnO at (descending) 0, 10, 25, and 50 cycles. Bottom: Observations on the electrodes after failure. Split panels indicate that the observed microstructures were dissimilar in different parts of the sample.

During electrodeposition of Zn(O), the directed growth of dendrites is due in part to epitaxial registration.[162,170] In the case of charge cycling, active material at the surface is unlikely to maintain this registration given the continuous recrystallization as either oxide or metal. A crystallographic contribution to dendrite morphology is minimized and deposition is favored at sites that protrude into the electrolyte bulk as described previously by Lupo and Schlettwein.[161] The chained elements grown in this fashion create the so-called "mossy"

texture that has been reported and attributed to non-uniform current densities and overpotentials in the system.[171]

Parker, *et al.* have previously shown that maintaining a continuous, highly conductive metallic core will encourage a more uniform distribution of current within the electrode, and reduce hot spots that contribute to degradation and failure.[10,150] During discharge, active material directly in contact with the electrolyte is first to be converted, and the reaction front proceeds from the surface toward the center, resulting in a composite cross section with a highly conductive (Zn) core and a semiconducting (ZnO) shell.[172] Since the current I through an element with cross-sectional area A is $I = \int j \, dA$ where j is the current density, to maintain galvanostatic conditions (i.e. constant I) with a smaller conducting core available, j must increase, further exacerbating "hot spot" conditions in locations with narrow charge transport paths (throats between neighboring particles in a packed powder bed). Further, as these throats are fully converted to the semiconducting oxide, the remaining conduction pathways in other parts of the electrode are responsible for a disproportionate amount of current delivery, driving non-uniform utilization of active material.

The distribution of electric current through packed powder beds has also been considered in the context of the Field Assisted Sintering Technique (FAST), previously known as spark plasma sintering.[173] During FAST materials processing, an electric current is passed through a powder bed that simultaneously experiences external heating and uniaxial compression. These conditions work in concert to activate sintering mechanisms at temperatures lower than necessary for free sintering.[174] The governing mechanism underpinning this process remains controversial,[173] however it is generally accepted that during the initial stages of sintering, the electric field assists in densification through Joule heating at narrow connections between

particles carrying a disproportionate amount of current.[174,175] We expect that the stochastic electrodes, which are morphologically similar to the powder beds used in FAST processing, experience these same constrictions in current conduction pathways, creating a non-uniform electric field, which in this case results in over-utilization of locally accessible active material, aggressive material redistribution, and electrode degradation.

In a recent study, comparing key morphological characteristics among four different classes of porous materials, we have shown that bijel-derived structures have a characteristically tighter distribution of domain sizes and interfacial curvatures throughout the material, when compared to packed powders.[153] Motivated by the topological changes seen in our 2D discharge simulations, and our *ex-situ* microstructural observations, we postulate that the uniform domain size and interfacial curvature in our bijel-derived electrodes result in a more even distribution of current densities within the structure, mitigating imperfections, hot spot formation, and aggressive material redistribution, and delaying the cascade of microstructural events that lead to electrode degradation. This directly establishes a correlation between microstructure and electrochemical performance, and introduces strategies based solely on microstructural and topological design to mitigate capacity degradation in these systems. We expect that further improvements in bijel-processing techniques to provide near-perfect spinodal structures, combined with orthogonal strategies to improve performance such as utilizing electrolyte additives or adsorbed coatings on the active material, can pave the way for effective implementation of Zn-based electrodes and realization of their advantages and full potential for electrochemical energy storage and conversion.

4.5. Conclusions

During discharge, interruptions to the continuity of a Zn electrode can result in a non-uniform distribution of electric current and deactivation of otherwise reusable material. Electrodes derived from spinodal decomposition were predicted *via* computer simulations to resist these topological changes compared to commercial electrodes generated from packed powder beds of active material. To explore this concept, a spinodal-like microstructure was created by templating Zn precursors into self-assembled bijels and the electrochemical behavior compared to powder-derived analogs with random porosity. Material utilization in the bijel-derived electrode approaches 100%, suggesting enhanced electrochemical availability of active material compared to the stochastic configuration. Further, the spinodal design in these electrodes effectively delays both microstructural evolution and irreversible capacity loss, which occur almost immediately in the powder-derived electrodes. After 40 cycles, the bijel-derived electrodes retain over 90% of their first-cycle capacity, while the capacity of the powder analogs has decayed below 50%. These advantages are attributed to the uniformity and continuity of fluid phases in the template bijel, which are translated to the electrode and facilitate robust pathways for both electric charge and ionic transport. We also postulate the unique surface curvature metrics of the starting electrode material assists in uniform exposure of active material to the imposed electric field and the chemical potential, conditions necessary to support electrochemical energy storage.

5. On Deactivating the Void Phase of an Electrode

5.1. Abstract

Gas-evolving electrodes are important in many industrial processes, including water electrolysis for hydrogen and oxygen generation. High surface area electrodes generated *via* powder compaction and thermal densification are known to suffer from material deactivation induced by poor electrical connections throughout the electrode and limited reactant transport imposed by non-ideal pore geometry. Bicontinuous interfacially jammed emulsion gels (bijels) offer a template from which to create Ni electrodes with robust connections resistant to electrolyte stagnation, mitigating the deleterious bubble effect and limited current distribution in powder-derived electrodes. Nickel electrodes derived from bijel templates are shown herein to expel product gas faster than powder-derived analogs and require up to 25% less overpotential to drive water electrolysis at a given current density, resulting in reduced energy losses. These results suggest that the pore structure of spinodal-like electrodes encourages detachment of product gas from the electrochemically active surfaces, which in turn homogenizes the current density across the electrode surface.

5.2. Introduction

Gas evolving electrodes are important to many industrial processes, such as high purity H_2 generation with water electrolysis. The hydrogen economy is dependent on the cheap and efficient production of H_2 gas; however, economically viable technologies for H_2 generation tend to impart impurities that compromise downstream energy conversion operations or pollute the environment.[176,177] Electrolysis of water is a known route to high-purity H_2, but remains one of the most expensive of the available techniques.[178,179] This is due in part to energy losses associated with the overpotential (η) required to drive the hydrogen evolution reaction (HER) on

commercially viable substrates at a competitive rate (typically at least 300 mV).[165,180,181] Current research to reduce these energy losses focuses strongly on improving electron transfer to reactants through nanostructured materials and catalysts[19,182], but on larger length scales, mass transport of the reactants has an important influence on overall system efficiency.[183–186]

Electrodes are often configured in a porous structure to increase available surface area over which to carry out an electrochemical reaction.[14] Electrodes derived from powder metallurgy or felted materials are convenient to manufacture on an industrial scale and satisfy the requirement for increased surface area;[28] however, during gas evolution, the product bubbles can present unique impediments to efficient operation. Similar to how connections in the solid phase can promote charge distribution and homogenize current density, a well-connected pore phase is expected to enhance electrolyte transport across the catalytically active surface, serving to both replenish reactants and improve release of the product gas.[187] In addition to compromised electrolyte conductivity,[188,189] bubbles adsorbed to the interface reduce the amount of electrochemically available surface area.[184] Together, these phenomena increase activation overpotential and decrease energy storage efficiency.[190] Surfactants,[191] convection,[192] and surface texture[187] have been proposed to mitigate these issues and offer strategies to compliment a fundamental understanding of the microstructural contribution to these challenges.[17,19,186,187] Recently reported microstructures include urchin-like,[19] honeycomb-like,[193] and bubble-templated morphologies;[194] however, these approaches fail to address simultaneously all of the processes that benefit from microstructural design. Such attributes are uniquely realized in electrodes derived from spinodal decomposition due to the inherently bicontinuous and uniform morphologies that spontaneously emerge during this form

of demixing.[195–197] We hypothesize that these qualities will work in concert to limit kinetic impediments during electrochemically driven gas evolution imposed by the microstructure, including dead ends, constrictions, tortuosity, and closed porosity as illustrated in Figure 5-1.[187]

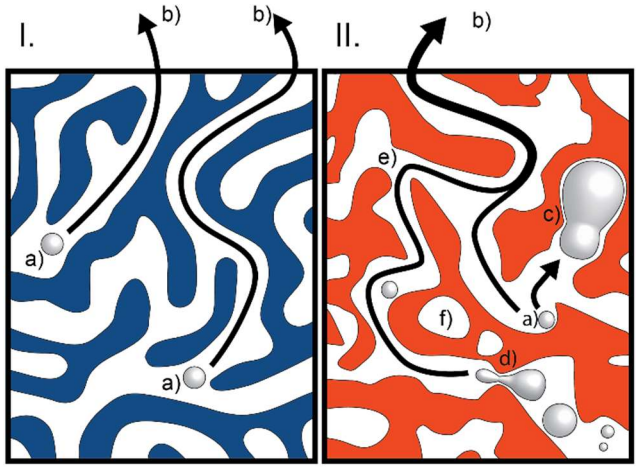

Figure 5-1: Schematic of bubbles moving from reaction sites (a) to the electrode exterior (b) through spinodal-like (I) and stochastic (II) structures. Non-idealities illustrated in (II) include dead-ends (c), constrictions (d), tortuosity (e), and closed porosity (f).

Bijels (bicontinuous interfacially jammed emulsion gels) provide a processing route toward porous materials with spinodal-like microstructure.[195] These emulsions are created by adsorbing particles to the interface of partially miscible fluids during spinodal decomposition. As the microstructure matures during this demixing, the interfacial area between the fluids is decreased until the particles come into contact and halt the coarsening.[195,198,199] Through a variety of templating techniques, this unique structure can be conferred to porous and composite materials with enhanced functional properties.[153] Electrodes previously synthesized *via* this process have been shown to benefit from availability of active material and high connectivity within the solid and void phases.[200,201] Together, these qualities encourage a homogenous distribution of reactants throughout the structure, which promotes uniform activity throughout

the volume. In the following study, we show that these qualities are active during operation as a hydrogen evolving cathode and serve to expel gas about twice as fast in bijel-templated electrodes than in electrodes with stochastically generated porosity. In addition to this, overpotential required to drive the HER is up to 25% lower in bijel-derived electrodes, suggesting a reduction in energy losses during gas evolution.

5.3. Materials and Methods

All materials were purchased from Sigma-Aldrich of St. Louis, MO unless otherwise noted. All water was purified to >18MΩ resistance (Millipore, Burlington MA). The methods to create the porous electrodes used in this study are illustrated schematically in Figure 5-2and described in detail below. Briefly, samples with randomly arranged pores were generated by blending Ni powder (<150 μm) with a variety of combustible starch-based pore formers and pressing uniaxially at 70 MPa in a custom steel die. Spinodal-like materials were synthesized by electroless deposition of a polymeric scaffold templated from a water-lutidine emulsion, similar to previous reports.[200] Electrodes were heat treated to remove the polymeric template and densify the metallic structure.

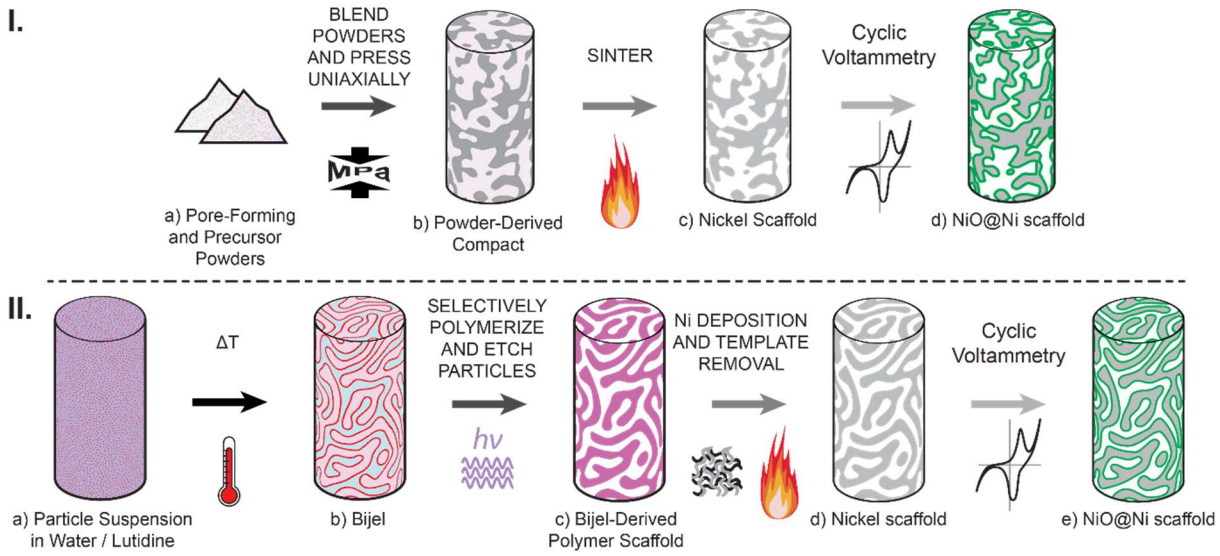

Figure 5-2: Processing routes to create powder-derived (I) and bijel-derived (II) porous nickel scaffolds

5.3.1. Powder-Derived Nickel Scaffolds

As shown in Figure 5-2 I, samples with randomly arranged pores were generated by blending 99.9% Ni powder (CAS# 7440-02-0, Sigma Aldrich, <150 μm) with combustible starch-based pore formers at 50 volume% and pressing uniaxially at 70 MPa in a custom steel die. Starches derived from corn, potato, and arrowroot were used in the combustible phase to provide a range of pore sizes.

The compacted powders were heat treated in an atmosphere-controlled quartz tube furnace in air with two 3 h steps at 300 °C and 500 °C to remove the combustible materials, followed by an 8 h reduction / sintering process under 10% H_2 / 90% Ar at 800 °C to produce metallic Ni compacts. A Ni wire current collector was attached to the compact with tin solder paste (Iso-Tip, Altoona WI) and shielded from the electrochemical experiment with polymeric epoxy (Epofix, Streuers, Cleveland, OH). Prior to electrochemical testing, unshielded solder and organics from processing were removed from the surfaces *via* 1 M HCl (CAS# 7647-01-0, ThermoFisher Scientific, Waltham MA).

5.3.2. Bijel-Derived Nickel Scaffolds

5.3.2.1. Synthesis of Silica Particles

Spherical silica particles (average diameter of 440 ± 20 nm) were synthesized *via* a modified Stöber process described in previously.[195,202] Briefly, 4180 µL of tetraethylorthosilicate (CAS# 78-10-4) was hydrated and polymerized in 44 g anhydrous ethanol (EtOH, CAS# 64-17-5, Gold Shield Distributors, Hayward CA), with added strong ammonia (~15 M NH_4OH, CAS# 1336-21-6, ThermoFisher Scientific, Waltham MA) to both catalyze the reaction and provide water for hydrolysis. A fluorescent dye was incorporated into the silica matrix by conjugating 12.5 mg rhodamine B isothiocyanate (CAS# 36877-69-7) with 26.2 µL aminopropyltriethoxysilane (CAS# 919-30-2, TCI America, Portland OR) in 10 mL EtOH for 24 h and mixing 5 mL of this solution into the alcohol/ammonia Stöber bath. After 24 h of growth and nucleation, the silica particles were rinsed in water five times *via* centrifuge and dried under vacuum (~25 in Hg) at 135°C until they reach neutrally wetting conditions with respect to a water and 2,6-lutidine (CAS# 108-48-5).

5.3.2.2. Bijel-Templated Polymer Scaffolds

The characteristic domain size for a bijel emulsion is inversely proportional to particle loading in the initial suspension[198]. The pore size in the Ni electrodes derived from bijel processing is related to the domain size of the template emulsion, allowing us to tailor the structures to match those created through the stochastic (power-derived) process. To create these emulsions, silica was first dispersed in a critical point mixture of water and 2-6 lutidine (69:31 by volume) at approximately 1.5, 3.0, and 6.0 volume% for target domain sizes of 60, 30, and 15 µm respectively (Figure 5-2, IIa). 205 µL of this suspension was dispensed into custom vials (5 mm inner diameter cylindrical glass tubes) and heated above the lower critical solution

temperature (LCST) of 34 °C with 10 s of microwave radiation at 300 W in order to quickly and homogeneously induce spinodal decomposition (Figure 5-2, IIb). After demixing, 35 µL oligomer solution comprising polyethylene glycol diacrylate of molecular weight ≈ 250 (PEGDA, CAS# 26570-48-9) and 1 volume% 2-hydroxy-2-methylpropiophenone (Darocur® 1173, CAS# 7473-98-5, Ciba Specialty Chemicals, Basel Switzerland) photo initiator was placed on the top of each sample and allowed to selectively diffuse into the lutidine-rich phase for 4 h. During this diffusion process, the temperature of the bijels were maintained at 70 °C (above the mixture's LCST) to prevent remixing. The lutidine-rich phase was then photopolymerized *via* 100 W UV for 100 s (Model S1000, EXFO, Quebec Canada) and the water-rich phase drained. After polymerization, the silica particles were etched from internal surfaces of the PEGDA with an 8 h treatment in 6 M hydrofluoric acid (CAS# 7664-39-3). The resulting scaffold was free standing and stable at room temperature and was subsequently used as a template onto which Ni can be deposited (Figure 5-2, IIc).

5.3.2.3. Metallization *via* Electroless Nickel Deposition

Ni precursors were deposited *via* electroless deposition on the polymer scaffolds. PEGDA was first saturated with a 0.1 M $PdCl_2$ (CAS# 7647-10-1) catalyst solution in 1:1 EtOH:water and allowed to dry before rinsing in isopropanol (IPA, CAS# 67-63-0, ThermoFisher Scientific, Waltham MA) to remove excess catalyst. A bath of 10 mL water with 1 volume% 1-propanol (CAS# 71-23-8, ThermoFisher Scientific, Waltham MA) was adjusted to pH 10 with NaOH **(**CAS# 1310-73-2, ThermoFisher Scientific, Waltham MA**)** and heated in an ultrasonic bath to 60 °C. The catalyst treated PEGDA scaffolds were added to the bath before dropwise addition of a 20 mL precursor solution comprising 0.02 M $NiCl_2$ (CAS# 7791-20-1, ThermoFisher Scientific, Waltham MA), 0.02 M Na-tartrate (CAS# 6106-24-7), and 1 M N_2H_4 (CAS# 10217-

52-4). After complete addition of the precursor solution, the Ni was allowed to deposit for an additional 48 h. The samples subsequently turned black and were reactive to magnetic stirring, indicating a successful metallization. Samples were removed from the plating bath, rinsed with IPA, and dried in an oven at 70 °C before heat treatment to remove the template and sinter the metal into a mechanically robust structure.

The heat treatment process described previously was used for bijel-derived samples as well. Heat treatment steps at 300 °C (3 h) and 500 °C (3 h) removed the PEGDA, followed by an 8 h reduction / sintering step under 10% H_2 / 90% Ar at 800 °C. A Ni wire current collector was attached to the metal scaffold with tin solder and shielded with epoxy. Prior to electrochemical testing, samples were cleaned in 1 M HCl to dissolve unshielded solder and remove organics from the surface.

5.3.3. Planar Samples

To test the intrinsic catalytic properties of the different starting materials and the effects of sub-micron texture under our testing conditions,[187,203] planar electrodes were created from the powder stock used in creating porous samples, electroless Ni, and a 99.99% Pure nickel extrudate (Goodfellow, Coraopolis PA). The planar powder-derived sample was created *via* 9 hours of hot pressing at 50 MPa and 1000 °C and sectioned to present a rectangular planar region to the electrochemical experiment. The electroless Ni was pressed uniaxially at 50 MPa into a planar configuration and heat treated alongside the porous samples in the process described above. Four identical sections of the high purity Ni standard were polished to a mirror finish with <0.1 μm diamond media (Buehler, Lake Bluff IL) and scratches were controllably reintroduced to three of the surfaces *via* diamond impregnated lapping films (0.5, 1.0, and 3.0 μm media).

5.3.4. Characterization

5.3.4.1. Microscopy

Scanning electron microscopy (SEM) was performed on a FEI Magellan (Model 400 ThermoFisher Scientific, Waltham MA) microscope equipped with a field emission electron source. All images were collected using an accelerating potential of 10 kV and a current of 0.10 nA. Conductive coatings were not necessary because the intrisic conductity of the Ni samples was sufficient to mitigate charging during the experiments. Brightness and contrast settings were adjusted independently in each image based on the contributions from local topology.

5.3.4.2. μCT

To evaluate porosity of representative samples, X-ray Computed Tomography (μCT) was performed on a Xradia VersaXRM™ (Model 410, Zeiss Microscopy, Jena Germany). 3-Dimensional reconstructions of the raw data were created from DICOM stacks in the ScanIP® module of Simpleware® (Synopsis, Mountain View CA). Ni provides sufficient X-ray scattering length and the volume of the solid phase can be reliably distinguished from the pore phase for comparison on a volumetric basis.

5.3.4.3. Analysis of Degassing Rates *via* Image Analysis

Measuring latency of gas escape from the electrode during the HER provides a rudimentary indicator of the residence time of product and efficiency of mass transport through the pore phase. To directly quantify this, samples were mounted in optical cuvettes and imaged before, during, and after steady-state operation as a H_2-evolving cathode. Images were captured with a DSLR (Rebel EOS Ti3, Canon, Tokyo Japan) and telephoto macro lens (K2 DistaMax™, Infinity Optics, Denver CO). This setup is illustrated schematically in Figure 5-3.

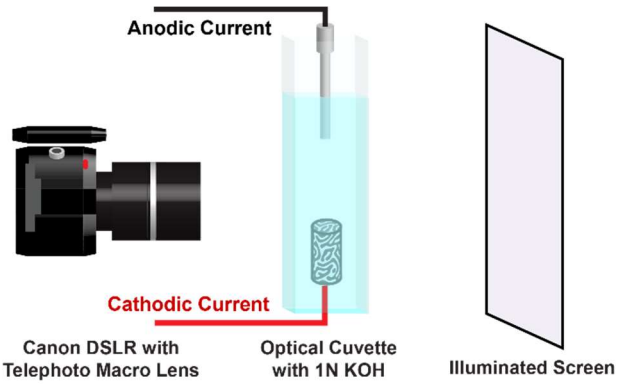

Figure 5-3: Schematic illustration of the imaging setup used to quantify gas escape from the porous electrodes.

The amount of gas in each frame was quantified by identifying a region of interest (1.85 megapixels) approximately 5 mm above the electrode and applying a threshold filter to binarize the image. The areal fraction of black pixels in the frame is directly related to the amount of gas being released by the electrode, verified by a calibration curve generated from a planar electrode presenting no microstructural impediment to gas release. Galvanostatic experiments were carried out between 0 and -300 μA for 20 m before steady state measurements. Turning this current off and measuring the rate of bubbles escaping the electrode allows a quantitative comparison of the transport kinetics between electrodes.

5.3.4.4. Electrochemical Testing

All electrochemical experiments took place in 1 M KOH with a Pt counter electrode. The potential (E) was measured *vs.* a Ag/AgCl (1 M KCl) reference electrode. Cyclic voltammetry (CV) experiments were performed with a Solatron CellTest System (Model 1470E, Ametek, Berwyn PA), and the galvanostatic experiments were driven by a Keithley Sourcemeter (Model 2400, Tektronix, Beaverton OR) with E tracked by the Solartron instrument. This split configuration decoupled E measurements from the power supply to take advantage of the stable current from the Keithley Sourcemeter and fast polling rate through the Solartron. The

instruments were grounded together external to the experiment. This configuration is illustrated schematically in Figure 5-4.

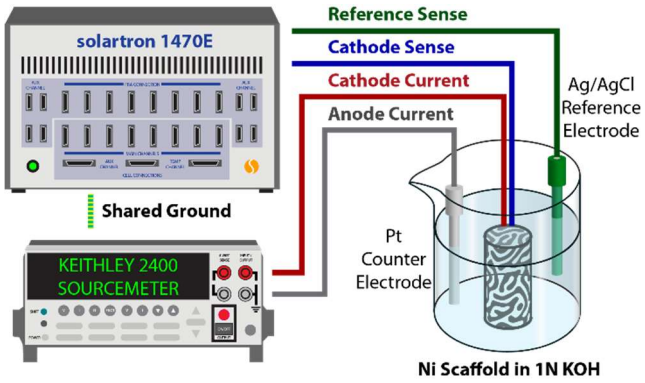

Figure 5-4: Configuration of the electrochemical devices used to measure η in the study.

The electrochemically active surface area was calculated *via* CV by comparing the magnitude of faradaic peaks corresponding to $NiOOH \leftrightarrow Ni(OH)_2$ to samples of known surface area.[204] Peak currents were identified automatically by finding points that are zero in dI/dE and non-zero in d^2I/dE^2. Electrochemically active surface area can also be measured by comparing the pseudocapacitance associated with hydrogen adsorption/desorption during CV in the non-faradaic region, however, this was inappropriate for our samples because activation introduces roughness that influences these measurements Figure 5-5.

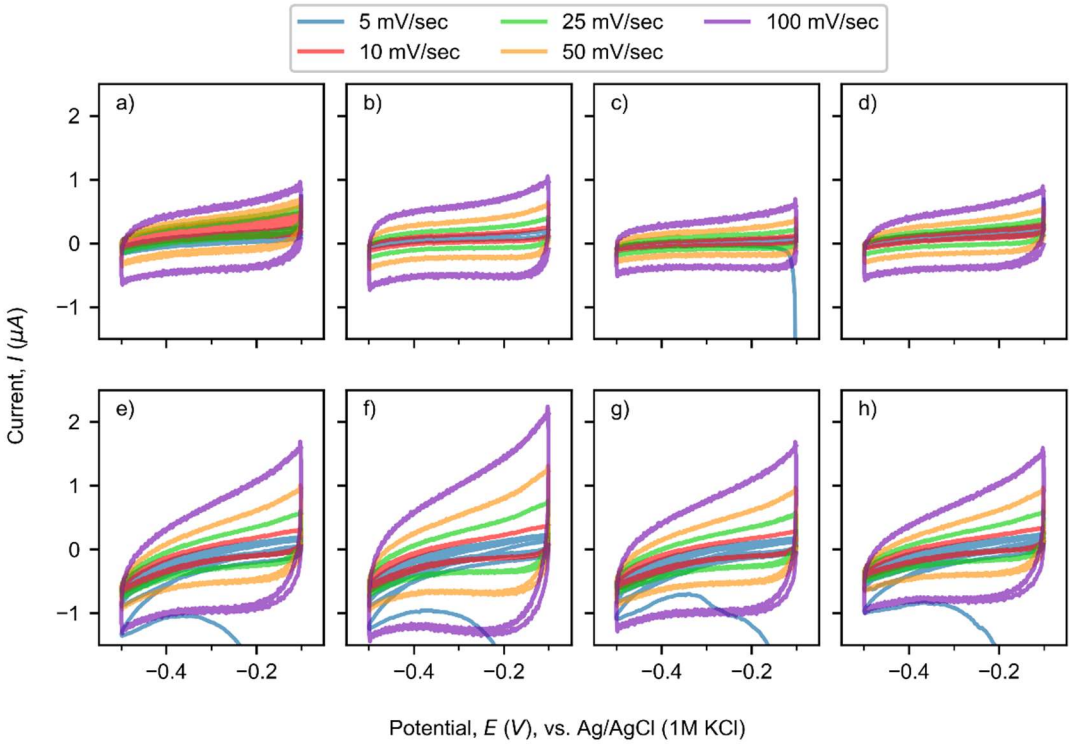

Figure 5-5: EDL measurements on highly polished nickel samples before (top) and after (bottom) electrochemical activation via cyclic voltammetry The samples were scratched to have controlled feature size: From left to right: Unscratched (<0.5 μm), 0.5 μm, 1 μm, and 3 μm media

To measure η required by each of the electrodes under steady state galvanostatic operation, experiments were performed at current densities (j) between -5 and -40 mA/cm^2. This range of current densities span a range over which the relationship between η and j can be compared to other studies [205,206]

5.4. Results and Discussion

5.4.1. Porosity and Morphology

Efficient diffusion of a species is expected to improve reaction kinetics and efficiency, but characteristics of the pore phase can significantly impede mass transport.[207–209] Volumetric porosity in samples for the current study is constant at 0.5, monitored throughout processing and

verified via μCT to be within 5% on representative samples. Given this equivalency, differences in the effective diffusivity can be attributed to tortuosity and constrictions in the transport pathways.[210] Photomicrographs of the two types of materials are presented in Figure 5-6 and show a qualitatively different structure between the samples and characteristics that are expected to influence operation as a gas-evolving electrode.

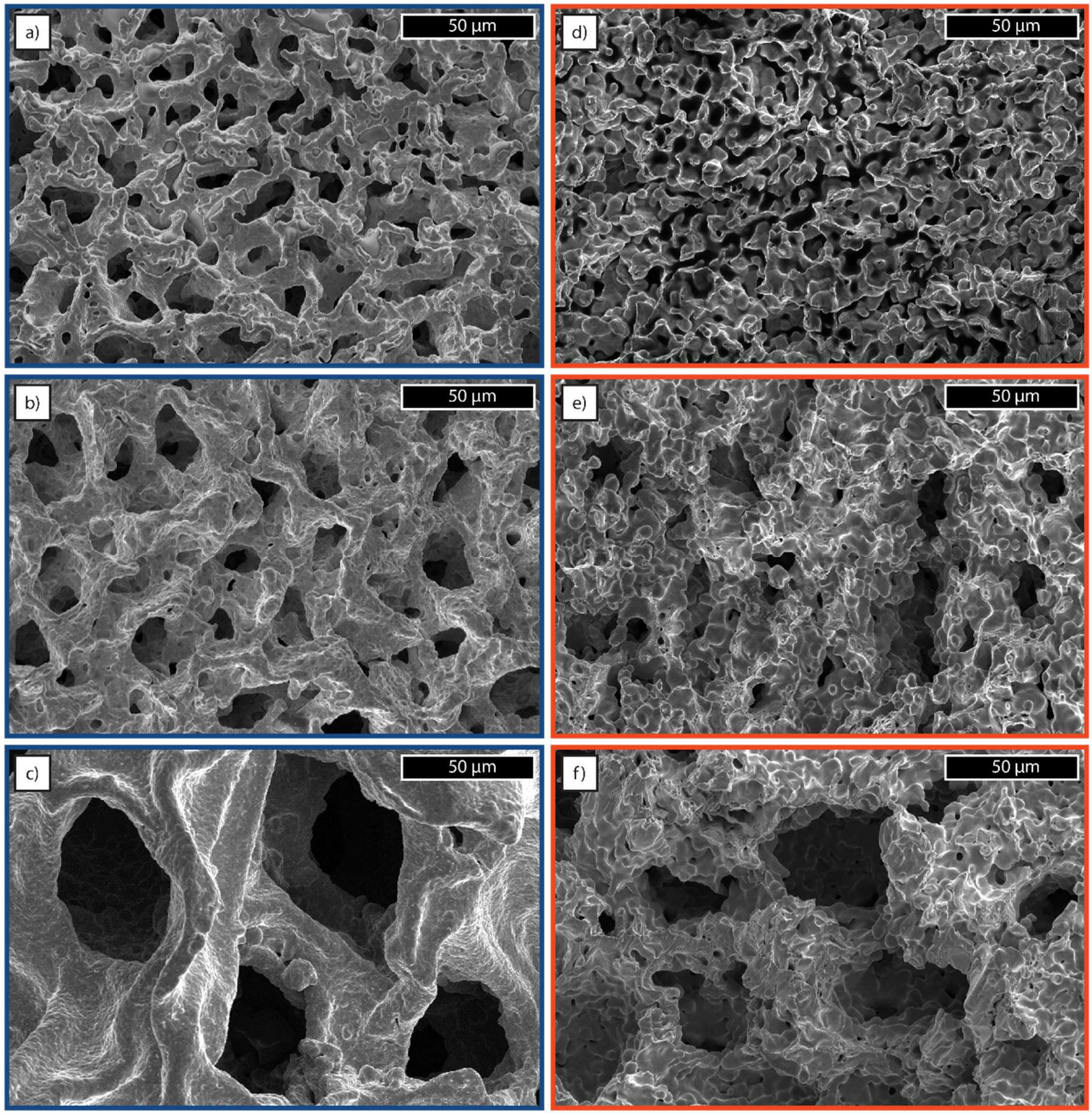

Figure 5-6: SEM images of bijel-derived (a - c) powder-derived (d - f) nickel electrodes. Characteristic pore size increases from top to bottom.

Specifically, pores in the spinodal-like electrodes are primarily on the length scale corresponding to the bijel from which they are templated. Conversely, powder-derived electrodes had porosity from both the combustible phase and interstitial spaces between elementary particles. Consequently, permeability and exposure of the active material surface is heterogeneous.[207] In addition, the bicontinuity inherent to spinodal decomposition encourages open porosity in bijel-derived samples, while the stochastically generated analogs are expected to suffer from dead ends or closed porosity.[153] This is supported by observations of the backs of some pores in the SEM images (pores in the top row appear relatively shallow because of the random pore morphology and associated tortuosity). These qualitative observations are consistent with previous studies that have quantified the microstructure of bijel-derived porous materials.[153,196]

We hypothesize that the well-connected porosity and uniform domain size characteristic of bijel-derived structures is more amenable to convection induced by buoyant migration of gaseous species. Convection through an electrode serves to quickly replenish electrolyte in the interior and remove the product gas, decreasing fractional gas coverage over active material surface and maintaining a homogeneous j during steady-state operation.[192] This effect is shown quantitatively with observations of the product gas escaping the electrode.

5.4.2. Image Analysis

To establish a relationship between current and observable product (bubbles), Figure 5-7 reports a calibration curve generated from a planar sample, which has no pore structure to impede transport of product gas. The results show a direct, near-linear relationship between the fraction of pixels obfuscated by bubbles (here termed the black level in frame) and the applied steady state current, confirming that the imaging configuration used successfully quantified

product gas with a reasonable degree of confidence. Similar calibration curves for each porous electrode are presented in Figure 5-8.

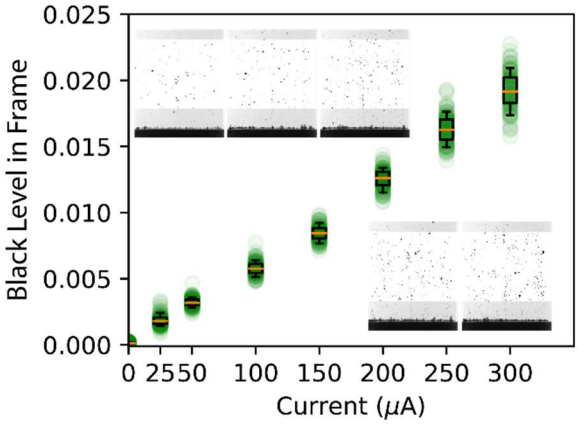

Figure 5-7: Calibration curve demonstrating near-linear relationship between current into an electrode and the quantification from thresholding given minimal impediment to escape of the product gas. Insets: example images from steady state operation at (left to right) 50, 100, 150, 200, and 250 μA.

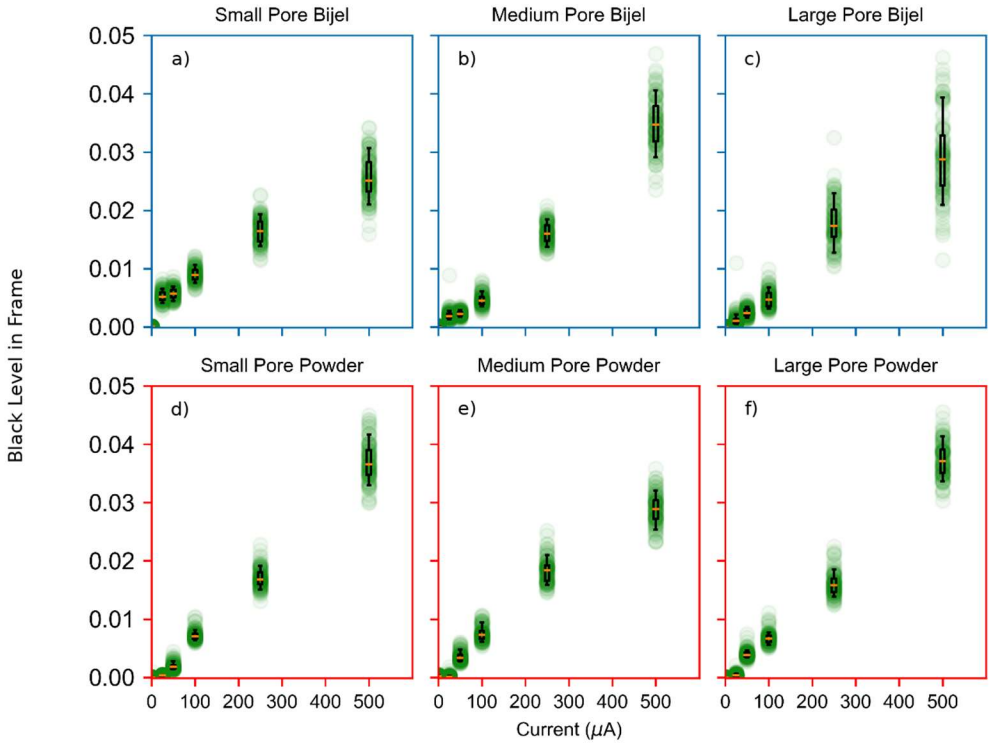

Figure 5-8: Calibration curves from porous media used in the study.

At currents above the boundaries established here, the electrode produced too much gas to be quantified reliably with this technique. To minimize this error, the steady state currents used to saturate the electrodes (and therefore representing the maximum in each experiment) was 100 or 250 μA, slightly less than the highest current presented in Figure 5-7 and within the linear relationship. Cutting electricity to the electrodes effectively stopped gas generation; however, product on the interior is trapped until it can fully navigate the pore phase, including any microstructural impediments. Quantification of the gas escaping porous electrodes during this degassing process is presented in Figure 5-9.

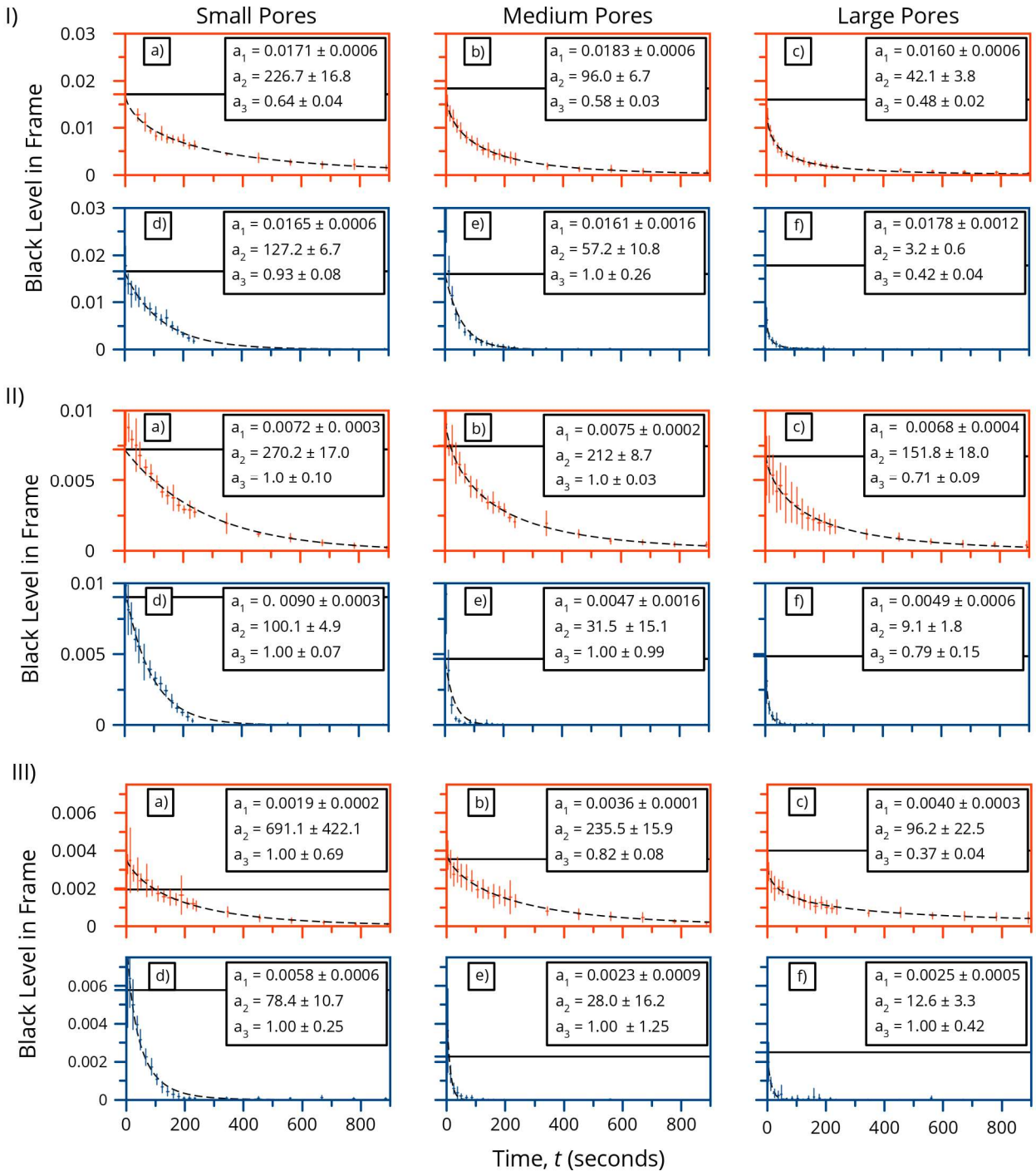

Figure 5-9: Data describing the decay kinetics from a steady state (indicated by the horizontal black lines). Data are fit to the stretched exponential function and parameters reported in each frame. Steady state currents from which the gas is generated were I) 250 μA, II) 100 μA and III) 50 μA. In general, powder derived electrodes (a-c) trapped gas longer than bijel-derived electrodes (d-f).

It is qualitatively obvious from observing the data that trapped gases take significantly longer to escape from electrodes with small or stochastically arranged pores. To quantify these observations, decay to zero black level is fit the stretched exponential function:

$$f(t) = a_1 * e^{\left(-\left(\frac{t}{a_2}\right)^{a_3}\right)}$$

The time constant in the stretched exponential function (a_2) indicates the characteristic time required for the observed product gas to reach the fraction $1/e$ of the steady state measurements. This parameter provides a basis with which the relative kinetics of mass transport can be compared across the electrodes. For each pore size, the time constant is consistently larger in fits to the data from stochastic electrodes. In addition to this microstructural contribution, the time constant also increases with smaller characteristic pore size. The longest decay period was observed in the powder-derived samples with the smallest pores - even after 20 m without current, product gas was observed escaping from the electrode.

These observations support the hypothesis that gas escape from spinodal-like morphologies can be more efficient than randomly generated porosity, but provides no information on the energy efficiencies associated with this advantage. Results from a more rigorous electrochemical investigation of the HER performed over the porous electrodes are described below.

5.4.3. Electrochemistry

5.4.3.1. Cyclic Voltammetry

Representative CV data for each sample type is shown in Figure 5-10.

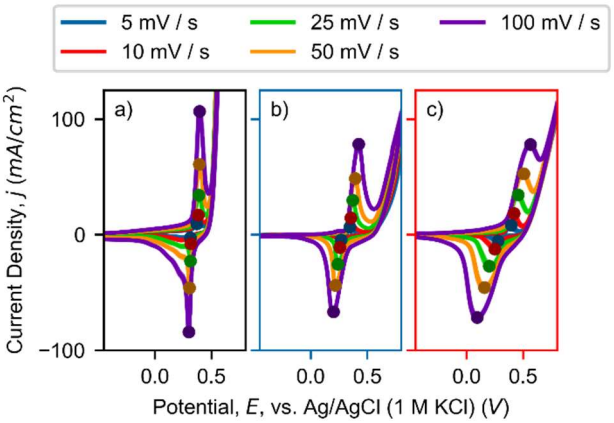

Figure 5-10: Representative cyclic voltammograms of the faradaic region in (a) planar, (b) bijel-derived, and (c) powder-derived samples. Pore size in (b) and (c) is approximately equal at 15 μm.

In addition to activating the surface through evolution of the catalytically functional oxides,[211] CV provides important information on the electrochemically available surface area[204] and diffusion of reactants in the electrode.[28] In every sample, cathodic and anodic peaks were observed between 0 and 0.75 V *vs.* Ag/AgCl (1 M KCl). The *E* of the observed maxima and minima were strongly dependent on sweep rate for the powder-derived electrodes, and nearly independent for planar samples. Bijel-derived electrodes were an intermediate case, where peak positions shifted only slightly. Additionally, the anodic NiO → NiO(OH) peaks were still well resolvable from that associated with the oxygen evolution reaction (OER) at strongly positive *E* (>0.65 V *vs.* Ag/AgCl). This observation is in agreement with previous measurements made on bijel derived Ni electrodes and suggests better exposure of the active surface area to the bulk electrolyte compared to stochastic materials.[200]

5.4.3.2. Galvanostatic experiments

To compare the η required to drive the HER at a given *j*, galvanostatic experiments were performed while measuring *E vs.* a Ag/AgCl (1 M KCl) reference electrode. Driving the HER at

a more aggressive j is expected to require a higher η. The relationship between these two values is frequently compared to evaluate the ability of a material to catalytically drive a reaction.[28,187] The so-called Tafel slope reports the change in potential required to accelerate a reaction by a factor of ten and is influenced by several underlying mechanisms, including fundamentally, the energy required to transfer electrons between surface species and reactants. This intrinsic value can be calculated with information about the reaction mechanism and is generally accepted to be around 110 mV/decade.[28,212] The Tafel relationship does not account for adsorbed gases and shielding of electrochemically active material, and a rigorous derivation of how this influences the relationship is beyond the scope of the current study. Nevertheless, the η - j relationship measured here is Tafel-like in nature, and qualitative trends across the experiments are clearly observable from the data reported in Figure 5-11.

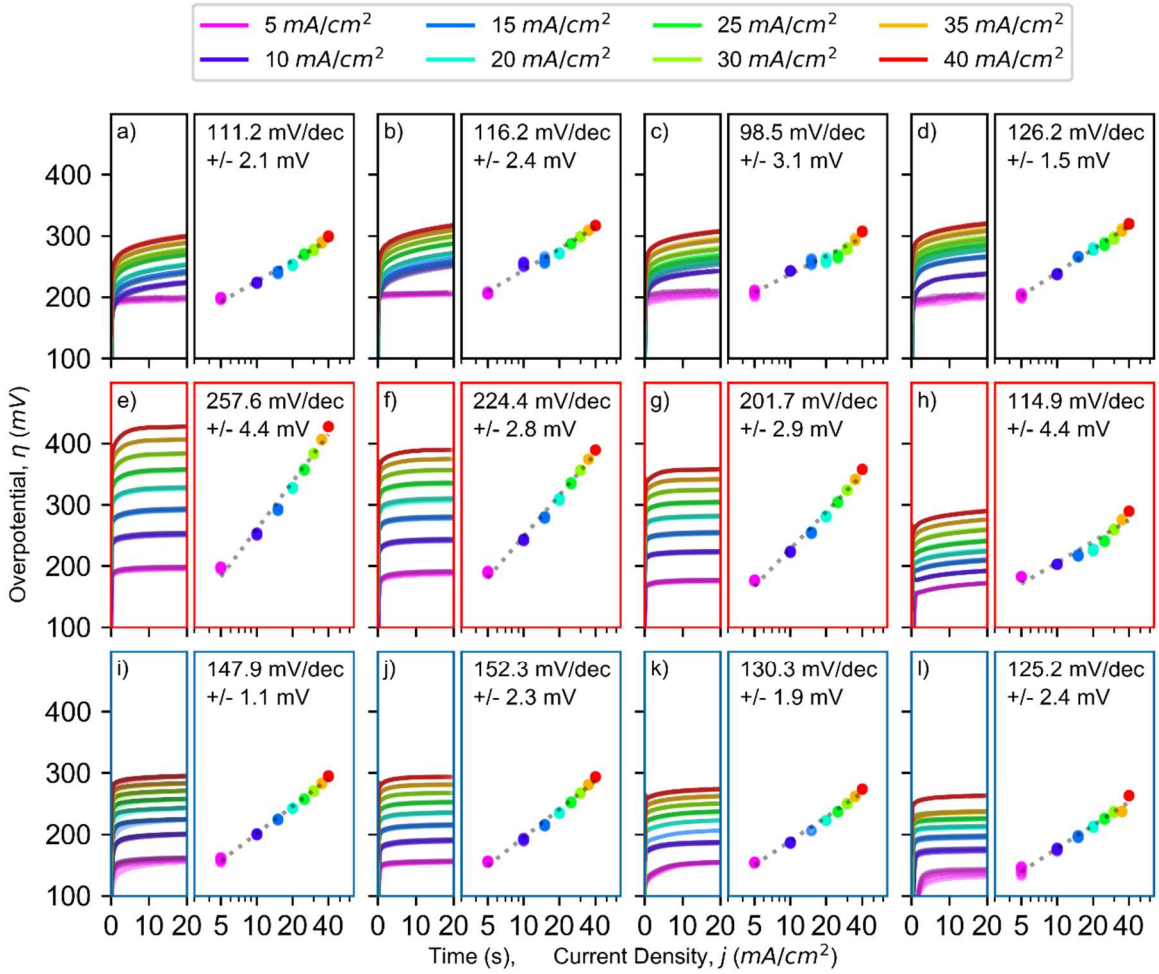

Figure 5-11: Split plots of η for all samples in the study. η with respect to time is reported in the left panels and values at t=20 s are projected onto the right axes to illustrate the relationship with j. A line of best fit is drawn through the data to demonstrate a qualitative comparison between slopes. a-d: flat samples with a range of scratch sizes. e-g: powder-derived (stochastic) samples with pore size increasing to the planar analog (h). i-k: Bijel-derived samples with pore size increasing to the planar analog (l).

Planar samples with variable surface texture (Figure 5-11 a-d) appear to have nearly the same slope in the η - j relationship, establishing the relatively small contribution from surface texture under these testing conditions. This relationship appears to be much more dependent on the pore arrangement in the sample, with porous electrodes experiencing a generally steeper η - j. Across these samples, the trend with pore size appears much stronger in powder-derived samples (Figure 5-11 e-g), with the steepest η - j relationship reported in panel e, corresponding to the smallest

pore size in stochastically arranged materials. Even the largest pore size in this configuration (Figure 5-11 g) has a noticeably steeper η - j curve than the corresponding planar electrode (Figure 5-11 h). Conversely, the bijel-derived samples do not suffer the same effect with reduced pore size. In other words, the η - j relationship for bijel-derived samples appears to be constant regardless of the effective domain size.

During steady state operation as a hydrogen evolving cathode, some fraction of the electrochemically available surface area is obfuscated by the adsorbed gases being produced and is consequently unavailable to participate in the HER. j on surfaces free of this shielding are artificially high, requiring more η to drive the reaction. We propose that this effect is more active in microstructures with small or stochastically arranged porosity that are prone to trapping the product. Surfaces with higher fractional coverage of gas require a higher η than surfaces with good exposure to the electrolyte, which can quickly release product into the electrolyte bulk and replenish reactants.

Electrode deactivation via bubble adsorption is especially damaging during electrolytic production of Al metal (termed the 'anode effect' in this context).[213] During the Hall-Héroult process, Al is separated electrocatalytically from a molten combination of Bayer process alumina and synthetic cryolite.[214] The metal is separated via siphon from the cathode, and the carbon anode reacts with O_2 to create byproduct CO_2 gas. This gas can be trapped against the electrode surface, resulting in the well-documented anode effect in which previously active surfaces are no longer in contact with the molten electrolyte and cannot participate in the reaction.[183,215] Non-uniform currents cause uneven wear and more frequent anode replacement in addition to

locally high η at sites unimpeded by adsorbed gases, which cause undesirable side-reaction and production of the potent greenhouse gases COF_2 and CF_4.[214,215]

5.5. Conclusions

Results from image analysis suggest improved transport of gaseous bubbles through porous media if the void phase is configured to reduce constrictions, dead ends, and tortuosity. The electrochemical results show clearly that porosity can increase the overpotential required to drive a reaction at a given rate and that this effect can be mitigated with a spinodal-like arrangement of pores in an electrode. Together, these results support the hypothesis that bijel-derived electrodes represent a unique configuration of active surface area and offer advantages to mass transport and electronic conductivity over similar powder-derived materials. These advantages are likely derived from uniformly sized features and good connectivity within the constituent phases, which together are expected to improve reactant transport, and distribute electrochemical activity homogeneously throughout the electrode volume. Understanding the contribution of the bubble effect to hydrogen generation is important to maximize efficiency in this specific application, but any process requiring transport of reactants in a gas phase (e.g. Al production or electrocatalytic CO_2 reduction) will benefit from minimizing this deactivation.

6. Summary and Future Work

This dissertation describes how bicontinuous interfacially jammed emulsion gels (bijels) can be used to stabilize a spinodal-like microstructure for functionalization as an electrochemical device, and how these electrodes are robust against deactivation *vs.* those with stochastically porous microstructures. Chapters 2 and 3 discuss the processing of bijel emulsions and the unique microstructural characteristics that are transferred to their derivatives. In general, these qualities are expected to homogenize electrochemical activity throughout the volume of an electrode and ultimately mitigate deactivation of an electrode by maintaining transport pathways for electronic and mass transport. Two specific applications described in Chapters 4 and 5 demonstrate this advantage by comparing bijel-derived electrodes to those built with stochastic porosity.

In Chapter 4, bijel templates were converted to Zn/ZnO electrodes that can be cycled between oxidized and metallic states to store energy electrochemically. As the oxidation (discharge) reaction proceeded from the electrode-electrolyte interface toward the interior of the solid phase, electronic conduction pathways were cut off, increasing resistance in the electrode. This resulted in locally high current densities and aggressive cycling, marked by dramatic morphological reconfiguration of the active material. Bijel-derived electrodes were shown to mitigate this effect and improve cyclability twofold. Simulations of this effect suggest this is due to the domain size and curvature uniformity that is characteristic of spinodal-like materials.

This homogeneity is mirrored in the pore phase, which plays an important role in the application Chapter 5. During operation as a gas-evolving electrode, product gas can become trapped in the pore structure and prevent some surfaces from participating in the electrochemically driven reaction, exacerbating energy losses. To explore this effect

experimentally, cathodic hydrogen evolution was performed using nickel electrodes in spinodal-like and stochastically porous configurations. Bijel-derived electrodes are observed to expel trapped gas about twice as fast as those with random porosity suggesting an advantage in mass transport derived from the uniform and well-connected porosity. This translates to a lower overpotential and improved efficiency associated with the reaction.

The templating described in the above chapters can be adapted to other electrochemical systems expected to benefit from robust transport, including energy storage devices like alkali-ion batteries (Na, K, Li),[2,7,9,216] carbon sequestration,[217] and catalytically active materials.[218]

REFERENCES

[1] The Future of the Grid Evolving to Meet America's Needs, Energetics Incorporated, 2014. http://energy.gov/sites/prod/files/2014/12/f19/Future%20of%20the%20Grid%20December%202014.pdf (accessed June 23, 2016).

[2] J.B. Goodenough, K.-S. Park, The Li-Ion Rechargeable Battery: A Perspective, J. Am. Chem. Soc. 135 (2013) 1167–1176. https://doi.org/10.1021/ja3091438.

[3] E.-Y. Jeong, Samsung to Recall Galaxy Note 7 Smartphone Over Reports of Fires, Wall Str. J. (2016). https://www.wsj.com/articles/samsung-to-recall-galaxy-note-7-smartphone-1472805076 (accessed March 11, 2019).

[4] P. Ping, Q. Wang, P. Huang, K. Li, J. Sun, D. Kong, C. Chen, Study of the fire behavior of high-energy lithium-ion batteries with full-scale burning test, J. Power Sources. 285 (2015) 80–89. https://doi.org/10.1016/j.jpowsour.2015.03.035.

[5] N. Nitta, G. Yushin, High-Capacity Anode Materials for Lithium-Ion Batteries: Choice of Elements and Structures for Active Particles, Part. Part. Syst. Charact. 31 (2014) 317–336. https://doi.org/10.1002/ppsc.201300231.

[6] F. Wu, G. Yushin, Conversion cathodes for rechargeable lithium and lithium-ion batteries, Energy Environ. Sci. 10 (2017) 435–459. https://doi.org/10.1039/C6EE02326F.

[7] M. Zhang, M. Shoaib, H. Fei, T. Wang, J. Zhong, L. Fan, L. Wang, H. Luo, S. Tan, Y. Wang, J. Zhu, J. Hu, B. Lu, Hierarchically Porous N-Doped Carbon Fibers as a Free-Standing Anode for High-Capacity Potassium-Based Dual-Ion Battery, Adv. Energy Mater. 9 (2019) 1901663. https://doi.org/10.1002/aenm.201901663.

[8] X. Wu, C.W.K. Lam, N. Wu, S.-S. Pang, Z. Xing, W. Zhang, Z. Ju, Multiple templates fabrication of hierarchical porous carbon for enhanced rate capability in potassium-ion batteries, Mater. Today Energy. 11 (2019) 182–191. https://doi.org/10.1016/j.mtener.2018.11.009.

[9] J.L. Kaufman, J. Vinckevičiūtė, S. Krishna Kolli, J. Gabriel Goiri, A. Van der Ven, Understanding intercalation compounds for sodium-ion batteries and beyond, Philos. Trans. R. Soc. Math. Phys. Eng. Sci. 377 (2019) 20190020. https://doi.org/10.1098/rsta.2019.0020.

[10] J.F. Parker, C.N. Chervin, E.S. Nelson, D.R. Rolison, J.W. Long, Wiring zinc in three dimensions re-writes battery performance—dendrite-free cycling, Energy Environ. Sci. 7 (2014) 1117. https://doi.org/10.1039/c3ee43754j.

[11] S. Higashi, S.W. Lee, J.S. Lee, K. Takechi, Y. Cui, Avoiding short circuits from zinc metal dendrites in anode by backside-plating configuration, Nat. Commun. 7 (2016) 11801. https://doi.org/10.1038/ncomms11801.

[12] S.J. Banik, R. Akolkar, Suppressing dendrite growth during zinc electrodeposition by PEG-200 additive, J. Electrochem. Soc. 160 (2013) D519–D523.

[13] M. Nie, D.P. Abraham, Y. Chen, A. Bose, B.L. Lucht, Silicon Solid Electrolyte Interphase (SEI) of Lithium Ion Battery Characterized by Microscopy and Spectroscopy, J. Phys. Chem. C. 117 (2013) 13403–13412. https://doi.org/10.1021/jp404155y.

[14] Z. Liu, T.W. Verhallen, D.P. Singh, H. Wang, M. Wagemaker, S. Barnett, Relating the 3D electrode morphology to Li-ion battery performance; a case for LiFePO4, J. Power Sources. 324 (2016) 358–367. https://doi.org/10.1016/j.jpowsour.2016.05.097.

[15] A. Esmanski, G.A. Ozin, Silicon Inverse-Opal-Based Macroporous Materials as Negative Electrodes for Lithium Ion Batteries, Adv. Funct. Mater. 19 (2009) 1999–2010. https://doi.org/10.1002/adfm.200900306.
[16] B.-K. Park, Q. Zhang, P.W. Voorhees, S.A. Barnett, Conditions for stable operation of solid oxide electrolysis cells: oxygen electrode effects, Energy Environ. Sci. (2019) 10.1039.C9EE01664C. https://doi.org/10.1039/C9EE01664C.
[17] Q. Zhou, J. Pu, X. Sun, C. Zhu, J. Li, J. Wang, S. Chang, H. Zhang, In situ surface engineering of nickel inverse opal for enhanced overall electrocatalytic water splitting, J Mater Chem A. (2017). https://doi.org/10.1039/C7TA03044D.
[18] J. S. Sakamoto, B. Dunn, Hierarchical battery electrodes based on inverted opal structures, J. Mater. Chem. 12 (2002) 2859–2861. https://doi.org/10.1039/B205634H.
[19] B. You, N. Jiang, M. Sheng, M.W. Bhushan, Y. Sun, Hierarchically Porous Urchin-Like Ni2P Superstructures Supported on Nickel Foam as Efficient Bifunctional Electrocatalysts for Overall Water Splitting, ACS Catal. 6 (2016) 714–721. https://doi.org/10.1021/acscatal.5b02193.
[20] R. Paul, V. Etacheri, V.G. Pol, J. Hu, Timothy.S. Fisher, Highly porous three-dimensional carbon nanotube foam as a freestanding anode for a lithium-ion battery, RSC Adv. 6 (2016) 79734–79744. https://doi.org/10.1039/C6RA17815D.
[21] B. Li, M. Gu, Z. Nie, Y. Shao, Q. Luo, X. Wei, X. Li, J. Xiao, C. Wang, V. Sprenkle, W. Wang, Bismuth Nanoparticle Decorating Graphite Felt as a High-Performance Electrode for an All-Vanadium Redox Flow Battery, Nano Lett. 13 (2013) 1330–1335. https://doi.org/10.1021/nl400223v.
[22] L. Wei, T.S. Zhao, G. Zhao, L. An, L. Zeng, A high-performance carbon nanoparticle-decorated graphite felt electrode for vanadium redox flow batteries, Appl. Energy. 176 (2016) 74–79. https://doi.org/10.1016/j.apenergy.2016.05.048.
[23] J.A. Witt, D.R. Mumm, A. Mohraz, Microstructural tunability of co-continuous bijel-derived electrodes to provide high energy and power densities, J Mater Chem A. 4 (2016) 1000–1007. https://doi.org/10.1039/C5TA06260H.
[24] M. Minsky, Microscopy apparatus, US3013467A, 1961. https://patents.google.com/patent/US3013467A/en (accessed November 21, 2019).
[25] M. Knoll, E. Ruska, Das Elektronenmikroskop, (n.d.) 22.
[26] M. Born, E. Wolf, Properties of Optics, Elsevier, 2013.
[27] J.I. Goldstein, D.E. Newbury, J.R. Michael, N.W.M. Ritchie, J.H.J. Scott, D.C. Joy, Scanning Electron Microscopy and X-Ray Microanalysis, 4th ed., Springer, 2017.
[28] A. Bard, L.R. Faulkner, Electrochemical Methods: Fundamentals and Applications, 2nd ed., John Wiley & Sons, Hoboken, NJ, 2001.
[29] M.-H. Park, K. Kim, J. Kim, J. Cho, Flexible dimensional control of high-capacity Li-ion-battery anodes: From 0D hollow to 3D porous germanium nanoparticle assemblies, Adv. Mater. 22 (2010) 415–418. https://doi.org/10.1002/adma.200901846.
[30] G.N. Bancroft, V.I. Sikavitsas, A.G. Mikos, Design of a flow perfusion bioreactor system for bone tissue-engineering applications, Tissue Eng. 9 (2003) 549–554. https://doi.org/10.1089/107632703322066723.
[31] L.E. Marshall, K.F. Goliwas, L.M. Miller, A.D. Penman, A.R. Frost, J.L. Berry, Flow–perfusion bioreactor system for engineered breast cancer surrogates to be used in preclinical testing, J. Tissue Eng. Regen. Med. 11 (2017) 1242–1250. https://doi.org/10.1002/term.2026.

[32] K.-L. Tung, C.-J. Chuang, Effect of pore morphology on fluid flow and particle deposition on a track-etched polycarbonate membrane, Desalination. 146 (2002) 129–134. https://doi.org/10.1016/S0011-9164(02)00504-0.
[33] J. Gröttrup, F. Schütt, D. Smazna, O. Lupan, R. Adelung, Y.K. Mishra, Porous ceramics based on hybrid inorganic tetrapodal networks for efficient photocatalysis and water purification, Ceram. Int. 43 (2017) 14915–14922. https://doi.org/10.1016/j.ceramint.2017.08.008.
[34] Y. Zhang, Y. Xia, Formation of embryoid bodies with controlled sizes and maintained pluripotency in three-dimensional inverse opal scaffolds, Adv. Funct. Mater. 22 (2012) 121–129. https://doi.org/10.1002/adfm.201101690.
[35] R.S. Moglia, J.L. Holm, N.A. Sears, C.J. Wilson, D.M. Harrison, E. Cosgriff-Hernandez, Injectable PolyHIPEs as high-porosity bone grafts, Biomacromolecules. 12 (2011) 3621–3628. https://doi.org/10.1021/bm2008839.
[36] A.N. Stachowiak, D.J. Irvine, Inverse opal hydrogel-collagen composite scaffolds as a supportive microenvironment for immune cell migration, J. Biomed. Mater. Res. A. 85A (2008) 815–828. https://doi.org/10.1002/jbm.a.31661.
[37] W.L. Murphy, R.G. Dennis, J.L. Kileny, D.J. Mooney, Salt fusion: An approach to improve pore interconnectivity within tissue engineering scaffolds, Tissue Eng. 8 (2002) 43–52. https://doi.org/10.1089/107632702753503045.
[38] G. Wegmann, R. Gerling, F.-P. Schimansky, Temperature induced porosity in hot isostatically pressed gamma titanium aluminide alloy powders, Acta Mater. 51 (2003) 741–752. https://doi.org/10.1016/S1359-6454(02)00465-2.
[39] N. Nomura, T. Kohama, I.H. Oh, S. Hanada, A. Chiba, M. Kanehira, K. Sasaki, Mechanical properties of porous Ti–15Mo–5Zr–3Al compacts prepared by powder sintering, Mater. Sci. Eng. C. 25 (2005) 330–335. https://doi.org/10.1016/j.msec.2005.04.001.
[40] R. Su, G. Ruan, H. Nie, T. Xie, Y. Zheng, F. Du, J. Li, Development of high internal phase emulsion polymeric monoliths for highly efficient enrichment of trace polycyclic aromatic hydrocarbons from large-volume water samples, J. Chromatogr. A. 1405 (2015) 23–31. https://doi.org/10.1016/j.chroma.2015.05.067.
[41] H. He, W. Li, M. Lamson, M. Zhong, D. Konkolewicz, C.M. Hui, K. Yaccato, T. Rappold, G. Sugar, N.E. David, K. Damodaran, S. Natesakhawat, H. Nulwala, K. Matyjaszewski, Porous polymers prepared via high internal phase emulsion polymerization for reversible CO2 capture, Polymer. 55 (2014) 385–394. https://doi.org/10.1016/j.polymer.2013.08.002.
[42] S. Abraham, P. Kuppan, S. Raj, B. Salama, G.S. Korbutt, C.D. Montemagno, Developing Hybrid Polymer Scaffolds Using Peptide Modified Biopolymers for Cell Implantation, ACS Biomater. Sci. Eng. 3 (2017) 2215–2222. https://doi.org/10.1021/acsbiomaterials.7b00383.
[43] M. Li, M.J. Mondrinos, X. Chen, M.R. Gandhi, F.K. Ko, P.I. Lelkes, Co-electrospun poly(lactide-co-glycolide), gelatin, and elastin blends for tissue engineering scaffolds, J. Biomed. Mater. Res. A. 79A (2006) 963–973. https://doi.org/10.1002/jbm.a.30833.
[44] M.-T. Hsieh, B. Endo, Y. Zhang, J. Bauer, L. Valdevit, The mechanical response of cellular materials with spinodal topologies, J. Mech. Phys. Solids. 125 (2019) 401–419. https://doi.org/10.1016/j.jmps.2019.01.002.

[45] Y. Zhang, S. Wang, M. Eghtedari, M. Motamedi, N.A. Kotov, Inverted-colloidal-crystal hydrogel matrices as three-dimensional cell scaffolds, Adv. Funct. Mater. 15 (2005) 725–731. https://doi.org/10.1002/adfm.200400325.
[46] H. Zhang, X. Yu, P.V. Braun, Three-dimensional bicontinuous ultrafast-charge and -discharge bulk battery electrodes, Nat. Nanotechnol. 6 (2011) 277–281. https://doi.org/10.1038/nnano.2011.38.
[47] C.F. Berg, Permeability description by characteristic length, tortuosity, constriction and porosity, Transp. Porous Media. 103 (2014) 381–400. https://doi.org/10.1007/s11242-014-0307-6.
[48] G.S. Armatas, Determination of the effects of the pore size distribution and pore connectivity distribution on the pore tortuosity and diffusive transport in model porous networks, Chem. Eng. Sci. 61 (2006) 4662–4675. https://doi.org/10.1016/j.ces.2006.02.036.
[49] H.-Y. Chen, Y. Kwon, K. Thornton, Multifunctionality of three-dimensional self-assembled composite structure, Scr. Mater. 61 (2009) 52–55. https://doi.org/10.1016/j.scriptamat.2009.03.006.
[50] A.H. Schoen, Infinite periodic minimal surfaces without self-intersections. NASA technical note D-5541, (1970).
[51] Y. Jung, S. Torquato, Fluid permeabilities of triply periodic minimal surfaces, Phys. Rev. E. 72 (2005) 056319. https://doi.org/10.1103/PhysRevE.72.056319.
[52] S. Zekoll, C. Marriner-Edwards, A.K. Ola Hekselman, J. Kasemchainan, C. Kuss, D.E. J. Armstrong, D. Cai, R. J. Wallace, F. H. Richter, J.H. J. Thijssen, P. G. Bruce, Hybrid electrolytes with 3D bicontinuous ordered ceramic and polymer microchannels for all-solid-state batteries, Energy Environ. Sci. 11 (2018) 185–201. https://doi.org/10.1039/C7EE02723K.
[53] H. Jinnai, Y. Nishikawa, T. Hashimoto, Curvature distributions of spinodal interface in a condensed matter system, Phys. Rev. E. 59 (1999) R2554–R2557. https://doi.org/10.1103/PhysRevE.59.R2554.
[54] M.E. Cates, P.S. Clegg, Bijels: a new class of soft materials, Soft Matter. 4 (2008) 2132. https://doi.org/10.1039/b807312k.
[55] D.A. Porter, K.E. Easterling, M. Sherif, Phase Transformations in Metals and Alloys, Third Edition, 3 edition, Routledge, Boca Raton, FL, 2009.
[56] M.H. Hillert, A theory of nucleation for solid metallic solutions, Thesis, Massachusetts Institute of Technology, 1956. https://dspace.mit.edu/handle/1721.1/17380 (accessed December 4, 2019).
[57] J.W. Cahn, On spinodal decomposition, Acta Metall. 9 (1961) 795–801. https://doi.org/10.1016/0001-6160(61)90182-1.
[58] W. Ramsden, F. Gotch, Separation of solids in the surface-layers of solutions and 'suspensions' (observations on surface-membranes, bubbles, emulsions, and mechanical coagulation).—Preliminary account, Proc. R. Soc. Lond. 72 (1904) 156–164. https://doi.org/10.1098/rspl.1903.0034.
[59] S.U. Pickering, CXCVI.—Emulsions, J. Chem. Soc. Trans. 91 (1907) 2001–2021. https://doi.org/10.1039/CT9079102001.
[60] R.J. Hunter, Foundations of Colloid Science, 2 edition, Oxford University Press, Oxford ; New York, 2001.

[61] S. Komura, Y. Hirose, Y. Nonomura, Adsorption of colloidal particles to curved interfaces, J. Chem. Phys. 124 (2006) 241104. https://doi.org/10.1063/1.2216697.
[62] K. Stratford, Colloidal Jamming at Interfaces: A Route to Fluid-Bicontinuous Gels, Science. 309 (2005) 2198–2201. https://doi.org/10.1126/science.1116589.
[63] E.M. Herzig, K.A. White, A.B. Schofield, W.C.K. Poon, P.S. Clegg, Bicontinuous emulsions stabilized solely by colloidal particles, Nat. Mater. 6 (2007) 966–971. https://doi.org/10.1038/nmat2055.
[64] M.N. Lee, J.H.J. Thijssen, J.A. Witt, P.S. Clegg, A. Mohraz, Making a Robust Interfacial Scaffold: Bijel Rheology and its Link to Processability, Adv. Funct. Mater. 23 (2013) 417–423. https://doi.org/10.1002/adfm.201201090.
[65] L. Imperiali, C. Clasen, J. Fransaer, C. W. Macosko, J. Vermant, A simple route towards graphene oxide frameworks, Mater. Horiz. 1 (2014) 139–145. https://doi.org/10.1039/C3MH00047H.
[66] M.N. Lee, A. Mohraz, Bicontinuous Macroporous Materials from Bijel Templates, Adv. Mater. 22 (2010) 4836–4841. https://doi.org/10.1002/adma.201001696.
[67] M. Reeves, K. Stratford, J.H.J. Thijssen, Quantitative morphological characterization of bicontinuous Pickering emulsions via interfacial curvatures, Soft Matter. 12 (2016) 4082–4092. https://doi.org/10.1039/C5SM03102H.
[68] J. Witt, D. R. Mumm, A. Mohraz, Bijel reinforcement by droplet bridging: A route to bicontinuous materials with large domains, Soft Matter. 9 (2013) 6773–6780. https://doi.org/10.1039/C3SM00130J.
[69] D. Cai, F. H. Richter, J.H. J. Thijssen, P. G. Bruce, P. S. Clegg, Direct transformation of bijels into bicontinuous composite electrolytes using a pre-mix containing lithium salt, Mater. Horiz. 5 (2018) 499–505. https://doi.org/10.1039/C7MH01038A.
[70] T.J. Thorson, E.L. Botvinick, A. Mohraz, Composite bijel-templated hydrogels for cell delivery, ACS Biomater. Sci. Eng. 4 (2018) 587–594. https://doi.org/10.1021/acsbiomaterials.7b00809.
[71] M.F. Haase, H. Jeon, N. Hough, J.H. Kim, K.J. Stebe, D. Lee, Multifunctional nanocomposite hollow fiber membranes by solvent transfer induced phase separation, Nat. Commun. 8 (2017) 1234. https://doi.org/10.1038/s41467-017-01409-3.
[72] G. Di Vitantonio, T. Wang, M.F. Haase, K.J. Stebe, D. Lee, Robust bijels for reactive separation via silica-reinforced nanoparticle layers, ACS Nano. 13 (2019) 26–31. https://doi.org/10.1021/acsnano.8b05718.
[73] Y. Kwon, K. Thornton, P.W. Voorhees, Coarsening of bicontinuous structures via nonconserved and conserved dynamics, Phys. Rev. E. 75 (2007) 021120-1-021120–5. https://doi.org/10.1103/PhysRevE.75.021120.
[74] V.W.L. Chan, K. Thornton, Channel size distribution of complex three-dimensional microstructures calculated from the topological characterization of isodistance structures, Acta Mater. 60 (2012) 2509–2517. https://doi.org/10.1016/j.actamat.2011.12.042.
[75] J.W. Cahn, J.E. Hilliard, Free Energy of a Nonuniform System. I. Interfacial Free Energy, J. Chem. Phys. 28 (1958) 258–267. https://doi.org/10.1063/1.1744102.
[76] J.W. Cahn, J.E. Hilliard, Free energy of a nonuniform system. III. Nucleation in a two-component incompressible fluid, J. Chem. Phys. 31 (1959) 688–699. https://doi.org/10.1063/1.1730447.

[77] S.M. Allen, J.W. Cahn, A microscopic theory for antiphase boundary motion and its application to antiphase domain coarsening, Acta Metall. 27 (1979) 1085–1095. https://doi.org/10.1016/0001-6160(79)90196-2.
[78] S. Frijters, J. Harting, Self-assembled porous media from particle-stabilized emulsions, ArXiv14082974 Cond-Mat Phys. (2014). http://arxiv.org/abs/1408.2974 (accessed December 11, 2017).
[79] A. Van Blaaderen, A. Vrij, Synthesis and characterization of colloidal dispersions of fluorescent, monodisperse silica spheres, Langmuir. 8 (1992) 2921–2931. https://doi.org/10.1021/la00048a013.
[80] A.Y. Sergienko, H. Tai, M. Narkis, M.S. Silverstein, Polymerized high internal-phase emulsions: Properties and interaction with water, J. Appl. Polym. Sci. 84 (2002) 2018–2027. https://doi.org/10.1002/app.10555.
[81] Synopsis, INC, Simpleware: Converting 3D images into models. Reference guide version 2016.09-SP2, (2017).
[82] Young P.G, Beresford-West T.B.H, Coward S.R.L, Notarberardino B, Walker B, Abdul-Aziz A, An efficient approach to converting three-dimensional image data into highly accurate computational models, Philos. Trans. R. Soc. Math. Phys. Eng. Sci. 366 (2008) 3155–3173. https://doi.org/10.1098/rsta.2008.0090.
[83] Y. Agarwal, W. Smigaj, P.G. Young, R. Cotton, P. Tompsett, Image-based software solutions for advanced materials processing and characterization, Mater. Today Proc. (2017). https://doi.org/10.1016/j.matpr.2017.02.030.
[84] T.J. Thorson, K.M. McDevitt, E.L. Botvinick, D.R. Mumm, A. Mohraz, 3D volume reconstructions of porous materials from micro-computed tomography scans and computational geometry scripts in Python 3, Mendeley Data. Version 1 (2019). https://doi.org/10.17632/hpjtgt2847.1.
[85] C.H. Rycroft, VORO++: A three-dimensional Voronoi cell library in C++, Chaos Interdiscip. J. Nonlinear Sci. 19 (2009) 041111. https://doi.org/10.1063/1.3215722.
[86] H. Blum, A Transformation for extracting new descriptors of shape., Models Percept. Speech Vis. Form. (1967) 362–380.
[87] F. Sun, Y. Choi, Y. Yu, W. Wang, Medial meshes – A compact and accurate representation of medial axis transform, IEEE Trans. Vis. Comput. Graph. 22 (2016) 1278–1290. https://doi.org/10.1109/TVCG.2015.2448080.
[88] T.B. Sebastian, B.B. Kimia, Curves vs. skeletons in object recognition, Signal Process. 85 (2005) 247–263. https://doi.org/10.1016/j.sigpro.2004.10.016.
[89] S.A. Wilmarth, N.M. Amato, P.F. Stiller, Motion planning for a rigid body using random networks on the medial axis of the free space, in: Proc. Fifteenth Annu. Symp. Comput. Geom., ACM, New York, NY, USA, 1999: pp. 173–180. https://doi.org/10.1145/304893.304967.
[90] J.W. Brandt, V.R. Algazi, Continuous skeleton computation by Voronoi diagram, CVGIP Image Underst. 55 (1992) 329–338. https://doi.org/10.1016/1049-9660(92)90030-7.
[91] J. Ma, S.W. Bae, S. Choi, 3D medial axis point approximation using nearest neighbors and the normal field, Vis. Comput. 28 (2012) 7–19. https://doi.org/10.1007/s00371-011-0594-7.
[92] R. Peters, H. Ledoux, Robust approximation of the medial axis transform of LiDAR point clouds as a tool for visualisation, Comput. Geosci. 90 (2016) 123–133. https://doi.org/10.1016/j.cageo.2016.02.019.

[93] I.R. Porteous, Geometric Differentiation: For the Intelligence of Curves and Surfaces, second ed., Cambridge University Press, Cambridge, 2001.
[94] E.T. Lilleodden, P.W. Voorhees, On the topological, morphological, and microstructural characterization of nanoporous metals, MRS Bull. 43 (2018) 20–26. https://doi.org/10.1557/mrs.2017.303.
[95] J. Chen, J. Jester, M. Gopi, Fast computation of tunnels in corneal collagen structure, in: Proc. Comput. Graph. Int. 2018, ACM, New York, NY, USA, 2018: pp. 57–65. https://doi.org/10.1145/3208159.3208175.
[96] K.R. Mangipudi, E. Epler, C.A. Volkert, Topology-dependent scaling laws for the stiffness and strength of nanoporous gold, Acta Mater. 119 (2016) 115–122. https://doi.org/10.1016/j.actamat.2016.08.012.
[97] R. Mendoza, K. Thornton, I. Savin, P.W. Voorhees, The evolution of interfacial topology during coarsening, Acta Mater. 54 (2006) 743–750. https://doi.org/10.1016/j.actamat.2005.10.010.
[98] E.W. Dijkstra, A note on two problems in connexion with graphs, Numer. Math. 1 (1959) 269–271. https://doi.org/10.1007/BF01386390.
[99] N. Epstein, On tortuosity and the tortuosity factor in flow and diffusion through porous media, Chem. Eng. Sci. 44 (1989) 777–779. https://doi.org/10.1016/0009-2509(89)85053-5.
[100] C.J. Gommes, A.-J. Bons, S. Blacher, J.H. Dunsmuir, A.H. Tsou, Practical methods for measuring the tortuosity of porous materials from binary or gray-tone tomographic reconstructions, AIChE J. 55 (2018) 2000–2012. https://doi.org/10.1002/aic.11812.
[101] I.V. Zenyuk, D.Y. Parkinson, L.G. Connolly, A.Z. Weber, Gas-diffusion-layer structural properties under compression via X-ray tomography, J. Power Sources. 328 (2016) 364–376. https://doi.org/10.1016/j.jpowsour.2016.08.020.
[102] I.V. Thorat, D.E. Stephenson, N.A. Zacharias, K. Zaghib, J.N. Harb, D.R. Wheeler, Quantifying tortuosity in porous Li-ion battery materials, J. Power Sources. 188 (2009) 592–600. https://doi.org/10.1016/j.jpowsour.2008.12.032.
[103] T.B. Boving, P. Grathwohl, Tracer diffusion coefficients in sedimentary rocks: correlation to porosity and hydraulic conductivity, J. Contam. Hydrol. 53 (2001) 85–100. https://doi.org/10.1016/S0169-7722(01)00138-3.
[104] S. Peng, Q. Hu, S. Hamamoto, Diffusivity of rocks: Gas diffusion measurements and correlation to porosity and pore size distribution, Water Resour. Res. 48 (2012). https://doi.org/10.1029/2011WR011098.
[105] L. Shen, Z. Chen, Critical review of the impact of tortuosity on diffusion, Chem. Eng. Sci. 62 (2007) 3748–3755. https://doi.org/10.1016/j.ces.2007.03.041.
[106] V. Springel, E pur si muove: Galilean-invariant cosmological hydrodynamical simulations on a moving mesh, Mon. Not. R. Astron. Soc. 401 (2010) 791–851. https://doi.org/10.1111/j.1365-2966.2009.15715.x.
[107] C.F. Guerra, J.-W. Handgraaf, E.J. Baerends, F.M. Bickelhaupt, Voronoi deformation density (VDD) charges: Assessment of the Mulliken, Bader, Hirshfeld, Weinhold, and VDD methods for charge analysis, J. Comput. Chem. 25 (2004) 189–210. https://doi.org/10.1002/jcc.10351.
[108] A. Poupon, Voronoi and Voronoi-related tessellations in studies of protein structure and interaction, Curr. Opin. Struct. Biol. 14 (2004) 233–241. https://doi.org/10.1016/j.sbi.2004.03.010.

[109] S.I. Somo, B. Akar, E.S. Bayrak, J.C. Larson, A.A. Appel, H. Mehdizadeh, A. Cinar, E.M. Brey, Pore Interconnectivity Influences Growth Factor-Mediated Vascularization in Sphere-Templated Hydrogels, Tissue Eng. Part C Methods. 21 (2015) 773–785. https://doi.org/10.1089/ten.tec.2014.0454.
[110] N. Zhao, Y. Li, X. Zhao, X. Zhi, G. Liang, Effect of particle size and purity on the low temperature electrochemical performance of LiFePO4/C cathode material, J. Alloys Compd. 683 (2016) 123–132. https://doi.org/10.1016/j.jallcom.2016.04.070.
[111] F.P.W. Melchels, A.M.C. Barradas, C.A. van Blitterswijk, J. de Boer, J. Feijen, D.W. Grijpma, Effects of the architecture of tissue engineering scaffolds on cell seeding and culturing, Acta Biomater. 6 (2010) 4208–4217. https://doi.org/10.1016/j.actbio.2010.06.012.
[112] R. Mendoza, I. Savin, K. Thornton, P.W. Voorhees, Topological complexity and the dynamics of coarsening, Nat. Mater. 3 (2004) 385. https://doi.org/10.1038/nmat1138.
[113] W. Meeks III, J. Perez, The classical theory of minimal surfaces, Bull. Am. Math. Soc. 48 (2011) 325–407. https://doi.org/10.1090/S0273-0979-2011-01334-9.
[114] R. Osserman, A Survey of Minimal Surfaces, Dover Phoenix ed., Dover Publications, New York, 2002.
[115] M. Werner, S.B.G. Blanquer, S.P. Haimi, G. Korus, J.W.C. Dunlop, G.N. Duda, Dirk.W. Grijpma, A. Petersen, Surface curvature differentially regulates stem cell migration and differentiation via altered attachment morphology and nuclear deformation, Adv. Sci. 4 (2017). https://doi.org/10.1002/advs.201600347.
[116] N.D. Bade, T. Xu, R.D. Kamien, R.K. Assoian, K.J. Stebe, Gaussian curvature directs stress fiber orientation and cell migration, Biophys. J. 114 (2018) 1467–1476. https://doi.org/10.1016/j.bpj.2018.01.039.
[117] S. Rajagopalan, R.A. Robb, Schwarz meets Schwann: Design and fabrication of biomorphic and durataxic tissue engineering scaffolds, Med. Image Anal. 10 (2006) 693–712. https://doi.org/10.1016/j.media.2006.06.001.
[118] C.E. Inglis, Stresses in a plate due to the presence of cracks and sharp corners, Trans Inst Nav. Arch. 55 (1913) 219–241.
[119] Z. Qin, G.S. Jung, M.J. Kang, M.J. Buehler, The mechanics and design of a lightweight three-dimensional graphene assembly, Sci. Adv. 3 (2017) e1601536. https://doi.org/10.1126/sciadv.1601536.
[120] N.P. Mitchell, V. Koning, V. Vitelli, W.T.M. Irvine, Fracture in sheets draped on curved surfaces, Nat. Mater. 16 (2016) 89–93. https://doi.org/10.1038/nmat4733.
[121] Christian, M. Mitchell, D.-P. Kim, P.J.A. Kenis, Ceramic microreactors for on-site hydrogen production, J. Catal. 241 (2006) 235–242. https://doi.org/10.1016/j.jcat.2006.04.033.
[122] H. Zhang, T. Shi, D.J. Wetzel, R.G. Nuzzo, P.V. Braun, 3D Scaffolded Nickel-Tin Li-Ion Anodes with Enhanced Cyclability, Adv. Mater. 28 (2016) 742–747. https://doi.org/10.1002/adma.201504780.
[123] S.-W. Choi, Y. Zhang, M.R. MacEwan, Y. Xia, Neovascularization in biodegradable inverse opal scaffolds with uniform and precisely controlled pore sizes, Adv. Healthc. Mater. 2 (2013) 145–154. https://doi.org/10.1002/adhm.201200106.
[124] A. Nalawade, R. V. Ghorpade, S. Shadbar, M. Shadbar Qureshi, N. N. Chavan, A. A. Khan, S. Ponrathnam, Inverse high internal phase emulsion polymerization (i-HIPE) of GMMA, HEMA and GDMA for the preparation of superporous hydrogels as a tissue

engineering scaffold, J. Mater. Chem. B. 4 (2016) 450–460. https://doi.org/10.1039/C5TB01873K.
[125] Ashby M.F, The properties of foams and lattices, Philos. Trans. R. Soc. Math. Phys. Eng. Sci. 364 (2006) 15–30. https://doi.org/10.1098/rsta.2005.1678.
[126] X.-Y. Sun, G.-K. Xu, X. Li, X.-Q. Feng, H. Gao, Mechanical properties and scaling laws of nanoporous gold, J. Appl. Phys. 113 (2013) 023505. https://doi.org/10.1063/1.4774246.
[127] W. Lee, C.-H. Ho, J.W. Van Zee, M. Murthy, The effects of compression and gas diffusion layers on the performance of a PEM fuel cell, J. Power Sources. 84 (1999) 45–51. https://doi.org/10.1016/S0378-7753(99)00298-0.
[128] U. Tallarek, F.J. Vergeldt, H.V. As, Stagnant mobile phase mass transfer in chromatographic media: Intraparticle diffusion and exchange kinetics, J. Phys. Chem. B. 103 (1999) 7654–7664. https://doi.org/10.1021/jp990828b.
[129] T.I. Croll, S. Gentz, K. Mueller, M. Davidson, A.J. O'Connor, G.W. Stevens, J.J. Cooper-White, Modelling oxygen diffusion and cell growth in a porous, vascularising scaffold for soft tissue engineering applications, Chem. Eng. Sci. 60 (2005) 4924–4934. https://doi.org/10.1016/j.ces.2005.03.051.
[130] M. Xu, D.G. Ivey, Z. Xie, W. Qu, Rechargeable Zn-air batteries: Progress in electrolyte development and cell configuration advancement, J. Power Sources. 283 (2015) 358–371. https://doi.org/10.1016/j.jpowsour.2015.02.114.
[131] A.M. Zamarayeva, A.M. Gaikwad, I. Deckman, M. Wang, B. Khau, D.A. Steingart, A.C. Arias, Fabrication of a High-Performance Flexible Silver-Zinc Wire Battery, Adv. Electron. Mater. 2 (2016) 1500296. https://doi.org/10.1002/aelm.201500296.
[132] J. Fu, Z.P. Cano, M.G. Park, A. Yu, M. Fowler, Z. Chen, Electrically Rechargeable Zinc-Air Batteries: Progress, Challenges, and Perspectives, Adv. Mater. 29 (2017) 1604685. https://doi.org/10.1002/adma.201604685.
[133] A.P. Karpinski, B. Makovetski, S.J. Russell, J.R. Serenyi, D.C. Williams, Silver–zinc: status of technology and applications, J. Power Sources. 80 (1999) 53–60.
[134] H. Kim, G. Jeong, Y.-U. Kim, J.-H. Kim, C.-M. Park, H.-J. Sohn, Metallic anodes for next generation secondary batteries, Chem. Soc. Rev. 42 (2013) 9011–9034. https://doi.org/10.1039/C3CS60177C.
[135] G. Liang, F. Mo, H. Li, Z. Tang, Z. Liu, D. Wang, Q. Yang, L. Ma, C. Zhi, A Universal Principle to Design Reversible Aqueous Batteries Based on Deposition–Dissolution Mechanism, Adv. Energy Mater. 0 (n.d.) 1901838. https://doi.org/10.1002/aenm.201901838.
[136] X. Chen, Z. Zhou, H.E. Karahan, Q. Shao, L. Wei, Y. Chen, Recent Advances in Materials and Design of Electrochemically Rechargeable Zinc–Air Batteries, Small. 14 (2018) 1801929. https://doi.org/10.1002/smll.201801929.
[137] Y. Wu, Y. Zhang, Y. Ma, J.D. Howe, H. Yang, P. Chen, S. Aluri, N. Liu, Ion-Sieving Carbon Nanoshells for Deeply Rechargeable Zn-Based Aqueous Batteries, Adv. Energy Mater. 8 (2018) 1802470. https://doi.org/10.1002/aenm.201802470.
[138] Y. Zhang, Y. Wu, H. Ding, Y. Yan, Z. Zhou, Y. Ding, N. Liu, Sealing ZnO nanorods for deeply rechargeable high-energy aqueous battery anodes, Nano Energy. 53 (2018) 666–674. https://doi.org/10.1016/j.nanoen.2018.09.021.
[139] K. Wang, P. Pei, Z. Ma, H. Chen, H. Xu, D. Chen, X. Wang, Dendrite growth in the recharging process of zinc–air batteries, J. Mater. Chem. A. 3 (2015) 22648–22655. https://doi.org/10.1039/C5TA06366C.

[140] D.E. Turney, J.W. Gallaway, G.G. Yadav, R. Ramirez, M. Nyce, S. Banerjee, Y.K. Chen-Wiegart, J. Wang, M.J. D'Ambrose, S. Kolhekar, J. Huang, X. Wei, Rechargeable Zinc Alkaline Anodes for Long-Cycle Energy Storage, Chem. Mater. 29 (2017) 4819–4832. https://doi.org/10.1021/acs.chemmater.7b00754.
[141] A. Nakata, H. Arai, T. Yamane, T. Hirai, Z. Ogumi, Preserving Zinc Electrode Morphology in Aqueous Alkaline Electrolytes Mixed with Highly Concentrated Organic Solvent, J. Electrochem. Soc. 163 (2016) A50–A56. https://doi.org/10.1149/2.0091602jes.
[142] T.C. Adler, F.R. McLarnon, E.J. Cairns, Low-Zinc-Solubility Electrolytes for Use in Zinc/Nickel Oxide Cells, J. Electrochem. Soc. 140 (1993) 289–294. https://doi.org/10.1149/1.2221039.
[143] J.F. Parker, I.R. Pala, C.N. Chervin, J.W. Long, D.R. Rolison, Minimizing shape change at Zn sponge anodes in rechargeable Ni–Zn cells: impact of electrolyte formulation, J. Electrochem. Soc. 163 (2016) A351–A355.
[144] J.-S. Chen, F.R. Mclarnon, E.J. Cairns, Investigation of low-zinc-solubility electrodes and electrolytes in zinc/silver oxide cells, J. Power Sources. 39 (1992) 333–348.
[145] Z. Zhao, J. Zhao, Z. Hu, J. Li, J. Li, Y. Zhang, C. Wang, G. Cui, Long-life and deeply rechargeable aqueous Zn anodes enabled by a multifunctional brightener-inspired interphase, Energy Environ. Sci. (2019). https://doi.org/10.1039/C9EE00596J.
[146] D. Zeng, Z. Yang, S. Wang, X. Ni, D. Ai, Q. Zhang, Preparation and electrochemical performance of In-doped ZnO as anode material for Ni–Zn secondary cells, Electrochimica Acta. 56 (2011) 4075–4080. https://doi.org/10.1016/j.electacta.2011.01.119.
[147] Y.N. Jo, S.H. Kang, K. Prasanna, S.W. Eom, C.W. Lee, Shield effect of polyaniline between zinc active material and aqueous electrolyte in zinc-air batteries, Appl. Surf. Sci. 422 (2017) 406–412. https://doi.org/10.1016/j.apsusc.2017.06.033.
[148] S.J. Banik, R. Akolkar, Suppressing Dendritic Growth during Alkaline Zinc Electrodeposition using Polyethylenimine Additive, Electrochimica Acta. 179 (2015) 475–481. https://doi.org/10.1016/j.electacta.2014.12.100.
[149] A. Mitha, A.Z. Yazdi, M. Ahmed, P. Chen, Surface Adsorption of Polyethylene Glycol to Suppress Dendrite Formation on Zinc Anodes in Rechargeable Aqueous Batteries, ChemElectroChem. 5 (2018) 2409–2418. https://doi.org/10.1002/celc.201800572.
[150] J.F. Parker, C.N. Chervin, I.R. Pala, M. Machler, M.F. Burz, J.W. Long, D.R. Rolison, Rechargeable nickel–3D zinc batteries: An energy-dense, safer alternative to lithium-ion, Science. 356 (2017) 415–418. https://doi.org/10.1126/science.aak9991.
[151] J.S. Ko, A.B. Geltmacher, B.J. Hopkins, D.R. Rolison, J.W. Long, J.F. Parker, Robust 3D Zn Sponges Enable High-Power, Energy-Dense Alkaline Batteries, ACS Appl. Energy Mater. 2 (2019) 212–216. https://doi.org/10.1021/acsaem.8b01946.
[152] M.N. Lee, A. Mohraz, Hierarchically Porous Silver Monoliths from Colloidal Bicontinuous Interfacially Jammed Emulsion Gels, J. Am. Chem. Soc. 133 (2011) 6945–6947. https://doi.org/10.1021/ja201650z.
[153] K.M. McDevitt, T.J. Thorson, E.L. Botvinick, D.R. Mumm, A. Mohraz, Microstructural characteristics of bijel-templated porous materials, Materialia. 7 (2019) 100393. https://doi.org/10.1016/j.mtla.2019.100393.
[154] S. Müller, F. Holzer, O. Haas, Optimized zinc electrode for the rechargeable zinc–air battery, J. Appl. Electrochem. 28 (1998) 895–898.

[155] W. Stöber, A. Fink, E. Bohn, Controlled growth of monodisperse silica spheres in the micron size range, J. Colloid Interface Sci. 26 (1968) 62–69. https://doi.org/10.1016/0021-9797(68)90272-5.
[156] R.J. Park, F.C. Meldrum, Synthesis of Single Crystals of Calcite with Complex Morphologies, Adv. Mater. 14 (2002) 1167. https://doi.org/10.1002/1521-4095(20020816)14:16<1167::AID-ADMA1167>3.0.CO;2-X.
[157] M. Yano, S. Fujitani, K. Nishio, Y. Akai, M. Kurimura, Effect of additives in zinc alloy powder on suppressing hydrogen evolution, J. Power Sources. 74 (1998) 129–134. https://doi.org/10.1016/S0378-7753(98)00044-5.
[158] R.F. Smart, E.C. Ellwood, Sintering of Tin Powder, Nature. 181 (1958) 833–834. https://doi.org/10.1038/181833a0.
[159] C.-Y. Jung, T.-H. Kim, W.-J. Kim, S.-C. Yi, Computational analysis of the zinc utilization in the primary zinc-air batteries, Energy. 102 (2016) 694–704. https://doi.org/10.1016/j.energy.2016.02.084.
[160] K. Wang, Y. Xiao, P. Pei, X. Liu, Y. Wang, A Phase-Field Model of Dendrite Growth of Electrodeposited Zinc, J. Electrochem. Soc. 166 (2019) D389–D394. https://doi.org/10.1149/2.0541910jes.
[161] C. Lupo, D. Schlettwein, Modeling of Dendrite Formation as a Consequence of Diffusion-Limited Electrodeposition, J. Electrochem. Soc. 166 (2019) D3182–D3189. https://doi.org/10.1149/2.0231901jes.
[162] A. Nakata, H. Murayama, K. Fukuda, T. Yamane, H. Arai, T. Hirai, Y. Uchimoto, J. Yamaki, Z. Ogumi, Transformation of Leaf-like Zinc Dendrite in Oxidation and Reduction Cycle, Electrochimica Acta. 166 (2015) 82–87. https://doi.org/10.1016/j.electacta.2015.03.076.
[163] W. Lu, C. Xie, H. Zhang, X. Li, Inhibition of Zinc Dendrite Growth in Zinc-Based Batteries, ChemSusChem. 11 (2018) 3996–4006. https://doi.org/10.1002/cssc.201801657.
[164] S. Arouete, K.F. Blurton, H.G. Oswin, Controlled Current Deposition of Zinc from Alkaline Solution, J. Electrochem. Soc. 116 (1969) 166–169. https://doi.org/10.1149/1.2411787.
[165] J.A. Dean, N.A. Lange, eds., Lange's handbook of chemistry, 15. ed, McGraw-Hill, New York, NY, 1999.
[166] B. Beverskog, I. Puigdomenech, Revised pourbaix diagrams for zinc at 25–300 °C, Corros. Sci. 39 (1997) 107–114. https://doi.org/10.1016/S0010-938X(97)89246-3.
[167] T.-H. Wu, Y. Zhang, Z.D. Althouse, N. Liu, Nanoscale design of zinc anodes for high-energy aqueous rechargeable batteries, Mater. Today Nano. 6 (2019) 100032. https://doi.org/10.1016/j.mtnano.2019.100032.
[168] J.-J. Yun, N.-I. Kim, C.K. Hong, K.H. Park, Inhibition of Hydrogen Formation with Calcium Hydroxide on Zinc Electrode of Film-type Manganese Battery, Trans. Electr. Electron. Mater. 16 (2015) 135–138. https://doi.org/10.4313/TEEM.2015.16.3.135.
[169] M. Schmid, M. Willert-Porada, Electrochemical behavior of zinc particles with silica based coatings as anode material for zinc air batteries with improved discharge capacity, J. Power Sources. 351 (2017) 115–122. https://doi.org/10.1016/j.jpowsour.2017.03.096.
[170] T. Mitsuhashi, Y. Ito, Y. Takeuchi, S. Harada, T. Ujihara, Non-uniform electrodeposition of zinc on the (0001) plane, Thin Solid Films. 590 (2015) 207–213. https://doi.org/10.1016/j.tsf.2015.07.068.

[171] T. Otani, M. Nagata, Y. Fukunaka, T. Homma, Morphological evolution of mossy structures during the electrodeposition of zinc from an alkaline zincate solution, Electrochimica Acta. 206 (2016) 366–373. https://doi.org/10.1016/j.electacta.2016.04.124.
[172] B. Dunn, C. Kim, S. Tolbert, Three-dimensional microbatteries for MEMS/NEMS technology, in: 2010 IEEE 23rd Int. Conf. Micro Electro Mech. Syst. MEMS, 2010: pp. 164–167. https://doi.org/10.1109/MEMSYS.2010.5442541.
[173] N. Chawake, L.D. Pinto, A.K. Srivastav, K. Akkiraju, B.S. Murty, R.S. Kottada, On Joule heating during spark plasma sintering of metal powders, Scr. Mater. 93 (2014) 52–55. https://doi.org/10.1016/j.scriptamat.2014.09.003.
[174] O. Guillon, J. Gonzalez-Julian, B. Dargatz, T. Kessel, G. Schierning, J. Räthel, M. Herrmann, Field-Assisted Sintering Technology/Spark Plasma Sintering: Mechanisms, Materials, and Technology Developments: FAST/SPS: Mechanisms, Materials, and Technology Developments, Adv. Eng. Mater. 16 (2014) 830–849. https://doi.org/10.1002/adem.201300409.
[175] X. Song, X. Liu, J. Zhang, Neck Formation and Self-Adjusting Mechanism of Neck Growth of Conducting Powders in Spark Plasma Sintering, J. Am. Ceram. Soc. 89 (2006) 494–500. https://doi.org/10.1111/j.1551-2916.2005.00777.x.
[176] X. Cheng, Z. Shi, N. Glass, L. Zhang, J. Zhang, D. Song, Z.-S. Liu, H. Wang, J. Shen, A review of PEM hydrogen fuel cell contamination: Impacts, mechanisms, and mitigation, J. Power Sources. 165 (2007) 739–756. https://doi.org/10.1016/j.jpowsour.2006.12.012.
[177] F. Suleman, I. Dincer, M. Agelin-Chaab, Environmental impact assessment and comparison of some hydrogen production options, Int. J. Hydrog. Energy. 40 (2015) 6976–6987. https://doi.org/10.1016/j.ijhydene.2015.03.123.
[178] A. Godula-Jopek, Hydrogen Production: by Electrolysis, John Wiley & Sons, 2015.
[179] K. Zeng, D. Zhang, Recent progress in alkaline water electrolysis for hydrogen production and applications, Prog. Energy Combust. Sci. 36 (2010) 307–326. https://doi.org/10.1016/j.pecs.2009.11.002.
[180] B.D. James, D.A. DeSantis, G. Saur, National Renewable Energy Lab. (NREL), Golden, CO (United States), Argonne National Lab. (ANL), Argonne, IL (United States), Final Report: Hydrogen Production Pathways Cost Analysis (2013 – 2016), 2016. https://doi.org/10.2172/1346418.
[181] R.L. Doyle, M.E.G. Lyons, The Oxygen Evolution Reaction: Mechanistic Concepts and Catalyst Design, in: S. Giménez, J. Bisquert (Eds.), Photoelectrochem. Sol. Fuel Prod., Springer International Publishing, Cham, 2016: pp. 41–104. https://doi.org/10.1007/978-3-319-29641-8_2.
[182] H. Yu, N. Danilovic, Y. Wang, W. Willis, A. Poozhikunnath, L. Bonville, C. Capuano, K. Ayers, R. Maric, Nano-size IrOx catalyst of high activity and stability in PEM water electrolyzer with ultra-low iridium loading, Appl. Catal. B Environ. 239 (2018) 133–146. https://doi.org/10.1016/j.apcatb.2018.07.064.
[183] H. Vogt, The actual current density of gas-evolving electrodes—Notes on the bubble coverage, Electrochimica Acta. 78 (2012) 183–187. https://doi.org/10.1016/j.electacta.2012.05.124.
[184] H. Vogt, R.J. Balzer, The bubble coverage of gas-evolving electrodes in stagnant electrolytes, Electrochimica Acta. 50 (2005) 2073–2079. https://doi.org/10.1016/j.electacta.2004.09.025.

[185] J. Venczel, Ueber den Stofftransport an gasentwickelnden Elektroden, ETH Zurich, 1961. https://doi.org/10.3929/ethz-a-000091264.
[186] A.K. Taylor, I. Andreu, B.D. Gates, Regular Dimpled Nickel Surfaces for Improved Efficiency of the Oxygen Evolution Reaction, ACS Appl. Energy Mater. 1 (2018) 1771–1782. https://doi.org/10.1021/acsaem.8b00338.
[187] A.R. Zeradjanin, A.A. Topalov, Q. Van Overmeere, S. Cherevko, X. Chen, E. Ventosa, W. Schuhmann, K.J.J. Mayrhofer, Rational design of the electrode morphology for oxygen evolution – enhancing the performance for catalytic water oxidation, RSC Adv. 4 (2014) 9579. https://doi.org/10.1039/c3ra45998e.
[188] Ph. Mandin, A.A. Aissa, H. Roustan, J. Hamburger, G. Picard, Two-phase electrolysis process: From the bubble to the electrochemical cell properties, Chem. Eng. Process. Process Intensif. 47 (2008) 1926–1932. https://doi.org/10.1016/j.cep.2007.10.018.
[189] C.W. Tobias, Effect of Gas Evolution on Current Distribution and Ohmic Resistance in Electrolyzers, 106 (1959) 6.
[190] C.-T. Lu, Y.-W. Chiu, M.-J. Li, K.-L. Hsueh, J.-S. Hung, Reduction of the Electrode Overpotential of the Oxygen Evolution Reaction by Electrode Surface Modification, Int. J. Electrochem. (2017). https://doi.org/10.1155/2017/7494571.
[191] D. Kosior, J. Zawala, Initial degree of detaching bubble adsorption coverage and the kinetics of dynamic adsorption layer formation, Phys. Chem. Chem. Phys. 20 (2018) 2403–2412. https://doi.org/10.1039/C7CP06099H.
[192] R.J. Balzer, H. Vogt, Effect of Electrolyte Flow on the Bubble Coverage of Vertical Gas-Evolving Electrodes, J. Electrochem. Soc. 150 (2003) E11–E16. https://doi.org/10.1149/1.1524185.
[193] A. Prakash Periasamy, P. Sriram, Y.-W. Chen, C.-W. Wu, T.-J. Yen, H.-T. Chang, Porous aluminum electrodes with 3D channels and zig-zag edges for efficient hydrogen evolution, Chem. Commun. 55 (2019) 5447–5450. https://doi.org/10.1039/C9CC01667H.
[194] I. Herraiz-Cardona, E. Ortega, L. Vázquez-Gómez, V. Pérez-Herranz, Double-template fabrication of three-dimensional porous nickel electrodes for hydrogen evolution reaction, Int. J. Hydrog. Energy. 37 (2012) 2147–2156. https://doi.org/10.1016/j.ijhydene.2011.09.155.
[195] M.N. Lee, A. Mohraz, Bicontinuous Macroporous Materials from Bijel Templates, Adv. Mater. 22 (2010) 4836–4841. https://doi.org/10.1002/adma.201001696.
[196] M. Reeves, K. Stratford, J.H.J. Thijssen, Quantitative morphological characterization of bicontinuous Pickering emulsions via interfacial curvatures, Soft Matter. 12 (2016) 4082–4092. https://doi.org/10.1039/C5SM03102H.
[197] V.W.L. Chan, K. Thornton, Channel size distribution of complex three-dimensional microstructures calculated from the topological characterization of isodistance structures, Acta Mater. 60 (2012) 2509–2517. https://doi.org/10.1016/j.actamat.2011.12.042.
[198] E.M. Herzig, K.A. White, A.B. Schofield, W.C.K. Poon, P.S. Clegg, Bicontinuous emulsions stabilized solely by colloidal particles, Nat. Mater. 6 (2007) 966–971. https://doi.org/10.1038/nmat2055.
[199] M.E. Cates, P.S. Clegg, Bijels: a new class of soft materials, Soft Matter. 4 (2008) 2132. https://doi.org/10.1039/b807312k.
[200] J.A. Witt, D.R. Mumm, A. Mohraz, Microstructural tunability of co-continuous bijel-derived electrodes to provide high energy and power densities, J Mater Chem A. 4 (2016) 1000–1007. https://doi.org/10.1039/C5TA06260H.

[201] K. McDevitt, D.R. Mumm, A. Mohraz, Improving Cyclability of ZnO Electrodes Through Microstructural Design, ACS Appl. Energy Mater. (2019). https://doi.org/10.1021/acsaem.9b01584.
[202] M.N. Lee, J.H.J. Thijssen, J.A. Witt, P.S. Clegg, A. Mohraz, Making a Robust Interfacial Scaffold: Bijel Rheology and its Link to Processability, Adv. Funct. Mater. 23 (2013) 417–423. https://doi.org/10.1002/adfm.201201090.
[203] S.H. Ahn, I. Choi, H.-Y. Park, S.J. Hwang, S.J. Yoo, E. Cho, H.-J. Kim, D. Henkensmeier, S.W. Nam, S.-K. Kim, J.H. Jang, Effect of morphology of electrodeposited Ni catalysts on the behavior of bubbles generated during the oxygen evolution reaction in alkaline water electrolysis, Chem. Commun. 49 (2013) 9323. https://doi.org/10.1039/c3cc44891f.
[204] P. Zhu, Y. Zhao, Cyclic voltammetry measurements of electroactive surface area of porous nickel: Peak current and peak charge methods and diffusion layer effect, Mater. Chem. Phys. 233 (2019) 60–67. https://doi.org/10.1016/j.matchemphys.2019.05.034.
[205] J.H. Montoya, L.C. Seitz, P. Chakthranont, A. Vojvodic, T.F. Jaramillo, J.K. Nørskov, Materials for solar fuels and chemicals, Nat. Mater. 16 (2017) 70–81. https://doi.org/10.1038/nmat4778.
[206] C. Wei, Z.J. Xu, The Comprehensive Understanding of 10mA/cm2 as an Evaluation Parameter for Electrochemical Water Splitting, Small Methods. 2 (2018) 1800168. https://doi.org/10.1002/smtd.201800168.
[207] P. Lehmann, M. Berchtold, B. Ahrenholz, J. Tölke, A. Kaestner, M. Krafczyk, H. Flühler, H.R. Künsch, Impact of geometrical properties on permeability and fluid phase distribution in porous media, Adv. Water Resour. 31 (2008) 1188–1204. https://doi.org/10.1016/j.advwatres.2008.01.019.
[208] M.R. Nokken, R.D. Hooton, Using pore parameters to estimate permeability or conductivity of concrete, Mater. Struct. 41 (2008) 1. https://doi.org/10.1617/s11527-006-9212-y.
[209] N. Neithalath, M.S. Sumanasooriya, O. Deo, Characterizing pore volume, sizes, and connectivity in pervious concretes for permeability prediction, Mater. Charact. 61 (2010) 802–813. https://doi.org/10.1016/j.matchar.2010.05.004.
[210] C.F. Berg, Permeability description by characteristic length, tortuosity, constriction and porosity, Transp. Porous Media. 103 (2014) 381–400. https://doi.org/10.1007/s11242-014-0307-6.
[211] Y. Choquette, Study of the Kinetics of Hydrogen Evolution Reaction on Raney Nickel Composite-Coated Electrode by AC Impedance Technique, J. Electrochem. Soc. 137 (1990) 1723. https://doi.org/10.1149/1.2086788.
[212] M.R.G. de Chialvo, A.C. Chialvo, Hydrogen evolution reaction: Analysis of the Volmer-Heyrovsky-Tafel mechanism with a generalized adsorption model, J. Electroanal. Chem. 372 (1994) 209–223. https://doi.org/10.1016/0022-0728(93)03043-O.
[213] E. Putri, G. Brooks, G.A. Snook, I. Eick, L.P. Lossius, Diffusion and Flow of CO2 in Carbon Anode for Aluminium Smelting, Metall. Mater. Trans. B. 50 (2019) 846–856. https://doi.org/10.1007/s11663-018-1497-z.
[214] H. Kvande, Production of primary aluminium, in: Fundam. Alum. Metall., Elsevier, 2011: pp. 49–69. https://doi.org/10.1533/9780857090256.1.49.
[215] M. Dupuis, J. Thonstad, T.A. Utigard, H. Vogt, On the Anode Effect in Aluminum Electrolysis, in: G. Bearne, G. Tarcy (Eds.), Essent. Read. Light Met., John Wiley & Sons,

Inc., Hoboken, NJ, USA, 2013: pp. 131–138. https://doi.org/10.1002/9781118647851.ch18.
[216] X.-Y. Fan, J. Han, Y.-L. Ding, Y.-P. Deng, D. Luo, X. Zeng, Z. Jiang, L. Gou, D.-L. Li, Z. Chen, Sodium Ion Batteries: 3D Nanowire Arrayed Cu Current Collector toward Homogeneous Alloying Anode Deposition for Enhanced Sodium Storage (Adv. Energy Mater. 28/2019), Adv. Energy Mater. 9 (2019) 1970111. https://doi.org/10.1002/aenm.201970111.
[217] J.-J. Lv, M. Jouny, W. Luc, W. Zhu, J.-J. Zhu, F. Jiao, A Highly Porous Copper Electrocatalyst for Carbon Dioxide Reduction, Adv. Mater. 30 (2018) 1803111. https://doi.org/10.1002/adma.201803111.
[218] D. Böhm, M. Beetz, M. Schuster, K. Peters, A.G. Hufnagel, M. Döblinger, B. Böller, T. Bein, D. Fattakhova-Rohlfing, Efficient OER Catalyst with Low Ir Volume Density Obtained by Homogeneous Deposition of Iridium Oxide Nanoparticles on Macroporous Antimony-Doped Tin Oxide Support, Adv. Funct. Mater. 0 (2019) 1906670. https://doi.org/10.1002/adfm.201906670.